Multi-Mode Antennas for Hemispherical Field-of-View Coverage

by

David Schalk van der Merwe Prinsloo

Dissertation approved for the degree of Doctor of Philosophy in Electronic Engineering in the Faculty of Engineering at Stellenbosch University

Promoters:

Prof. Petrie Meyer Prof. Marianna V. Ivashina Dr. Rob Maaskant

March 2015

Declaration

By submitting this thesis electronically, I declare that the entirety of the work contained therein is my own, original work, that I am the sole author thereof (save to the extent explicitly otherwise stated), that reproduction and publication thereof by Stellenbosch University will not infringe any third party rights and that I have not previously in its entirety or in part submitted it for obtaining any qualification.

March 2015

Abstract

Keywords – Receiving antennas, Radio astronomy, Multi-conductor transmission lines, Beamforming, Signal-to-noise ratio, Network theory

This dissertation proposes a multi-mode antenna element excited through a multiconductor feed. It is shown that each of the orthogonal transverse electromagnetic modes supported by the antenna feed results in a unique radiated far-field pattern that collectively allow for near-hemispherical field-of-view coverage.

Three multi-mode antenna designs are presented: a dual-mode antenna, integrating a single linearly polarised dipole antenna with a co-located monopole, as well as two quad-mode antenna designs integrating two dual-polarised dipole elements with a co-located monopole element. The dual-mode antenna is excited through a balanced transmission line feed supporting both differential- and common-mode signals that, respectively, result in typical dipole-over-ground and monopole radiated far-field patterns. The quad-mode antennas are each fed through a quadraxial transmission line allowing for excitation through four orthogonal transverse electromagnetic port modes.

To characterise the multi-mode response of the multi-mode antennas, generalised transformations are derived by which the multi-mode S-parameters and radiated far-fields can be calculated from the S-parameters and far-fields corresponding to single-ended excitations. These transformations are implemented to validate the response of a dual-mode and quad-mode antenna design through measurements.

An equivalent network representation for active multi-mode antennas is presented, including generalised transformations relating the multi-mode signal and noise response of the low-noise amplifiers to the two-port S-parameters and noise parameters of the low-noise amplifiers. Through the use of classical beamforming algorithms, the performance of an active dual-mode and quad-mode antenna is presented. In the case of the active dual-mode antenna, it is shown that through the added use of common-mode signals, a variation in sensitivity of less than 50% is achieved in the E-plane. Similarly, the additional excitation modes supported by the active quad-mode antenna is shown to result in a significant improvement in the polarimetric capabilities over the field-of-view coverage.

Opsomming

Sleutelwoorde – Ontvangsantennas, Radio-sterrekunde, Multi-geleier transmissielyne, Bundelvorming, Sein-tot-ruis verhouding, Netwerkteorie

Hierdie proefskrif stel 'n multimodale antenna element voor wat deur 'n multi-geleier transmissielyn gevoer word. Dit word gewys dat elk van die ortogonale transversale elektromagnetiese opwekkingsmodusse wat deur die antenna voer ondersteun word, 'n unieke vêrveld stralingspatroon skep, wat gesamentlik lei tot 'n hemisferiese gesigsveld.

Drie multimodale antenna ontwerpe word voorgestel: 'n dubbelmodale antenna, waarin 'n enkel lineêrgepolariseerde dipool antenna en monopool mede-geleë word, asook twee viermodale antenna ontwerpe waarin twee dubbelgepolariseerde dipool elemente geïntegreer word met mede-geleë monopool antenna elemente. Die dubbelmodale antenna word gevoer deur 'n gebalanseerde transmissielyn wat beide differensiële- en gemene-modus seine ondersteun, waar elk onderskeidelik dipool-oor-aardvlak en monopool stralingspatrone voortbring. Die viermodale antennas word elk gevoer deur vier-as transmissielyne wat vier ortogonale transversale elektromagnetiese opwekkingsmodusse ondersteun.

Om die multimodale gedrag van die drie multimodale antennas te karakteriseer, word veralgemeende transformasies afgelei waardeur die multimodale strooiingsparameters asook die vêrveld stralingspatrone vanaf enkelpoort strooiingsparameters en vêrvelde bereken word. Hierdie transformasies word toegepas om die gedrag van 'n dubbel- en viermodale antenna ontwerp te karakteriseer deur metings.

Ekwivalente netwerkvoorstellings vir aktiewe multimodale antennas word voorgestel, insluitend veralgemeende transformasies om die multimodale sein asook ruis gedrag van die lae-ruis versterkers betreklik te maak tot die tweepoort strooiingsparameters en ruisparameters van die lae-ruis versterkers. Deur gebruik te maak van klasieke bundelvormingsalgoritmes, word die gedrag van aktiewe dubbelmodale en viermodale antennas voorgestel. Vir die aktiewe dubbelmodale antenna word daar aangedui dat die gesamentlike gebruik van differensiële- en gemene-modus seine, 'n variasie in sensitiwiteit onder 50% tot gevolg het in die E-vlak. Soortgelyk word daar aangedui dat die addisionele opwekkingsmodusse wat deur die aktiewe viermodale antenna ondersteun word, tot 'n beduidende verbetering in die polarisasievermoë oor die gesigsveld lei.

Acknowledgements

I would like to acknowledge the following people and institutes for their invaluable assistance and support throughout this work. First and foremost my supervisors prof. Petrie Meyer, prof. Marianna Ivashina, and dr. Rob Maaskant for their constant guidance and advice throughout this work, and for always making time available in their busy schedules. In particular, prof. Meyer for his unfailing patience and sound words of encouragement during the times when results seemed out of reach. Prof. Ivashina and dr. Maaskant for hosting me at Chalmers University of Technology for several months. The discussions with prof. Ivashina and dr. Maaskant during my time at Chalmers made for some of the most productive periods during the course of this work. At Stellenbosch University, I would like to acknowledge prof. P.W. van der Walt for the insightful discussions during the earlier phases of the work, prof. David Davidson for enabling me to continue with SKA related research, dr. Dirk de Villiers for the discussions on antenna measurements, Wessel Croukamp and Wynand van Eeden for lending their expertise during the manufacturing of the antenna designs, and finally Anneke Bester for patiently assisting me with all the antenna measurements. For the time spent with the Antenna Group at Chalmers University of Technology in Gothenburg, Sweden, I would like to extend my sincerest gratitude towards prof. Per-Simon Kildal for always making me feel welcome at the department, to dr. Tobia Carozzi for the discussions on polarimetry, and lastly to all the researchers at the Antenna Group for making me feel at home in Gothenburg.

Closer to home, I would like to thank my family for constantly showing interest in the progress of my work. To my mother for her insightful advice no matter how technical the problem, my father for his constant moral support and keen interest in my work, and finally my brother for his invaluable advice on all non-work related topics. To my fellow postgraduate students at Stellenbosch University, in particular Shamim, Theunis, Dewald, and Satyam who shared the office with me, thank you for a truly memorable time at Stellenbosch. I would also like to thank all my friends who earnestly kept my life in balance and celebrated every accomplishment with me. Finally, the work presented in this dissertation could not have been completed without the financial support of the following institutes: the National Research Foundation (NRF), the Square Kilometre Array project, the South African Research Chairs Initiative of the Department of Science and Technology in South Africa, the Swedish Research Council (VR), VINNOVA, as well as the Marie Curie international research staff exchange scheme fellowship within the European FP7 programme.

Contents

List of Figures

List of Tables

List of Acronyms

AA	Aperture Array
AAVS	Aperture Array Verification System
ASTRON	Netherlands Institute for Radio Astronomy
BF	Beamformer
CM	Common-Mode
CST	Computer Simulation Technology
DM	Differential-Mode
EEP	Embedded Element Pattern
EMBRACE	Electronic Multi-Beam Radio Astronomy Concept
FIDA3	Fundación General Intituto Geográfico Nacional - Differential Active Antenna Array
FoV	Field-of-View
HBA	High Band Antenna
IXR	Intrinsic Cross-polarisation Ratio
LBA	Low Band Antenna
LNA	Low-Noise Amplifier
LOFAR	Low Frequency Array
LWA	Long Wavelength Array
MM	Multi-Mode
MPR	Multi-Port Receiver
MWA	Murchison Widefield Array
OPMN	Optimal-Polarisation Minimum-Noise
ORA	Octagonal Ring Array
SE	Single-Ended
SKA	Square Kilometre Array
SKALA	SKA Log-periodic Antenna
SNR	Signal-to-Noise Ratio
SSFoM	Survey Speed Figure-of-Merit
TEM	Transverse Electromagnetic
VLA	Very Large Array
VSWR	Voltage Standing Wave Ratio
XPD	Cross-Polarisation Discrimination
XPI	Cross-Polarisation Isolation
XPR	Cross-Polarisation Ratio

Chapter 1

Introduction

1.1 Motivation

Following recent advances in digital signal processing hardware, a number of large phased array radio telescopes have come under construction to observe within the Very High Frequency (VHF) and Ultra High Frequency (UHF) bands. At the forefront of this technology are large irregular arrays such as the Low Frequency Array (LOFAR) operating at frequencies ranging from 10 MHz to 240 MHz, the Murchison Wide-field Array (MWA) observing at 80 MHz to 300 MHz, as well as dense connected arrays such as the Electronic Multi-Beam Radio Astronomy Concept (EMBRACE) operating from 500 MHz up to 1.5 GHz. Through the use of electronic beamformers, complex valued beamforming weights can be applied to each of the constituent array antenna elements to steer the collective array beam over the Field-of-View (FoV). Furthermore, given a large number of antenna elements, multiple beams can be formed simultaneously to realise a large aggregated instantaneous FoV. With the technological readiness of digital beamforming arrays displayed through these precursor telescopes, the design of a next generation radio telescope incorporating irregular sparse as well as dense connected arrays with unsurpassed collection surfaces has been set in motion. This next generation radio telescope is referred to as the Square Kilometre Array (SKA) telescope.

To allow for longer observation times it is desirable to track celestial objects as they transit across the celestial plane. Presently the majority of phased array radio telescopes implement purely differential antenna elements able to discern the polarisation state of radio emissions up to scan angles of approximately 45° from zenith. Various antenna elements have been proposed to achieve such a scan range, including inverted-V dipoles (LOFAR), vertically positioned bow-tie antennas (MWA), and tapered slot antennas (EMBRACE), amongst others. A detailed discussion of these systems is presented in Chapter 2, where it is shown that the present state-of-the-art typically achieves ±45° scan range. However, according to the specifications of the SKA telescope, it is desired that the antenna elements that form part of the phased arrays of the telescope should be able to discern the polarisation state of an incident electromagnetic wave

front up to 60° from zenith [1]. It is the aim of this dissertation to present such an antenna element.

1.2 About the Dissertation

This dissertation proposes antenna elements excited through multiconductor transmission lines supporting multiple orthogonal transverse electromagnetic (TEM) modes. Three multi-mode antenna designs are presented including, a dual-mode antenna excited through a twin axial transmission line supporting two orthogonal modes, and two quad-mode antenna designs excited through a quadraxial transmission line supporting four orthogonal modes.

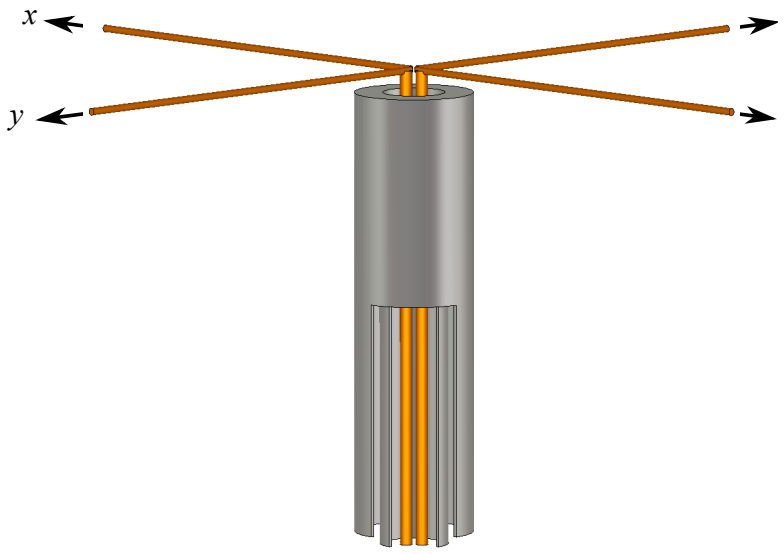

Figure 1.1: Cylindrical quad-mode antenna design integrating two orthogonal dipoles and a monopole sleeve into a single antenna excited through a quadraxial feed.

Figure 1.1 shows a graphic illustration of one of the quad-mode antenna designs. As shown, the quad-mode antenna integrates two orthogonal dipoles and a monopole element into a single antenna excited through a quadraxial feed. The monopole element integrated into the design is realised by folding the ground shield of the feed back over itself resulting in a concentric, cylindrical sleeve. It is shown that this cylindrical sleeve enables the quad-mode antenna to radiate in a monopole fashion when the four inner conductors of the quadraxial feed are excited in-phase. With each of the inner conductors of the feed connected to one of the dipole arms, the quad-mode antenna allows for a further two orthogonal dipole-over-ground radiation patterns when the opposing inner conductors are excited out-of-phase. The most important aspect of such an antenna is the possibility of judiciously combining excitations in order to improve antenna parameters such as FoV, polarisation discrimination and sensitivity. This is illustrated for various antenna configurations, and it is shown that significant improvements can be achieved.

In order to characterise the multi-mode performance of these antenna designs, generalised transformations are presented by which the S-parameters and radiated far-fields of an N-port multi-mode antenna can be transformed into the equivalent response corresponding to excitations comprising linear combinations of the Single-Ended (SE) ports. These transformations are validated through the measured response of a dual-mode and quad-mode antenna design. Following these transformations, an equivalent network representation of an active multi-mode antenna connected to N SE Low-Noise Amplifiers (LNAs) is proposed for the case where the linear combination of the SE antenna excitations form N orthogonal modes. Using the equivalent multi-mode representation, further transformations are presented by which the S-parameters and noise parameters of the LNAs associated with each orthogonal multiconductor excitation can be solved from the corresponding SE S- and noise parameters of the LNAs. Finally, with the equivalent multi-mode response of the active antenna receivers defined, beamforming techniques normally applied to conventional single-mode phased arrays are introduced and used to assess the gain, sensitivity, and polarimetric performance of the presented multi-mode antenna designs. The performance of the active multi-mode antennas are compared with conventional purely differential antennas to illustrate the improvement in FoV coverage, as well as polarimetric performance achieved by the proposed dual-mode and quad-mode antenna designs.

The primary and secondary original contributions of this dissertation are listed below.

Primary Contributions

- A dual-mode antenna fed through a single twinaxial feed, allowing for both differential- and common-mode excitations that radiate typical dipole-over-ground and monopole far-field distributions resonant at the same frequency [2, 3].
- A quad-mode antenna integrating two orthogonal dipole antennas and a monopole excited through a quadraxial transmission line feed supporting four orthogonal TEM excitation modes. Exciting the quad-mode antenna with each orthogonal mode results in a unique radiation pattern that collectively provide near-hemispherical FoV coverage [4, 5, 6].
- Generalised transformations through which the equivalent S-parameters and radiated far-field patterns corresponding to linear combinations of the SE excitations of an N-port multi-mode antenna can be solved from the measured or simulated SE response [7].
- Transformations expressing the equivalent noise parameters and S-parameters corresponding to N orthogonal multiconductor TEM modes of N identical SE LNAs, in terms of the two-port S-parameters and noise parameters of the SE LNAs [3].

Secondary Contributions

- Coefficient matrices relating the SE voltages and currents of a quadraxial transmission line to four orthogonal modes each exciting the four inner conductors with equal magnitudes.

- Equivalent model of an active multi-mode antenna as well as an active multi-mode polarimeter excited through N excitation modes each radiating a unique far-field pattern.
- Implementation of beamforming algorithms on a single multi-mode antenna element to assign complex weight values to individual excitation modes in order to maximise the gain, sensitivity and polarimetric performance of the single antenna over a hemispherical FoV coverage.

1.3 Layout of the Dissertation

The dissertation starts with an introduction to the phased antenna arrays proposed for the Square Kilometre Array (SKA) telescope in Chapter 2. The desired performance specifications for these arrays are summarised along with a detailed description of the state-of-the-art precursor arrays developed across the globe.

In Chapter 3 the concept of a multi-mode antenna is presented. Starting with the operating principle of a dual-mode antenna, it is illustrated that a single antenna element can be designed to allow for both differential- and common-mode excitation through a balanced transmission line feed. Transformations are derived to calculate the mixed differential- and common-mode S-parameters and radiated far-field patterns of the dual-mode antenna from conventional Single-Ended (SE) S-parameter and far-field measurements. Based on the operating principle of the dual-mode antenna, the concept of a multi-mode antenna element excited through a multiconductor transmission line feed supporting N orthogonal TEM excitation modes is presented. Generalised transformations are derived by which the S-parameters and radiated far-field patterns corresponding to the N orthogonal excitation modes can be solved from the SE S-parameters and far-field patterns excited through the N SE conductors of the multiconductor feed. Two quad-mode antenna designs are presented, a narrow band cylindrical quad-mode antenna and a conical quad-mode antenna operating over an improved frequency bandwidth. Using the generalised S-parameter and far-field transformations, the multi-mode performance of the conical quad-mode antenna is validated through SE measurements.

Chapter 4 presents an equivalent model of an active multi-mode antenna as well as a multi-mode polarimeter. It is shown that the active multi-mode antenna can be modelled as an N element array of coupled single-mode antenna elements, enabling the use of conventional beamforming algorithms to solve complex beamforming weights for each orthogonal excitation mode in order to maximise the gain, sensitivity and polarimetric performance of a single multi-mode antenna element over a hemispherical FoV coverage. The performance with respect to gain and sensitivity of an active dual-mode and active quad-mode antenna is assessed, and the improved performance achieved through the utilisation of additional excitation modes present in multiconductor antenna feeds is demonstrated by comparing the gain and sensitivity of the dual- and quad-mode antennas to conventional single and dual-polarised dipole antennas. Lastly, using the quad-mode polarimeter model it is illustrated that the conical quad-mode antenna is

able to discern the polarisation state of an incident electromagnetic wave front up to scan angles of 60° from zenith.

Finally, Chapter 5 concludes the dissertation and recommendations are given for future work.

Chapter 2

Aperture Arrays for the Square Kilometre Array

In recent years astronomers have developed a set of specifications for a next generation radio telescope that will aid them in their understanding of the phenomena that make up the universe. The radio telescope proposed to meet these specifications is the Square Kilometre Array (SKA) telescope [8].

To cover the desired operating frequency bandwidth of the SKA telescope, ranging from 50 MHz up to 20 GHz, three different receiver topologies have been proposed – each designed to achieve a unique set of science goals [9]. These include, sparse antenna arrays – referred to as Aperture Arrays (AAs) – for the lower frequency band (50 MHz to 350 MHz), dense AAs operating between 350 MHz and 1 GHz, as well as an array of reflector antennas operating from 350 MHz up to 20 GHz. This chapter provides a brief introduction to the AA technology considered for the SKA, highlighting the performance requirements of the arrays in Sec. 2.1, and summarising the performance of the state-of-the-art sparse and dense aperture arrays in Sec. 2.2.

2.1 Aperture Array Technology

In radio astronomy, phased antenna arrays are normally referred to as Aperture Arrays (AAs). For sufficiently large arrays consisting of individually excited antenna elements, beam patterns can be formed and steered through the use of an electronic beamformer. By altering the phase of the signal induced in the individual antenna elements and summing the signals to form a single output, the resulting beam can be pointed anywhere on the sky – analogous to the mechanical steering of parabolic reflectors. Given that both the phase and the magnitude of the signals received by each element can be altered, AAs provide additional control over the shape of the resulting beam pattern. Furthermore, multiple beams can be formed simultaneously with various elements of the array, using separate beamformers to create each of the individual beams, allowing for a large aggregated instantaneous Field-of-View (FoV) [1, 10].

2.1.1 Desirable specifications

To meet the science requirements set out for the SKA telescope a number of performance specifications have been defined for the receivers of the SKA. The specifications of each receiver topology are summarised in [1], and only the desirable specifications for the AA receivers are discussed in this section.

Sensitivity

The weakest point-like source that can be detected in a given observation time is proportional to $T_{\text{sys}}/A_{\text{eff}}$, with T_{sys} denoting the system temperature and A_{eff} the effective area of the telescope. Telescope sensitivity is defined as the inverse of this ratio [8], that is

$$\text{Sensitivity} = \frac{A_{\text{eff}}}{T_{\text{sys}}}. \tag{2.1}$$

For the SKA a receiving sensitivity of at least 10 000 m^2/K is desired. This system sensitivity requirement therefore not only implies an extremely large collecting surface, but also places stringent requirements on the noise performance of the AAs.

Survey speed

The observing time required to detect point-like sources within the Field-of-View (FoV) of a telescope is proportional to $(T_{\text{sys}}/A_{\text{eff}})^2$, where the FoV is defined by the solid angle Ω over which the sensitivity of the telescope is greater that half the maximum sensitivity [8]. In recent years survey speed has not been considered as a design specification for radio telescopes, but a number of the science goals proposed for the SKA can only be achieved through AAs with large survey speeds. Therefore a Survey Speed Figure of Merit (SSFoM) has been established for the AA receivers of the SKA [1]. This SSFoM is defined as the ratio of the FoV (Ω) to the observation time required to detect point-like sources of specified strength, that is $(A_{\text{eff}}/T_{\text{sys}})^2\,\Omega$. The SSFoM of an AA can therefore be increased by increasing either the sensitivity or the FoV. Since the likelihood of detecting new phenomena is increased by viewing more of the sky, a large FoV is preferred when comparing receiver technologies with comparable survey speeds [1].

Polarisation discerning capability and sky coverage

Discerning the polarisation state of radio emissions from celestial sources is another key requirement for the SKA receivers [11]. For an ideal array where mutual coupling between the constituent antenna elements can be neglected, the array beam is obtained by multiplying the element pattern of a single array antenna element with the array factor of the array [12]. It therefore follows that the polarisation characteristics of the antenna array is largely determined by the polarisation characteristics of the constituent antenna element patterns [10]. To discern

the polarisation state of an incident field, two co-located and orthogonally oriented antenna elements are normally placed at each position within the array. Despite the broad beam pattern of electrically small antennas, the variation in gain at angles of incidence below zenith results in a directional variation in the polarization characteristics of the narrower array beam. To meet the desired SKA specifications, the AA receivers should be able to discern the polarisation state of incident fields up to scan angles of 60° from zenith [1].

2.1.2 Sparse and dense aperture arrays

For the frequency range from 50 MHz to 1 GHz, sparse and dense AAs have been identified as the optimal receiver technologies to meet the desired sensitivity specification. Sparse AAs refer to an array of antennas where the element spacing is greater than half the wavelength of the highest operating frequency. Alternatively, a dense AA refers to an array where the element spacing is less than half the shortest operating wavelength.

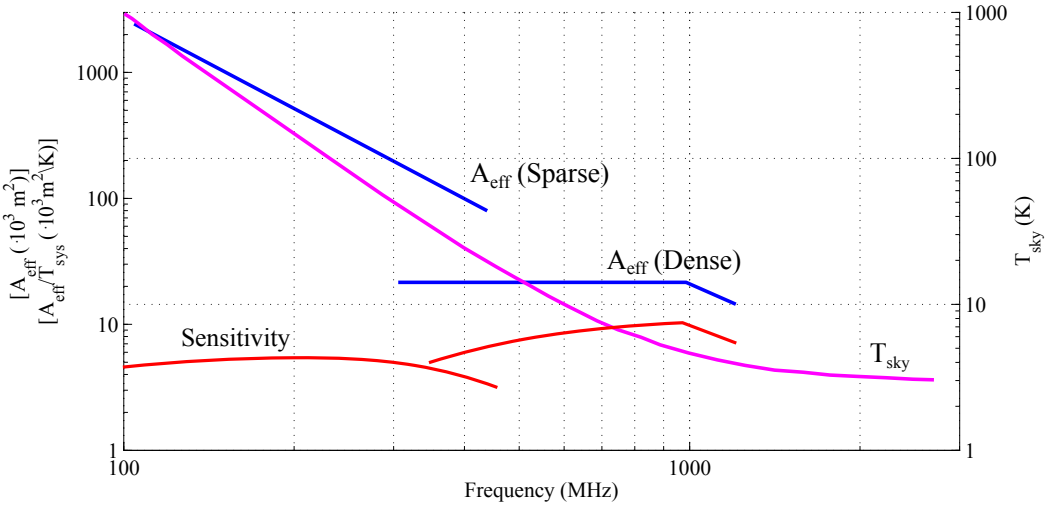

Figure 2.1: Sky noise contribution over frequency indicating the frequency bands for sparse and dense aperture arrays [13].

As indicated in Fig. 2.1, the sky noise temperature is significantly higher at the lower frequency band than at the middle and higher frequency bands. A sparse AA is therefore the most suited receiver technology to meet the SKA sensitivity specification for the frequency band ranging from 50 MHz to 350 MHz – since the effective area of each antenna element increases with λ^2 [14]. The sky noise is seen to reduce at frequencies higher than 300 MHz, allowing for the use of large dense AAs. The dense AAs form a collecting surface that essentially remains constant over frequency – up to an operating frequency where the element spacing become greater than half the wavelength – and is able to completely sample an incident electromagnetic wave [13]. Given that the number of antenna elements required to achieve the sensitivity specification using a dense AA increases quadratically with frequency, large reflector antennas become more cost effective at frequencies above 1 GHz.

2.2 Demonstrator Arrays

To demonstrate that sparse and dense AAs are viable options for the receivers of the SKA, a number of precursor telescopes are being developed by institutes across the globe. The most successful sparse demonstrator arrays include, the LOw Frequency ARray (LOFAR), Long Wavelength Array (LWA), Murchison Widefield Array (MWA), as well as a more recent Aperture Array Verification System 0.5 (AAVS 0.5) constructed using the SKA Log-periodic Antenna (SKALA). For the dense AA technology the most promising demonstrator arrays include, the Electronic Multi-Beam Radio Astronomy ConcEpt (EMBRACE), Octagonal Ring Antenna (ORA) array, and the FG-IGN: Fundación General Instituto Geográfico Nacional - Differential Active Antenna Array (FIDA3). This section gives a description of the antenna elements implemented in each of the sparse and dense demonstrator arrays, highlighting the recently documented performance achieved with each array.

2.2.1 Sparse aperture arrays

From Sec. 2.1 the lower frequency band for the SKA requires receivers with large effective areas to overcome the high sky noise present at these frequencies. The broad radiation patterns produced by linear wire antennas therefore make dipoles a cost effective option for sparse AAs to realise a large effective area over a wide scan range. The dipole-like antennas designed to provide the required effective area for each sparse demonstrator array are summarised in this section.

LOFAR

Developed by the Netherlands Institute for Radio Astronomy (ASTRON), the LOFAR telescope has been an important pathfinder to demonstrate the phased array concept for radio astronomy applications [15]. Designed to operate within the frequency band ranging from 10 MHz to 240 MHz, the phased array telescope consists of 48 sub-arrays, referred to as *stations*, with 40 stations located in the Netherlands and a further eight international stations located across Europe. To cover the entire frequency band, each station comprises two distinct antenna arrays: a 96 element sparse array operating from 10 MHz to 90 MHz, and a more dense 48 element – or 96 element for international stations – array operating from 110 MHz to 240 MHz. The array antenna elements used for each frequency band, referred to as the Low Band Antenna (LBA) and High Band Antenna (HBA), are shown in Fig. 2.2.

Shown in Fig. 2.2(a), the LBA element is realised by two co-located, perpendicular inverted-V dipole antenna elements, making the LBA element sensitive to two orthogonal polarisations [15]. Each dipole is supported by a 1.7 m high, vertical PVC shaft housing two coaxial cables carrying the signals induced on the respective dipole elements. At the top of the shaft, two differential Low-Noise Amplifiers (LNAs) convert the differential signal of each orthogonal dipole

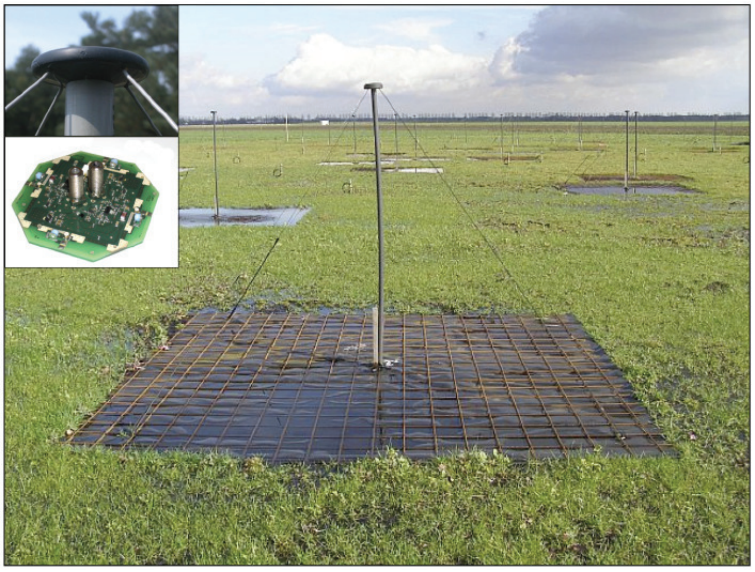

(a)

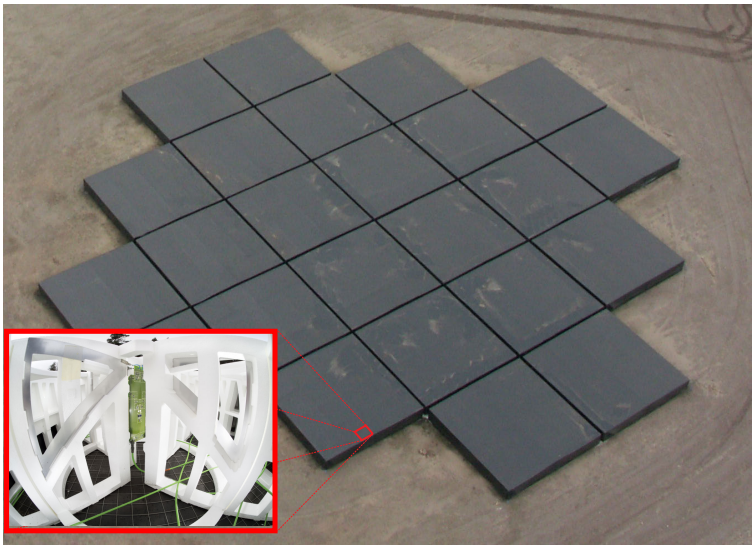

(b)

Figure 2.2: LOFAR (a) LBA [16] and (b) HBA array elements [17].

into unbalanced signals transmitted along the inner coaxial cables. Each dipole is constructed using 1.38 m long, collinear copper wires extending in opposite directions from the top of the centre shaft toward the ground plane at 45° angles with respect to the vertical shaft. The ground plane of the LBA element is realised as a 3 m × 3 m metal mesh placed on a square foil sheet of similar size. Despite this simple design, the simulated LBA performance indicate half-power beamwidths ranging between 77° – 85°, from 30 MHz to 80 MHz, in the E-plane and above 115°, over the entire frequency band, in the H-plane [15].

Figure 2.3 shows an aerial view of nine of the core LOFAR stations, located in the Netherlands, where each station consists of an array of 96 LBA elements and 48 HBA elements. To effectively utilise the broad beam patterns of the LBA elements, the station configuration allows each of the LBA elements to be excited individually through the implementation of a digital beamformer

Figure 2.3: An aerial view of core LOFAR stations located in the Netherlands showing six stations located on the circular island and three additional stations located in the lower left and upper right corners [16].

[16]. The LBA elements are positioned to form a dense core in the centre of the array, with a minimum element spacing of 2.4 m, and extend outward in a pseudo-random exponential taper – allowing for the use of sparse array configurations at the both the lower and higher ends of the frequency band [18].

To cover the frequency band from 110 MHz to 240 MHz each LOFAR station consists of a second array of HBA elements. Similar to the LBA array, each HBA element is sensitive to two orthogonal polarisations. The HBA [c.f. Fig. 2.2(b)] is realised by two co-located, perpendicular bow-tie dipole antennas constructed from aluminium plates with a pitch of 1.25 m and a height of 0.45 m. To position the antennas upright, each dual-polarised HBA element is housed in a square polystyrene structure [16]. The HBA array is constructed as a grid of 5 m $\times$ 5 m sub-arrays referred to as *tiles*. Each tile comprises a grid of 4 $\times$ 4 dual-polarised HBA elements, where analogue beamformers are used to combine the outputs of the 16 elements of each polarisation within the tile. Combining the signals within each tile extends the effective area at minimal cost [19].

LWA

The Long Wavelength Array (LWA) is a sparse phased array radio telescope, under construction in New Mexico near the Very Large Array (VLA), operating in the frequency band ranging from 10 MHz to 88 MHz [21]. Upon completion, the LWA will consist of 53 stations each consisting of 256 dual-polarised dipole-like antenna elements. The first station referred to as LWA1 [c.f. Fig. 2.4(a)] was completed in 2011 and consists of 256 antenna elements configured in a sparse array configuration with a minimum element spacing of 5.4 m [20]. The LWA antenna, shown in Fig. 2.4(b), consists of two co-located and perpendicular wire-grid bow-tie dipole antennas each with an arm length of 1.5 m.

In order to broaden the antenna beam the dipole arms of the LWA antenna are bent downwards

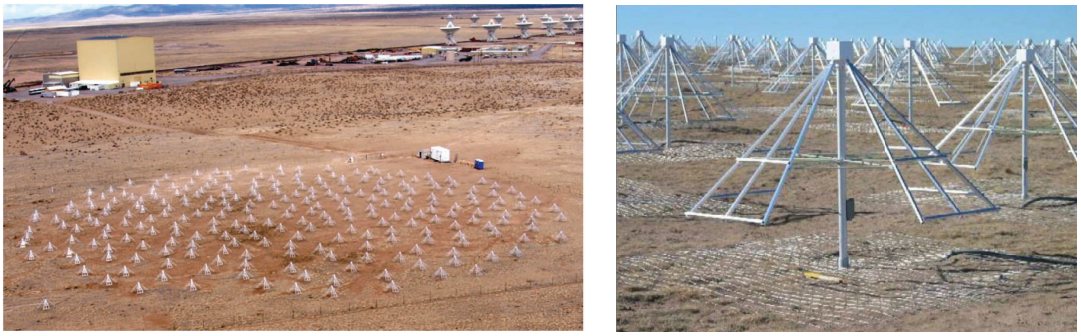

(a) (b)

Figure 2.4: The Long Wavelength Array (a) station LWA1 (b) LWA dual-polarised bow-tie dipole antenna [20].

toward the ground at 45° from the central feed point . The feed point is located at 1.5 m above a 3 m × 3 m wire-gird mesh acting as a ground plane to the antenna. Two differential LNAs, each realised with two single-ended (SE) LNAs connected to a balun, are positioned at the feed point to transform the differential signals induced in each polarisation into two unbalanced signals. The resulting beam of each element has a half-power beamwidth ranging between 82° – 96° in the E-plane and 102° – 116° in the H-plane between 20 MHz and 80 MHz [22].

MWA

Located at the official SKA sparse AA site in the Murchison region of outback Western Australia, the Murchison Widefield Array (MWA) is another state-of-the-art dipole-based AA telescope designed to operate over the frequency range from 80 MHz – 300 MHz [23]. Completed in 2013, MWA consists of a total of 2048 dual-polarised bow-tie antennas arranged in 128 tiles, each comprising a 4 × 4 array of dipoles. The dual-polarised dipole elements are realised by two vertically mounted, co-located and perpendicularly oriented bow-tie antennas with a span of 0.74 m [24].

Figure 2.5: One of the 128 tiles of the Murchison Widefield Array showing 16 bow-tie dipole elements above a square wire-grid mesh [25].

At the centre feed point of the antenna, the arms of each dipole element are connected to two SE LNAs and converted to an unbalanced output through a balun placed at the output of the LNAs. Through the use of dielectric spacers the antennas are positioned upright at an approximate distance of 0.1 m above a 5 m × 5 m wire-grid mesh ground plane and 1.1 m from one another within each tile, resulting in the tile configuration shown in Fig. 2.5 [25]. As a result of the finite ground plane the antenna patterns only allow for array pointing directions up to 60° from zenith.

AAVS 0.5 (SKALA)

As part of the Aperture Array Verification System (AAVS) initiative, coordinated by the Aperture Array Design and Construction (AADC) consortium, a second SKA demonstrator array is under construction at the Australian core site [26]. The array (AAVS 0.5), shown in Fig. 2.6(a), is being tested and constructed in collaboration with the existing MWA precursor telescope. At present AAVS 0.5 consists of a pseudo-random circular array of 16 dual-polarised antennas with an operating frequency range covering the entire lower frequency band proposed for the SKA – 50 MHz to 350 MHz.

(a) (b)

Figure 2.6: The Aperture Array Verification System 0.5 (a) 16 element SKALA array [27] (b) SKALA element [28].

The antenna element, shown in Fig. 2.6(b), dubbed the SKA Log-periodic Antenna (SKALA), is realised by four 1.6 m high arms configured as a dual-polarised log-periodic dipole array with nine interleaved, wide dipoles per polarisation. Each arm is positioned at a 10° opening angle with respect to the vertical centre of the antenna and extends downward to 0.3 m from the ground, covering a 1.3 m × 1.3 m ground area [29]. Simulated performance of the SKALA element with an infinite ground plane show half-power beamwidths ranging between 70° – 80° in the E-plane and 100° – 150° in the H-plane between 70 MHz and 300 MHz.

2.2.2 Dense aperture arrays

For frequencies above 300 MHz it becomes more effective to form a large collecting surface using a dense AA of connected antenna elements. These dense AA tiles form a collecting surface that essentially remains constant over frequency. The constant effective area together with the reduced sky noise contribution at these frequencies place stringent requirements on the noise contributed by the dense AA receivers. To ensure optimum sampling of an incident electromagnetic wave front across the mid SKA frequency band the element spacing within a dense AA for the SKA should be close to half a wavelength at 1 GHz, resulting in strong coupling between the array antenna elements. Effective use of coupling between elements – referred to as mutual coupling – can provide increased operating bandwidth using antenna elements with relatively narrow bandwidth when implemented as an isolated element [30]. As reported in [30], further improvement in impedance stability over the frequency band can be obtained – especially at wide scan angles – through the use of dielectric slabs positioned above the antenna elements. The dense AA demonstrators introduced in this section consist of two types of antenna elements. These include tapered slot antennas implemented in EMBRACE and FIDA3, as well as an array of planar ORA elements connected through additional coupling capacitors which, together with a meta-material slab acting as a dielectric layer, provide improved impedance stability over a large bandwidth.

EMBRACE

The Electronic Multi-Beam Radio Astronomy Concept (EMBRACE) demonstrator is a large scale AA conceived to illustrate that a low cost AA is a viable option for the dense AAs of the SKA. The demonstrator consists of two stations situated in Nancay in France and Westerbork in the Netherlands. At present the Westerbork array, shown in Fig. 2.7(a), is the larger of the two stations consisting of more than 20 000 antenna elements [31].

(a) (b)

Figure 2.7: EMBRACE (a) Westerbork station comprising over 20 000 [32] (b) tapered slot antenna elements [33].

The array comprises 144 tiles each containing 72 dual-polarised tapered slot (Vivaldi) antenna elements operating in the frequency band ranging from 500 MHz to 1500 MHz. All antenna elements within a tile are connected to one another, with the bordering elements of each tile connected to the adjacent tiles, forming a 160 m^2 collecting surface. Figure 2.7(b) shows a single Vivaldi element with the microstrip to slot line transition acting as a balun through which the antenna is excited. The element spacing within each tile is 12.5 cm, placing the array in the dense regime for frequencies below 1.2 GHz. At frequencies above 1.2 GHz the element spacing becomes sparse, resulting in the appearance of grating lobes in the array beam pattern and a reduction in the effective area of the array at larger scan angles [34]. Given the size of EMBRACE, an infinite array approximation is used to predict the array performance. Preliminary studies indicate that the current EMBRACE element distribution allows for a scan range up to the horizon, but only achieving the SKA polarisation specifications up to scan angles of 45° from zenith [35].

FIDA3

Similar to EMBRACE, the FIDA3 demonstrator is a dense array of connected dual-polarised tapered slot antenna elements developed by the FG-IGN: Fundación General Instituto Geográfico Nacional in Spain. The demonstrator is under development to investigate the feasibility of a differential active antenna element operating in the mid SKA frequency band from 300 MHz to 1 GHz in a connected array environment. Given the large number of receivers required for the dense AA receivers, cryogenic cooling of the receivers is not a viable or cost-effective solution to minimize the noise contribution. The receivers will therefore be operated at ambient temperature. Since the implementation of a balun in front of the LNA in the receiving chain increases the noise contributed by the receiver at ambient temperature, the differential active antenna elements of the FIDA3 demonstrator excite each tapered slot antenna through a balanced transmission line feed connected to a differential LNA [36] – removing the need for a balun and thereby reducing the system noise.

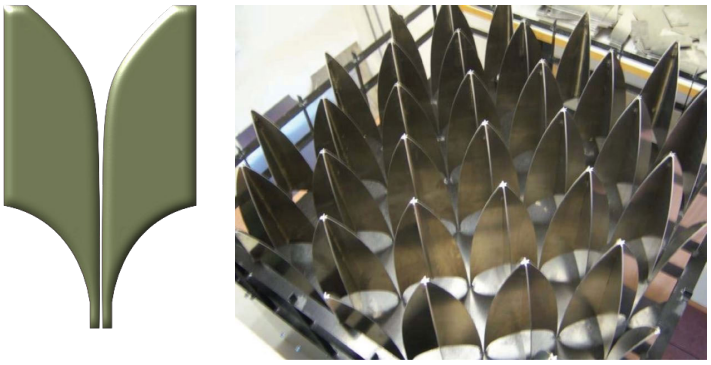

(a) (b)

Figure 2.8: FIDA3 (a) Bunny-ear tapered slot antenna (b) 64 element array tile [36].

Using infinite array simulations the bunny-ear element [c.f. Fig. 2.8(a)] has been optimised to illustrate that a large connected array of differentially excited elements can provide a low input VSWR over the desired frequency range. When scanning to broadside, these simulations show an input VSWR below 2.5 over the frequency range from 300 MHz to 1 GHz. During the antenna optimisation process, impedance anomalies appeared at certain frequencies within the operating frequency band, when scanning to angles off broadside, severely deteriorating the antenna performance at these frequencies. Further investigation into these anomalies showed that at certain scan angles even-mode currents are induced in the antenna feed, dominating the desired odd-mode currents through which the antenna elements are excited [37]. To reduce the effect of these undesired even-mode currents resistors have been connected between the ground plane and each of the transmission lines of the balanced feed, resulting in a reasonable suppression of these impedance anomalies at the expense of a 10 K increase in the system noise.

At present only a single tile consisting of 64 bunny-ear antennas [c.f. Fig. 2.8(b)], in a dual-polarised configuration, has been constructed. The measured system noise of the active array tile is reported in [36] showing the measured E- and H-plane radiation patterns of a single antenna element embedded within the tile. The measured embedded element pattern of the FIDA3 tile indicate that the differential active antenna element allows for a scan range up to 45° from zenith with less than 5 dB gain variation.

ORA

The Octagonal Ring Antenna (ORA) is a dense AA element designed as part of the SKA Design Studies (SKADS) initiative jointly run by the University of Cambridge, the University of Manchester, and the University of Oxford [11].

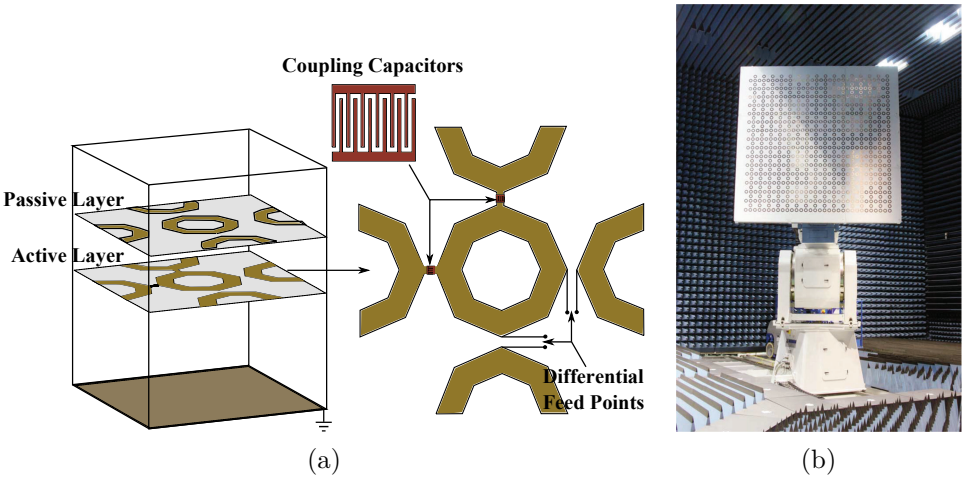

Figure 2.9: ORA (a) unit cell of single dual-polarised element (b) 256 element demonstrator array [38].

A single dual-polarised ORA element simulated as a unit cell with periodic boundaries is shown in Fig. 2.9(a). The element consists of two layers, an active radiating layer containing dual-

polarised elements connected to adjacent ORA elements through coupling capacitors and a passive superstrate meta-material layer positioned above the radiating layer [39]. Each element comprises three octagonal rings with two feed points exciting two orthogonal polarisations through a shared ring and two additional rings positioned at right angels with the shared ring [38]. The second passive layer positioned above the radiating ring element consists of a scaled down version of the three rings and act as a dielectric layer, improving the input impedance of the array at wide scan angles.

The dimensions of the ORA element has been optimised in an infinite array environment to achieve an operating bandwidth ranging from 300 MHz to 1 GHz. Simulations performed for an infinite array scanning from broadside to 45° illustrate that, for a differential port impedance of 150 Ω, stable input impedance characteristics can be achieved across the desired frequency band [39]. The peak broadside gain of the ORA element in an infinite array varies from -4 dB to 5 dB with frequency and results in a loss of 2 dB when scanning to 45°. To measure the performance of the ORA element in an array environment a 16 × 16 element array [c.f. Fig. 2.9(b)] has been constructed. The measured embedded element pattern of the central array element – excited through a co-planar waveguide to slot-line transition – show approximately 2 dB gain variation with scan angle over the operating bandwidth, allowing good polarisation performance over the scan range of ±45°.

2.3 Conclusion

This chapter introduces the desired performance specifications for the sparse and dense AA receivers for the lower and middle frequency band of the SKA telescope, and summarises the performance achieved by the state-of-the-art receivers implemented in a number of sparse and dense demonstrator arrays. All sparse demonstrator arrays are shown to implement dipole-like antenna elements with broad beam patterns to overcome the high sky noise contribution through a large effective area. Sparse demonstrator array antennas such as the LOFAR LBA and the LWA antenna achieve increased FoV by bending the arms of each dipole element toward the ground plane at 45°. These antenna designs are seen to result in at least 3 dB variation in gain when scanning along the E-plane up to 50° from zenith. The vertically oriented bow-tie elements implemented in the LOFAR HBA tiles and MWA achieve similar scan range performance with the gain of the MWA antennas reducing by at least 6 dB at 60° below zenith. In an attempt to cover the entire lower frequency band proposed for the SKA sparse AAs with a single antenna element, the Aperture Array Verification System demonstrator (AAVS 0.5) implements log-periodic dipole array elements. The log-periodic antennas (SKALA) are shown to achieve the desired operating frequency bandwidth, with the antenna gain decreasing by 3 dB in the E-plane for scan angles below 45° from zenith. Since sky noise is the dominant contributor to the total system noise, low noise contribution from the receivers are not essential at frequencies below 300 MHz.

At frequencies above 300 MHz, low-noise receivers become a critical requirement for the dense

AAs to achieve the desired sensitivity specifications for the SKA. For the mid frequency band of the SKA, dense AAs are envisioned to form a large collecting surface that essentially remains constant over frequency. Due to the number of elements required to form these collecting surfaces, the dense demonstrator arrays introduced in this chapter illustrate cost-effective antenna designs for the dense AAs of the SKA. These antenna designs include tapered slot antennas as implemented in EMBRACE and FIDA3 as well as the unconventional approach of the ORA array. At the price of reduced gain at the lower end of the frequency band, the ORA elements show the smallest gain variation for scan angles up to 60° from zenith, whereas the reduced gain at wider scan angles of the tapered slot antennas used by EMBRACE and FIDA3 only allow for a scanning up to 45° from zenith.

The differential nature of the antenna elements implemented in the precursor arrays enforces the use of baluns to convert the differential signal at the antenna feed to an unbalanced signal. If placed before the low-noise amplification stage, these baluns contribute unnecessary noise to the system noise of the receivers, especially for the receivers of the dense AAs. To circumvent this additional noise contribution, the FIDA3 demonstrator investigated an active differential antenna element, whereby the differential tapered slot antenna elements are excited differentially through differential LNAs. Despite the fact that these differential LNAs are designed to suppress common-mode propagation, these signals are still observed to be excited within the balanced transmission feed lines at certain scan angles, resulting in a deterioration of the desired differential-mode performance.

In the following chapter a single polarisation dual-mode antenna is introduced to overcome these impedance anomalies associated with undesired common-mode signals excited in the balanced transmission line feed. Instead of a purely differential antenna element, the dual-mode antenna integrates and co-locates dipole and monopole elements excited through a single balanced transmission line, thereby removing the need for a balun or purely differential LNA. It is shown that the co-located dipole and monopole elements allow for the utilisation of both differential- and common-mode signals, and results in two complimentary radiation patterns that allow for a near-hemispherical FoV coverage over which an array beam can be steered. It is worth noting that the concept of a single antenna element excited through both differential- and common-mode signals that radiate in typical dipole-over-ground and monopole-like fashion has recently been patented [40]. The design published in this patent describes a single polarisation antenna element for which the two respective radiation patterns are resonant at different frequencies, whereas the dual-mode antenna design presented here is an antenna element with integrated dipole and monopole elements that are resonant at the same centre frequency – thereby allowing for an extended FoV coverage. Based on the concept of the dual-mode antenna, further designs are presented in Chapter 3 including a cylindrical and conical quad-mode antenna design allowing for excitation through a single quadraxial transmission line supporting four orthogonal transverse electromagnetic modes. In Chapter 4 it is illustrated that these quad-mode antenna designs are able to discern the polarisation state of an incident electromagnetic wave front up to scan angels of 60° from zenith.

Chapter 3

Multi-Mode Antennas

As discussed in Chapter 2, this work proposes an antenna system utilising all or multiple modes propagating on multiconductor antenna feeds. It will be shown that antenna elements can be designed which produce a different radiation pattern for each excitation mode. This, in turn, creates the possibility of combining excitations to create combinations of the different far-field patterns, in this way allowing for an element with improved Field-of-View (FoV), polarisation discrimination or sensitivity, depending on the requirements of the designers. While the latter is discussed in Chapter 4, this chapter presents three multi-mode antenna elements which can be used for such a purpose. The concept of a multi-mode antenna using a narrowband single polarisation dual-mode antenna is first presented in Sec. 3.1. Based on the same operating principle a generalised network description of a multi-mode antenna excited through a multiconductor transmission line supporting multiple orthogonal port modes is presented in Sec. 3.2. Expressions are derived to transform the measured Single-Ended (SE) response of a multi-mode antenna into the equivalent response corresponding to the orthogonal transverse electromagnetic (TEM) port modes supported by the multiconductor transmission line. These transformations are used to assess the performance of two dual-polarised multi-mode antenna designs: a narrowband cylindrical quad-mode antenna and a conical quad-mode antenna operating over an improved frequency bandwidth presented in Sec. 3.3 and 3.4, respectively.

3.1 Dual-Mode Antenna

To illustrate the operating principle of a multi-mode antenna, a dual-mode antenna integrating a half-wave dipole and quarter-wave monopole element excited through a balanced transmission line supporting both Differential-Mode (DM) and Common-Mode (CM) propagation is presented. An overview of the operating principle of this dual-mode antenna element is given in Sec. 3.1.1 by first describing the conventional SE operation of the antenna when excited through two SE ports. Using the example of a balanced transmission line, the DM and CM signals are defined in terms of the SE signals propagating on the transmission line. This is used to describe the operation of the dual-mode antenna when excited by purely DM and CM excitations. In

Sec. 3.1.2, the DM and CM definitions are used to derive expressions by which the SE response of the dual-mode antenna can be transformed into the equivalent mixed DM and CM response. The dual-mode antenna design is discussed in Sec. 3.1.3, and used to illustrate the validity of the multi-mode antenna concept and the transformations derived in Sec. 3.1.2 using both simulated and measured results.

3.1.1 Operating principle of the dual-mode antenna

A schematic representation of the proposed dual-mode antenna element is shown in Fig. 3.1. The antenna integrates a dipole and a monopole element excited by a single balanced transmission line over an infinite ground plane. As depicted in Fig. 3.1, each arm of the dipole is connected to one of the lines of the balanced transmission line, and the monopole element is connected to the common ground conductor of the balanced transmission line.

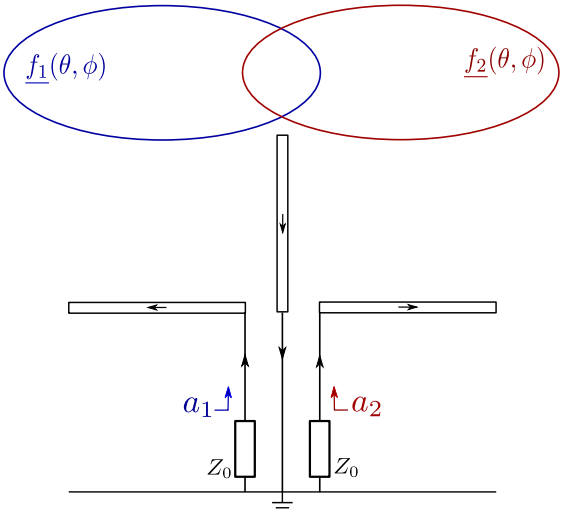

Figure 3.1: Schematic representation of the single-ended operation of a dual-mode antenna.

Figure 3.1 shows a single-ended (SE) excitation of the dual-mode antenna, with each of the constituent SE transmission lines of the balanced transmission line feed terminated in a characteristic impedance (Z_0) and individually excited by wave excitations a_1 and a_2. For this case of excitation, the radiated electric far-field can be described by the two SE radiation patterns, $\boldsymbol{f}_1(\theta,\phi)$ and $\boldsymbol{f}_2(\theta,\phi)$, and a SE two-port description can be obtained in the form of the scattering matrix $\mathbf{S}_{\mathrm{SE}}$.

Instead of the two SE excitations, the balanced transmission line can be excited by a second set of orthogonal modes, i.e a differential mode (DM) and common mode (CM). A differential-mode excitation is realised by exciting the two SE transmission lines with equal amplitudes but out-of-phase and a CM excitation by exciting them in-phase with equal amplitudes. To illustrate the characteristics of a DM and CM excitation, consider the graphic illustration of a pair of symmetric, terminated, coupled transmission lines over a ground plane, shown in Fig. 3.2.

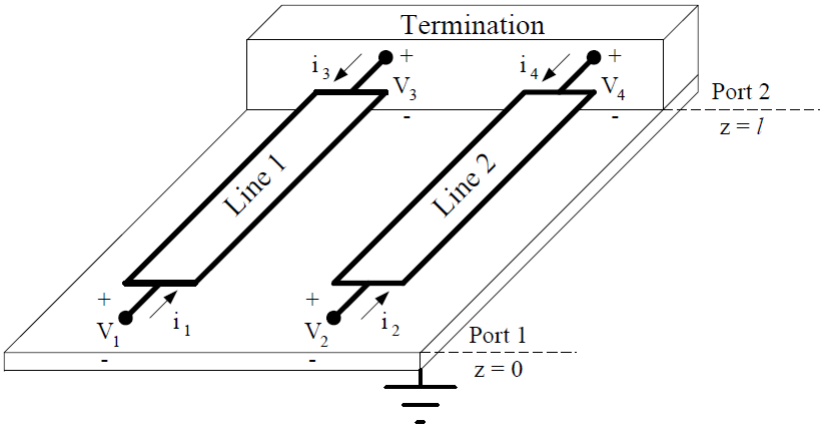

Figure 3.2: Symmetric, terminated, coupled transmission lines over a ground plane.

Inherently, the symmetric coupled transmission line supports two orthogonal ground-referenced propagation modes, namely odd- and even-modes, with respective characteristic impedances Z_{0o} and Z_{0e} [41]. Figures 3.3(a) and (b) show the transverse electric field line distribution for the odd- and even-mode, respectively.

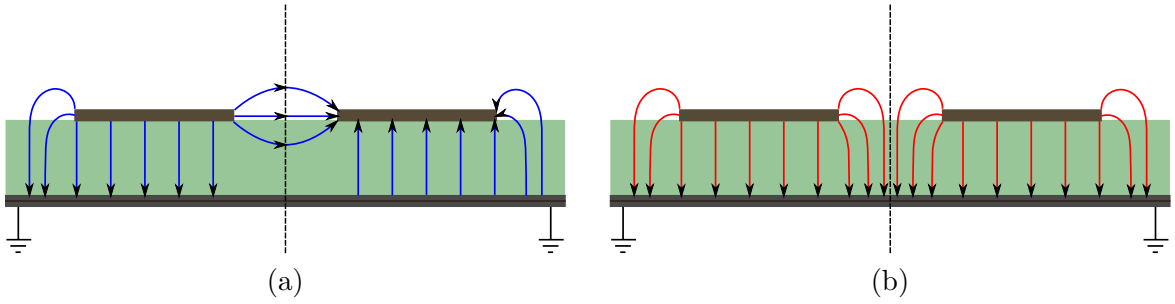

Figure 3.3: (a) Odd-mode and (b) even-mode electric field distribution.

From [42], the voltages and currents on the two lines can be expressed in terms of incident and reflected even- and odd-mode voltage waves as

$$v_1(z) = A_1 e^{-\gamma_e z} + A_2 e^{\gamma_e z} + A_3 e^{-\gamma_o z} + A_4 e^{\gamma_o z} \tag{3.1a}$$

$$v_2(z) = A_1 e^{-\gamma_e z} + A_2 e^{\gamma_e z} - A_3 e^{-\gamma_o z} - A_4 e^{\gamma_o z} \tag{3.1b}$$

$$i_1(z) = \frac{A_1}{Z_{0e}} e^{-\gamma_e z} - \frac{A_2}{Z_{0e}} e^{\gamma_e z} + \frac{A_3}{Z_{0o}} e^{-\gamma_o z} - \frac{A_4}{Z_{0o}} e^{\gamma_o z} \tag{3.1c}$$

$$i_2(z) = \frac{A_1}{Z_{0e}} e^{-\gamma_e z} - \frac{A_2}{Z_{0e}} e^{\gamma_e z} - \frac{A_3}{Z_{0o}} e^{-\gamma_o z} + \frac{A_4}{Z_{0o}} e^{\gamma_o z} \tag{3.1d}$$

where $\{v_1(z), v_2(z)\}$, and $\{i_1(z), i_2(z)\}$ denote the voltage and current on each line, $\{A_1, A_3\}$, and $\{A_2, A_4\}$, the phasor coefficients of the incident and reflected odd- and even-mode waves, and $\{\gamma_o, \gamma_e\}$, the odd- and even-mode propagation constants, respectively.

Defining differential- and common-mode propagation form a useful subset of the even and odd modes often implemented in the analysis of differential microwave circuits. A differential-mode

voltage (3.2a) is defined as the difference in voltage at any point (z) between lines 1 and 2, and is therefore no longer referenced to ground, implying that the DM current (3.2b) flowing into the one line returns through the other.

$$v_{\mathrm{DM}}(z) = v_1(z) - v_2(z) \tag{3.2a}$$

$$i_{\mathrm{DM}}(z) = \frac{1}{2}\left[i_1(z) - i_2(z)\right] \tag{3.2b}$$

The CM voltage (3.3a) is defined as the average voltage at any point (z) along the lines, hence the CM current (3.3b) is equal to the total current flowing into both lines which returns through the ground plane.

$$v_{\mathrm{CM}}(z) = \frac{1}{2}\left[v_1(z) + v_2(z)\right] \tag{3.3a}$$

$$i_{\mathrm{CM}}(z) = i_1(z) + i_2(z) \tag{3.3b}$$

Substituting the expressions for the voltage and current on each line (3.1a) – (3.1d) into the expressions for the DM and CM voltage and current (3.2a) – (3.3b), it can be shown that a DM signal is completely defined in terms of odd-mode waves propagating on the lines, and a CM signal is defined solely by even-mode propagation. A differential- and common-mode excitation therefore exhibits the same field line distribution as the odd- and even-modes depicted in Fig. 3.3(a) and (b), respectively. Using this result, the DM and CM characteristic impedances can be expressed in terms of the ground referenced odd- and even-mode characteristic impedances, where [42]

$$Z_{\mathrm{DM}} = 2Z_{0\mathrm{o}} \tag{3.4a}$$

$$Z_{\mathrm{CM}} = \frac{Z_{0\mathrm{e}}}{2}. \tag{3.4b}$$

In the case of an uncoupled balanced transmission line, as used for the dual-mode antenna feed illustrated in Fig. 3.1

$$Z_0 = Z_{0\mathrm{o}} = Z_{0\mathrm{e}} \tag{3.5}$$

in which case, the DM and CM characteristic impedances are related to the SE characteristic impedance by

$$Z_{\mathrm{DM}} = 2Z_0 \tag{3.6a}$$

$$Z_{\mathrm{CM}} = \frac{Z_0}{2}. \tag{3.6b}$$

Figures 3.4(a) and (b), respectively illustrate the differential- and common-mode operation of the dual-mode antenna [2]. When the antenna is excited by a DM excitation the two dipole arms are excited out-of-phase and no current is present on the monopole. The radiated electric field therefore is the typical dipole-over-ground radiation pattern ($\boldsymbol{f}_{\mathrm{DM}}(\theta, \phi)$). A common-mode excitation [c.f. Fig. 3.4(b)] is seen to excite the dipole arms in-phase and out-of-phase with

respect to the monopole element connected to the common ground, resulting in the monopole-like radiated electric field pattern ($\boldsymbol{f}_{\mathrm{CM}}(\theta,\phi)$). The equivalent DM and CM operation of the dual-mode antenna can therefore be described by the respective radiation patterns and an equivalent mixed differential- and common-mode two-port S-matrix ($\mathbf{S}_{\mathrm{MM}}$).

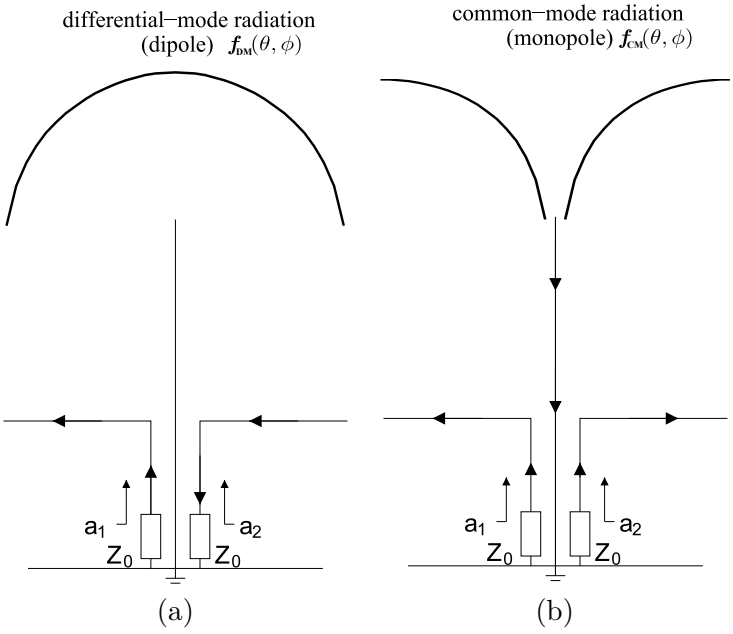

Figure 3.4: Operation of the dual-mode antenna for (a) differential- and (b) common-mode excitation.

3.1.2 Single-ended to mixed differential- and common-mode transformation

Measuring the differential- and common-mode S-matrix and radiated far-fields requires either the use of a balun and power divider or a vector network analyser that allows for a balanced port configuration. The equivalent SE S-matrix and radiation patterns, in comparison, can easily be obtained through standard measurements using a two-port vector network analyser. This section therefore introduces expressions by which the equivalent DM and CM operation depicted in Fig. 3.4 can be derived from the SE S-matrix ($\mathbf{S}_{\mathrm{SE}}$) and radiation patterns $\{\boldsymbol{f}_1(\theta,\phi)\,,\ \boldsymbol{f}_2(\theta,\phi)\}$.

First, consider the mixed DM and CM S-matrix. Following the derivation in [42], the DM (3.7) and CM (3.8) incident waves can be expressed in terms of the SE incident waves a_1 and a_2, using the definitions for the DM and CM voltages and currents (3.2a) – (3.3b). Hence

$$\begin{aligned} a_{\mathrm{DM}} &= \frac{1}{2\sqrt{\Re\{Z_{\mathrm{DM}}\}}}\left[v_{\mathrm{DM}} + Z_{\mathrm{DM}} i_{\mathrm{DM}}\right] \\ &= \frac{1}{\sqrt{2}}\left[a_1 - a_2\right] \end{aligned} \tag{3.7}$$

and

$$\begin{aligned} a_{\mathrm{CM}} &= \frac{1}{2\sqrt{\Re\{Z_{\mathrm{CM}}\}}}\left[v_{\mathrm{CM}} + Z_{\mathrm{CM}} i_{\mathrm{CM}}\right] \\ &= \frac{1}{\sqrt{2}}\left[a_1 + a_2\right] \end{aligned} \tag{3.8}$$

with

$$a_{\mathrm{n}} = \frac{1}{2\sqrt{\Re\{Z_0\}}}\left[v_{\mathrm{n}} + Z_0 i_{\mathrm{n}}\right] \quad \text{for} \quad \mathrm{n} = 1, 2. \tag{3.9}$$

Given the linear relation between the differential- and common-mode incident waves and the SE incident waves, the SE excitation of the dual-mode antenna can readily be transformed into the equivalent mixed differential and common-mode excitations using

$$\mathbf{a}_{\mathrm{MM}} = \mathbf{M}\,\mathbf{a}_{\mathrm{SE}}, \tag{3.10}$$

where $\mathbf{a}_{\mathrm{MM}} = [a_{\mathrm{DM}}\; a_{\mathrm{CM}}]^T$ and $\mathbf{a}_{\mathrm{SE}} = [a_1\; a_2]^T$ denote vectors containing the DM and CM, and SE incident waves respectively, and the transformation matrix $\mathbf{M}$ is given by

$$\mathbf{M} = \frac{1}{\sqrt{2}}\begin{bmatrix} 1 & -1 \\ 1 & 1 \end{bmatrix}. \tag{3.11}$$

In a similar fashion, the reflected differential- and common-mode waves can be related to the reflected SE waves, with

$$\mathbf{b}_{\mathrm{MM}} = \mathbf{M}\,\mathbf{b}_{\mathrm{SE}}, \tag{3.12}$$

where $\mathbf{b}_{\mathrm{MM}} = [b_{\mathrm{DM}}\, b_{\mathrm{CM}}]^T$ and $\mathbf{b}_{\mathrm{SE}} = [b_1\, b_2]^T$ denote vectors containing the DM and CM, and SE reflected waves. It follows from (3.10) and (3.12) that the mixed differential- and common-mode scattering matrix ($\mathbf{S}_{\mathrm{MM}}$) of the dual-mode antenna can be solved from the SE scattering matrix ($\mathbf{S}_{\mathrm{SE}}$), using the transformation [43]

$$\mathbf{S}_{\mathrm{MM}} = \mathbf{M}\,\mathbf{S}_{\mathrm{SE}}\,\mathbf{M}^{-1} \tag{3.13}$$

where $\mathbf{S}_{\mathrm{MM}}$ relates the incident DM and CM waves to the respective reflected waves. That is

$$\begin{aligned} \mathbf{b}_{\mathrm{MM}} &= \mathbf{S}_{\mathrm{MM}}\,\mathbf{a}_{\mathrm{MM}} \\ &= \begin{bmatrix} S_{\mathrm{dd}} & S_{\mathrm{dc}} \\ S_{\mathrm{cd}} & S_{\mathrm{cc}} \end{bmatrix} \mathbf{a}_{\mathrm{MM}} \end{aligned} \tag{3.14}$$

with $\{S_{\mathrm{dd}},\, S_{\mathrm{cc}}\}$ denoting the DM and CM input reflection coefficients, and $\{S_{\mathrm{dc}},\, S_{\mathrm{cd}}\}$ the coupling between the two modes.

With the DM and CM excitation of the dual-mode antenna defined in terms of the SE excitations, expressions can now be derived for the equivalent differential- and common-mode radiation patterns. To this end, consider the SE radiated electric field patterns defined in a set of spherical coordinates in the far-field region. That is, each SE radiation pattern is of the form

$$\boldsymbol{f}_{\mathrm{n}}(\theta, \phi) = f_{\mathrm{n}}^{\theta}(\theta, \phi)\,\hat{\boldsymbol{a}}_{\boldsymbol{\theta}} + f_{\mathrm{n}}^{\phi}(\theta, \phi)\,\hat{\boldsymbol{a}}_{\boldsymbol{\phi}} \quad \text{for} \quad \mathrm{n} = 1, 2 \tag{3.15}$$

where the superscripts θ and ϕ denote the orthogonal transverse components of the radiated electric field, corresponding to the unit vectors $\hat{\boldsymbol{a}}_{\boldsymbol{\theta}}$ and $\hat{\boldsymbol{a}}_{\boldsymbol{\phi}}$ in the spherical coordinate system, respectively. Given the linearity between the radiated electric fields and the excitation applied to the antenna port, the same transformation applied to the SE incident waves (3.10) can be applied to solve the components of the corresponding DM and CM radiation patterns. That is

$$\mathbf{F}^{\mathrm{p}}_{\mathrm{MM}} = \mathbf{M}\,\mathbf{F}^{\mathrm{p}}_{\mathrm{SE}} \quad \text{for} \quad \mathrm{p} = \theta, \phi \tag{3.16}$$

where $\mathbf{F}^{\mathrm{p}}_{\mathrm{MM}} = [f^{\mathrm{p}}_{\mathrm{DM}}(\theta,\phi)\ \ f^{\mathrm{p}}_{\mathrm{CM}}(\theta,\phi)]^T$, $\mathbf{F}^{\mathrm{p}}_{\mathrm{SE}} = [f^{\mathrm{p}}_{1}(\theta,\phi)\ \ f^{\mathrm{p}}_{2}(\theta,\phi)]^T$, and the transformation matrix $\mathbf{M}$ is given by (3.11).

Following, the transformations given in (3.13) and (3.16) are used to characterise the mixed differential- and common-mode performance of a narrowband dual-mode antenna design.

3.1.3 Dual-mode antenna design

As a first example of an antenna element utilising more than one excitation mode, a narrow-band dual-mode antenna design is presented in this section [3]. The dual-mode antenna combines a dipole and a cylindrical sleeve monopole element with a single twinaxial feed. As shown in Fig. 3.5(a), the cylindrical dual-mode antenna is realised by a single balanced transmission line feeding a dipole element over a ground plane, where each of the two centre conductors is connected to one of the dipole arms. The monopole is realised by folding the ground conductor of the twinaxial feed back towards the ground plane, leaving a small gap between the monopole and the ground shield of the feed (w_3) as well as the ground plane (g_1). Using the parameters indicated in Fig. 3.5(b), the dual-mode antenna can be designed such that both differential- and common-mode excitations produce resonance at the same centre frequency, in this case, at 1 GHz.

It is well known that optimal performance of a linearly polarised dipole over a ground plane is achieved when the length of the dipole is approximately half a wavelength and positioned a quarter wavelength above the ground plane. Starting from this point the dimensions L_1 and L_2 are solved for a centre frequency of 1 GHz. Next an air-core twinaxial transmission line of length L_2 is included, where the inner conductor diameter w_1, the conductor spacing s_1 and the ground shield diameter w_2 is solved such that the differential-mode characteristic impedance matches the real part of the input impedance of the dipole. As indicated in Fig. 3.5(b), the ground shield of the twinaxial transmission line extends a height L_3, or up to a distance L_4 from the dipole. The integrated monopole sleeve is realised by extending the ground shield radially outward a distance w_3 at the height L_3, and folding the shield back towards the ground plane leaving a small gap g_1 between the shield and the ground plane. Since the length of the monopole sleeve is shorter than the desired quarter operating wavelength of a conventional monopole, the resonant frequency of the monopole sleeve is slightly higher than that of the dipole when the sleeve is positioned too close to the ground shield. The resonant frequency of the common-mode excitation – i.e. the monopole sleeve – is lowered by extending the distance between the

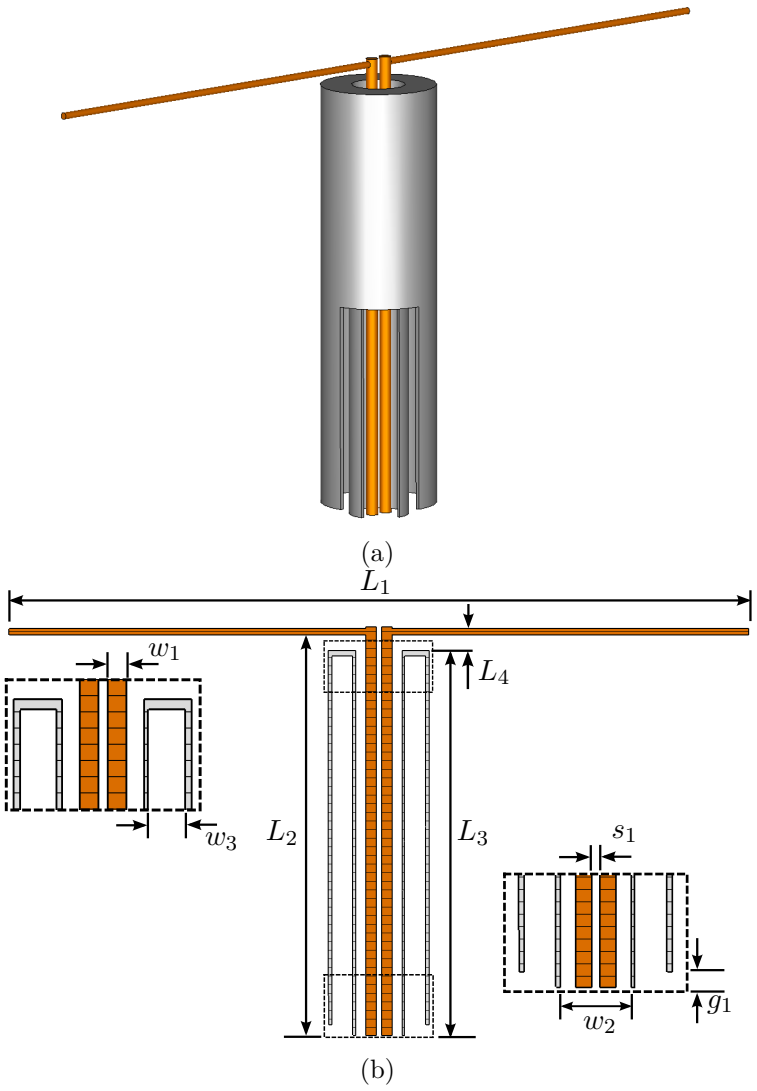

Figure 3.5: (a) Cylindrical dual-mode antenna (b) cross-sectional cut of the antenna design.

twinaxial transmission line feed and the sleeve (w_3) and adjusting the height L_3. Table 3.1 indicates the dimensions of the dual-mode antenna solved using CST Microwave Studio for a dipole arm diameter of 1.15 mm and a shield conductor thickness of 0.9 mm. The resulting effect of the monopole sleeve incorporated in the dual-mode antenna design is clearly seen when considering the Smith chart shown in Fig. 3.6.

The graph compares the differential- and common-mode input reflection coefficients of the dual-mode antenna with that of a conventional dipole antenna excited through a twinaxial transmission line, simulated using the same dimensions solved for the dual-mode antenna with the monopole sleeve excluded from the design. The curves show the input reflection coefficients over the frequency range from 0.7 GHz to 1.4 GHz, with the markers on each curve indicating the input reflection coefficient at 1 GHz. As seen, the differential-mode input reflection coefficient is nearly identical for both the conventional purely differential dipole and dual-mode antenna, with the common-mode input reflection coefficient of the dipole largely mismatched. Considering the common-mode input reflection coefficient of the dual-mode antenna, the monopole sleeve

Table 3.1: Design parameters of cylindrical dual-mode antenna depicted in Fig. 3.5(b).

Parameter	Value [mm]	Description
L_1	141	Dipole length
L_2	75	Dipole height
L_3	72	Feed/Monopole height
L_4	3	Dipole-Monopole separation
w_1	2	Feed inner conductor diameter
w_2	8.2	Feed ground shield inner diameter
w_3	3	Sleeve-Ground separation
g_1	2	Monopole-Ground plane gap height
s_1	2	Feed inner conductor separation

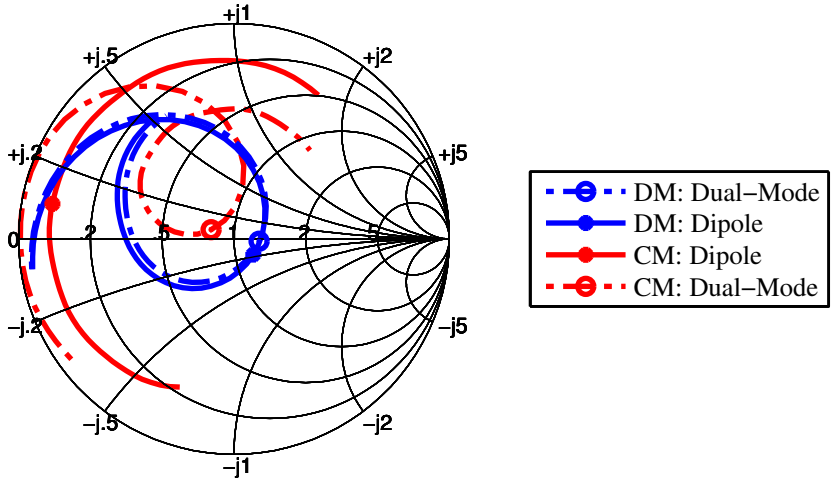

Figure 3.6: Differential- and common-mode input reflection coefficients of the dual-mode antenna compared with a conventional dipole antenna.

integrated into the dual-mode antenna design is seen to result in a common-mode resonance optimally matched at 1 GHz.

While illustrating the concept of a dual-mode antenna, the design in Fig. 3.5 suffers from a few disadvantages: a structurally weak air-core twinaxial feed and coupled ports which prohibit single-ended measurements. To realise a dual-mode antenna design that allows for conventional SE far-field and S-parameter measurement and improve structural aspects, modifications are made to the antenna design illustrated in Fig. 3.5. This modified cylindrical dual-mode antenna is shown in Fig. 3.7 [3]. The monopole sleeve is kept in place through a small Teflon spacer placed at the base of the antenna, and to ensure the stability of the centre conductors of the twinaxial transmission line a second Teflon spacer is placed at the top of the monopole sleeve. Two SE excitation ports are realised through the use of two 3 mm semi-rigid coaxial cables extending midway into the antenna feed (L_5), from which point the centre conductors of the semi-rigid coaxial cables extend further to form an air-core twinaxial transmission line. Table 3.2 summarises the antenna design parameters of the dual-mode antenna illustrated in Fig. 3.7.

The electric field distributions of the differential- and common-mode near fields and port field

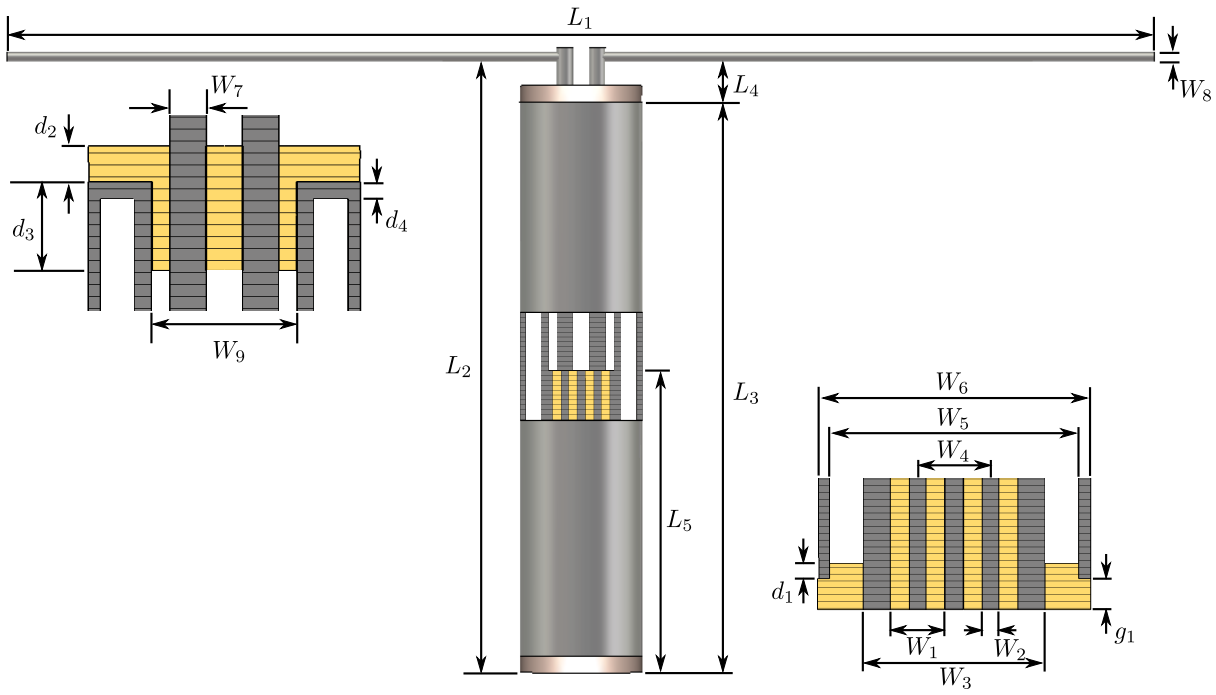

Figure 3.7: Cylindrical dual-mode antenna design with cut planes at the bottom, middle (semi-rigid coaxial to air-core twinaxial transition) and top of the antenna feed.

Table 3.2: Cylindrical dual-mode antenna design parameters.

Parameter	Value [mm]	Description
L_1	141	Dipole length
L_2	75	Dipole height
L_3	70	Feed/Monopole height
L_4	5	Dipole-Monopole separation
L_5	35	Height of twinaxial transition
W_1	3	Coaxial dielectric diameter
W_2	0.91	Coaxial conductor diameter
W_3	10	Feed ground shield outer diameter
W_4	5	Dipole/Feed line separation
W_5	13.66	Monopole sleeve inner diameter
W_6	15	Monopole sleeve outer diameter
W_7	2	Twinaxial inner conductor diameter
W_8	1.15	Dipole arm diameter
W_9	8	Twinaxial ground shield inner diameter
d_1	1	Monopole Teflon support
d_2	2	Twinaxial conductor Teflon support
d_3	5	Twinaxial conductor Teflon support
d_4	1	Monopole-Feed ground cap thickness
g_1	2	Monopole-Ground plane gap height

distributions of the antenna, simulated over an infinite ground plane in CST Microwave Studio, are shown in Figs. 3.8(a) to (d). The purely DM and CM excitations are simulated by defining potentials on each of the centre conductors of the twinaxial line, corresponding to the definitions of a DM and CM excitation given in (3.7) and (3.8), respectively.

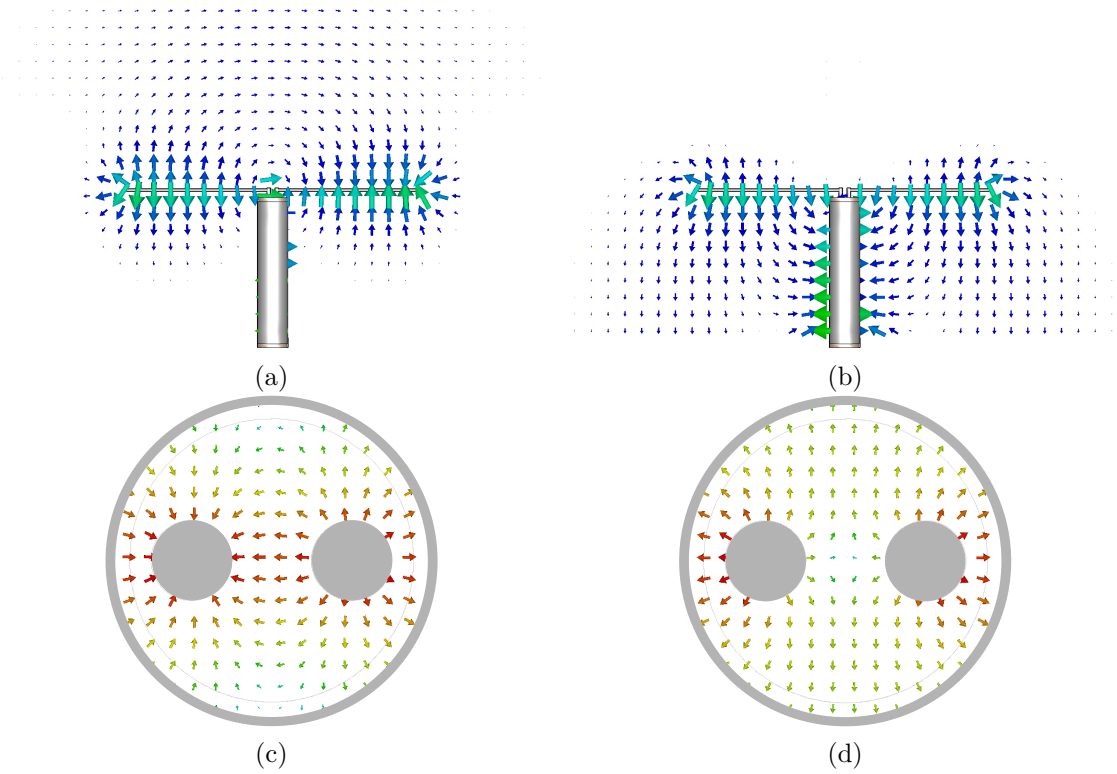

Figure 3.8: Simulated electric field distributions (a) DM antenna near field (b) CM antenna near field (c) DM port excitation (d) CM port excitation.

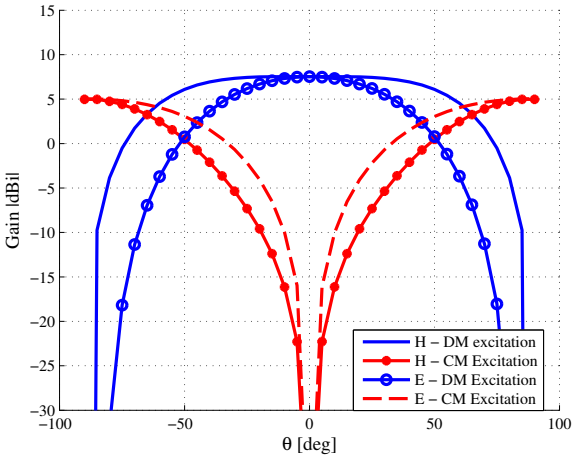

Figure 3.9: Differential- and common-mode E-plane and H-plane gain simulated at 1 GHz.

As described in Sec. 3.1.1, a DM field distribution in the balanced transmission line feed [c.f. Fig. 3.8(c)] is seen to excite the dipole arms out-of-phase, realising a typical dipole radiated electric near field [c.f. Fig. 3.8(a)]. A CM excitation realises the field distribution of the feed as depicted in Fig. 3.8(d) and is shown to excite the dipole arms in-phase, but out-of-phase with respect to the monopole sleeve, resulting in a monopole-like radiated electric near field [c.f. Fig. 3.8(b)]. Fig. 3.9 shows the normalised E- and H-plane differential- and common-mode gain patterns resulting from the DM and CM excitations depicted in Fig. 3.8. The curves in

Fig. 3.9 clearly illustrate that a typical dipole-over-ground radiation pattern is realised by a DM excitation, and that a CM excitation results in a monopole-over-ground radiation pattern.

In order to measure the performance of the antenna, the design illustrated in Fig. 3.7 is placed in the centre of a circular ground plane with a diameter of 500 mm, and excited through two 3 mm semi-rigid coaxial cables shown in Fig. 3.10.

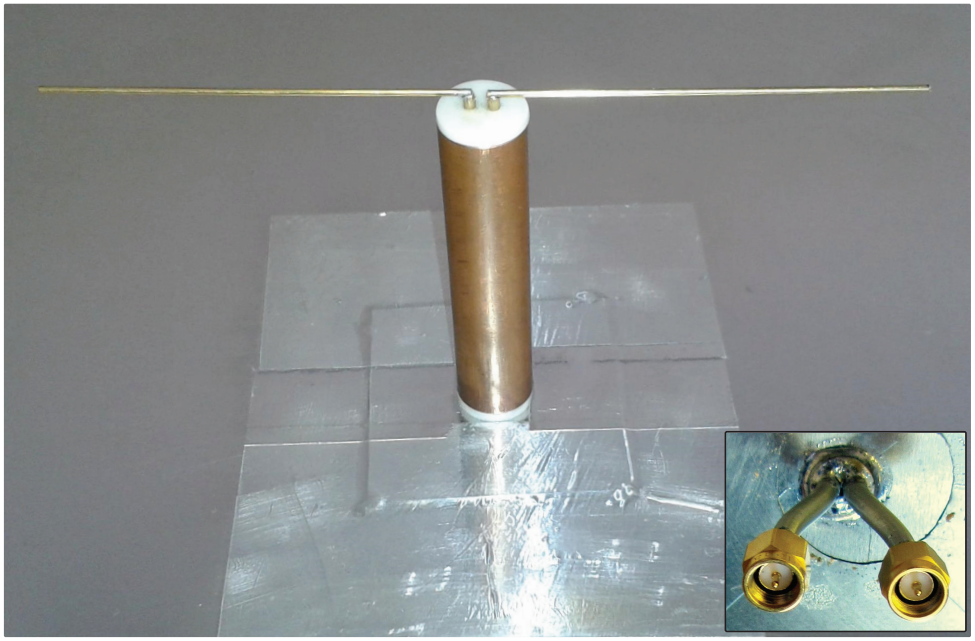

Figure 3.10: Dual-mode antenna on finite circular ground plane with 3 mm semi-rigid coaxial feeds.

Using (3.13), the DM and CM input reflection coefficients can be solved from the measured SE S-parameters of the antenna. The graph in Fig. 3.11 compares the measured differential- and common-mode input reflection coefficients to the simulated results obtained using purely DM and CM excitations in CST. Fig. 3.11 shows that the measurements agree very well with the simulated response, with both differential- and common-modes matched at the center frequency of 1 GHz. Also shown in Fig. 3.11 is the measured isolation between the DM and CM excitations calculated using (3.13). It is seen that an isolation below -30 dB is achieved. Given the orthogonal nature of the two excitation modes, the simulated isolation is below -60 dB across the indicated frequency band, and is therefore omitted from Fig. 3.11.

Similar to the reflection coefficients, the DM and CM radiation patterns are obtained by measuring the SE radiation patterns of the antenna and applying (3.16). The co-polar DM and CM radiation patterns measured and simulated at 1 GHz, in both principal planes, are compared in Fig. 3.12. The measured differential- and common-mode radiation patterns are seen to be in good agreement with the simulated response [c.f. Fig. 3.12] in both principal planes. It should be noted that the differences in the common-mode pattern of the measured antenna, shown in Fig. 3.12, and the radiation patterns depicted in Fig. 3.9 can be attributed to the finite ground plane used for the physical antenna. Regardless of these differences, the measurements still

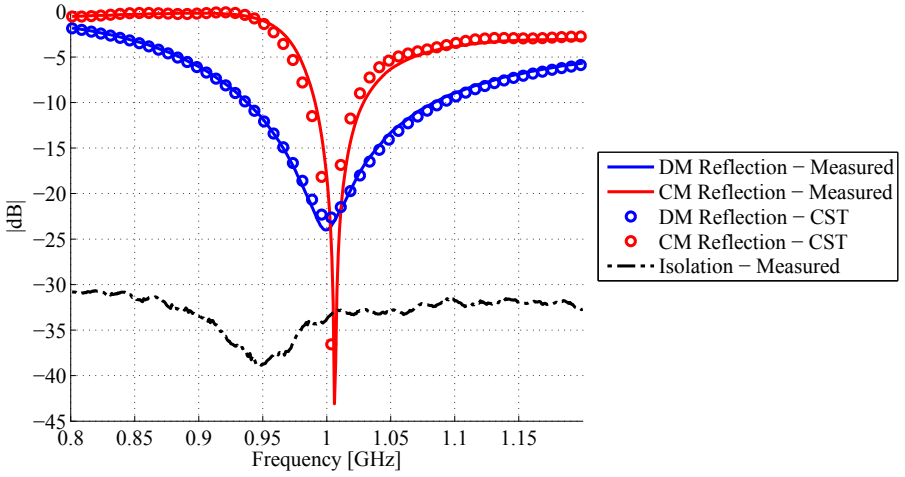

Figure 3.11: Measured and simulated differential- and common-mode input reflection coefficients and isolation.

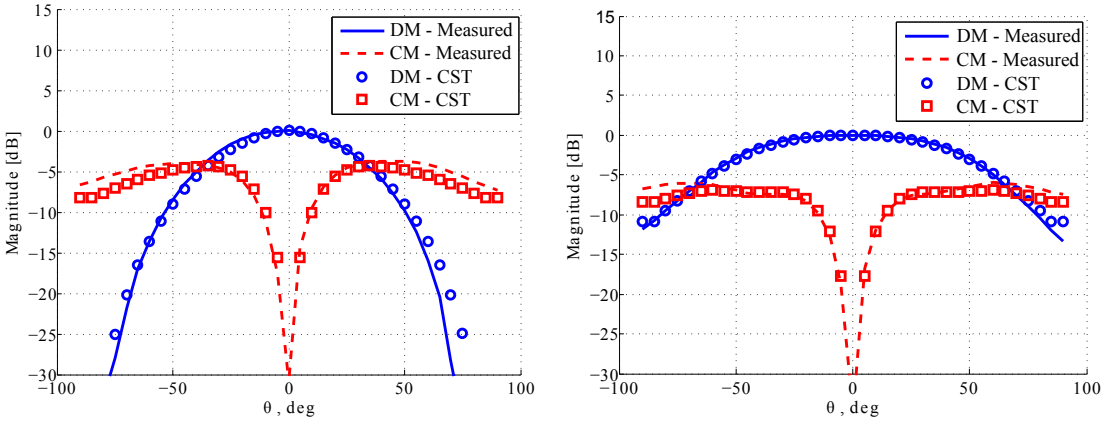

Figure 3.12: Measured and simulated co-polar differential- and common-mode radiation patterns (a) E-plane and (b) H-plane.

illustrate the dipole- and monopole-like radiation characteristics of the antenna resulting from differential- and common-mode excitations. Considering the complimentary radiation patterns excited by each mode, it can readily be seen from Fig. 3.9 that near-hemispherical FoV coverage can be obtained through judicious use of the differential and common excitation modes. This aspect is discussed in Chapter 4, where an equivalent mixed differential- and common-mode receiver model of an active dual-mode antenna is presented and used to solve complex beamforming weights that result in less than 50 % variation in sensitivity in the E-plane when scanning from $-90°$ to $90°$.

3.2 Transformations for Multi-Mode Antennas

The theory in Sec. 3.1 is not limited to two excitation modes, but can be generalised to the case of N-modes, as presented in the following section.

3.2.1 Generalised transformations for a multi-mode antenna

Consider a hypothetical antenna element excited through a multiconductor transmission line with N SE terminations, where the performance of the antenna is described by the SE S-matrix $\left(\mathbf{S}^{\mathrm{SE}}\right)$ and SE radiated electric field patterns $\left(\boldsymbol{f}_1^{\mathrm{SE}}(\theta,\phi)\right.$ to $\left.\boldsymbol{f}_{\mathrm{N}}^{\mathrm{SE}}(\theta,\phi)\right)$. The SE multiconductor antenna can be represented by the network illustrated in Fig. 3.13(a), indicating the SE voltage $\left(V_{\mathrm{n}}^{\mathrm{SE}}\right)$, current $\left(I_{\mathrm{n}}^{\mathrm{SE}}\right)$, the incident $\left(a_{\mathrm{n}}^{\mathrm{SE}}\right)$ and reflected $\left(b_{\mathrm{n}}^{\mathrm{SE}}\right)$ waves, as well as the characteristic impedance $Z_{0\mathrm{n}}$ at each port, n. Alternatively to the SE representation, the performance of the multiconductor antenna can be described by a multi-mode S-matrix $\left(\mathbf{S}^{\mathrm{MM}}\right)$ and radiated electric field patterns $\left(\boldsymbol{f}_1^{\mathrm{MM}}(\theta,\phi)\right.$ to $\left.\boldsymbol{f}_{\mathrm{N}}^{\mathrm{MM}}(\theta,\phi)\right)$ corresponding to N orthogonal transverse electromagnetic (TEM) port modes defined by linear combinations of the SE excitations. The multiconductor antenna can therefore be represented by a multi-mode network [c.f. Fig. 3.13(b)], where each port represents the voltage $\left(V_{\mathrm{n}}^{\mathrm{MM}}\right)$, current $\left(I_{\mathrm{n}}^{\mathrm{MM}}\right)$, incident $\left(a_{\mathrm{n}}^{\mathrm{MM}}\right)$ and reflected $\left(b_{\mathrm{n}}^{\mathrm{MM}}\right)$ waves, as well as the characteristic impedance $\left(Z_{\mathrm{n}}^{\mathrm{MM}}\right)$ associated with the n^{th} orthogonal mode.

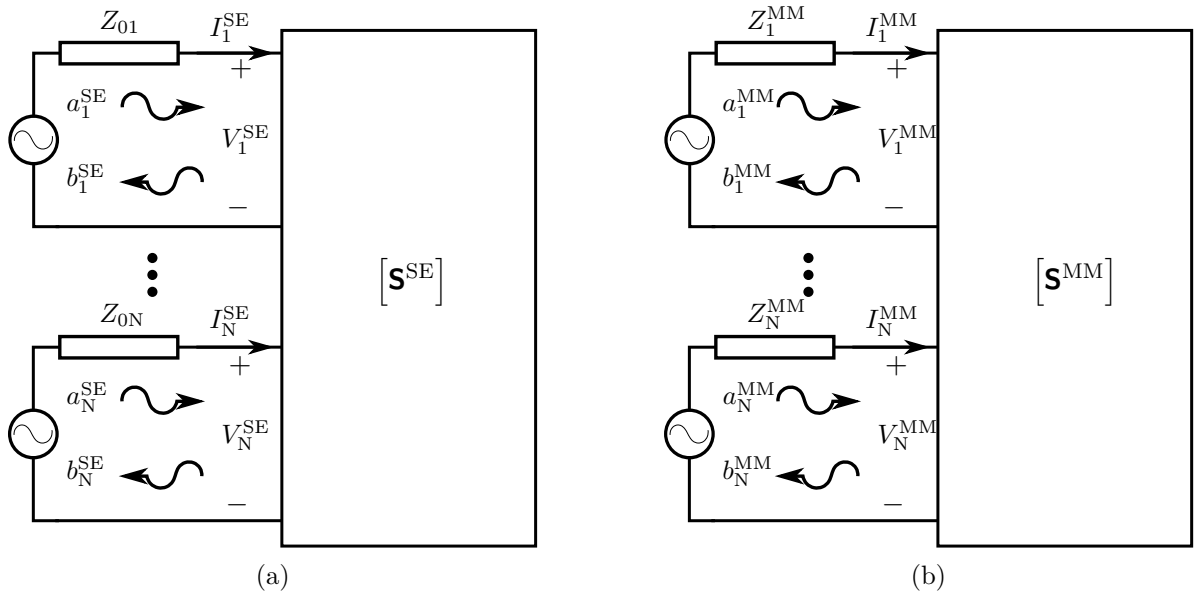

Figure 3.13: (a) Single-ended and (b) multi-mode schematic illustration of a multi-mode antenna.

To derive expressions by which the SE S-matrix and radiation patterns of the multi-mode antenna can be transformed into the equivalent S-matrix and radiation patterns corresponding to the orthogonal port modes, the multi-mode voltages and currents are first expressed as linear

combinations of the SE voltages and currents. That is,

$$\begin{aligned} V_{\mathrm{n}}^{\mathrm{MM}} &= k_{\mathrm{n1}}^{\mathrm{v}} V_1^{\mathrm{SE}} + k_{\mathrm{n2}}^{\mathrm{v}} V_2^{\mathrm{SE}} + \cdots + k_{\mathrm{nN}}^{\mathrm{v}} V_{\mathrm{N}}^{\mathrm{SE}} \\ I_{\mathrm{n}}^{\mathrm{MM}} &= k_{\mathrm{n1}}^{\mathrm{i}} I_1^{\mathrm{SE}} + k_{\mathrm{n2}}^{\mathrm{i}} I_2^{\mathrm{SE}} + \cdots + k_{\mathrm{nN}}^{\mathrm{i}} I_{\mathrm{N}}^{\mathrm{SE}} \end{aligned} \quad \text{for} \quad \mathrm{n} = 1, ..., N \tag{3.17}$$

or

$$\mathbf{V}^{\mathrm{MM}} = \mathbf{K}^{\mathrm{v}} \mathbf{V}^{\mathrm{SE}} \tag{3.18a}$$

$$\mathbf{I}^{\mathrm{MM}} = \mathbf{K}^{\mathrm{i}} \mathbf{I}^{\mathrm{SE}} \tag{3.18b}$$

where $\{\mathbf{V}^{\mathrm{MM}}, \mathbf{V}^{\mathrm{SE}}\}$ and $\{\mathbf{I}^{\mathrm{MM}}, \mathbf{I}^{\mathrm{SE}}\}$ denote $[N \times 1]$ vectors containing the multi-mode and SE voltages and currents, and the matrices $\{\mathbf{K}^{\mathrm{v}}, \mathbf{K}^{\mathrm{i}}\}$ contain the respective coefficients of the SE voltages and currents that define each orthogonal mode, hence

$$\mathbf{K}^{\mathrm{v}} = \begin{bmatrix} k_{11}^{\mathrm{v}} & k_{12}^{\mathrm{v}} & \cdots & k_{1\mathrm{N}}^{\mathrm{v}} \\ \vdots & \vdots & \ddots & \vdots \\ k_{\mathrm{N1}}^{\mathrm{v}} & k_{\mathrm{N2}}^{\mathrm{v}} & \cdots & k_{\mathrm{NN}}^{\mathrm{v}} \end{bmatrix} \tag{3.19}$$

and

$$\mathbf{K}^{\mathrm{i}} = \begin{bmatrix} k_{11}^{\mathrm{i}} & k_{12}^{\mathrm{i}} & \cdots & k_{1\mathrm{N}}^{\mathrm{i}} \\ \vdots & \vdots & \ddots & \vdots \\ k_{\mathrm{N1}}^{\mathrm{i}} & k_{\mathrm{N2}}^{\mathrm{i}} & \cdots & k_{\mathrm{NN}}^{\mathrm{i}} \end{bmatrix}. \tag{3.20}$$

Using the fact that the total average power applied to the multi-mode antenna must remain equal for both SE and multi-mode representations, an expression can be derived to relate the voltage and current coefficient matrices to one another. With the SE and multi-mode average power defined as

$$\begin{aligned} P_{\mathrm{avg}}^{\mathrm{SE}} &= \frac{1}{2} \left(\left[\mathbf{V}^{\mathrm{SE}} \right]^T \left[\mathbf{I}^{\mathrm{SE}} \right]^* \right) \\ &= \frac{1}{2} \left(\left[\mathbf{V}^{\mathrm{MM}} \right]^T \left[\mathbf{I}^{\mathrm{MM}} \right]^* \right) = P_{\mathrm{avg}}^{\mathrm{MM}}, \end{aligned} \tag{3.21}$$

where, from (3.18a) and (3.18b)

$$\begin{aligned} P_{\mathrm{avg}}^{\mathrm{MM}} &= \frac{1}{2} \left(\left[\mathbf{K}^{\mathrm{v}} \mathbf{V}^{\mathrm{SE}} \right]^T \left[\mathbf{K}^{\mathrm{i}} \mathbf{I}^{\mathrm{SE}} \right]^* \right) \\ &= \frac{1}{2} \left(\left[\mathbf{V}^{\mathrm{SE}} \right]^T \left[\mathbf{K}^{\mathrm{v}} \right]^T \left[\mathbf{K}^{\mathrm{i}} \right]^* \left[\mathbf{I}^{\mathrm{SE}} \right]^* \right) \end{aligned} \tag{3.22}$$

it follows that, for the power relation in (3.21) to hold

$$\left[\mathbf{K}^{\mathrm{v}} \right]^T \left[\mathbf{K}^{\mathrm{i}} \right]^* = [\mathcal{I}] \tag{3.23}$$

or, for real valued coefficients, that

$$\left[\mathbf{K}^{\mathrm{v}} \right]^T = \left[\mathbf{K}^{\mathrm{i}} \right]^{-1} \tag{3.24}$$

with $[\mathcal{I}]$ denoting an $[N \times N]$ identity matrix.

Next, the incident and reflected waves of the multi-mode representation can be defined in terms of the SE voltages and currents. To this end, consider the expressions for the incident and reflected multi-mode waves, given by [44]

$$\mathbf{a}^{\mathrm{MM}} = \frac{1}{2}\left[\mathbf{Z}_{\mathrm{MM}}\right]^{-\frac{1}{2}}\mathbf{V}^{\mathrm{MM}} + \frac{1}{2}\left[\mathbf{Z}_{\mathrm{MM}}\right]^{\frac{1}{2}}\mathbf{I}^{\mathrm{MM}} \tag{3.25a}$$

$$\mathbf{b}^{\mathrm{MM}} = \frac{1}{2}\left[\mathbf{Z}_{\mathrm{MM}}\right]^{-\frac{1}{2}}\mathbf{V}^{\mathrm{MM}} - \frac{1}{2}\left[\mathbf{Z}_{\mathrm{MM}}\right]^{\frac{1}{2}}\mathbf{I}^{\mathrm{MM}} \tag{3.25b}$$

where $\mathbf{Z}_{\mathrm{MM}}$ is a diagonal matrix containing the characteristic impedances of each orthogonal port mode supported by the multiconductor transmission line

$$\mathbf{Z}_{\mathrm{MM}} = \begin{bmatrix} Z_1^{\mathrm{MM}} & \cdots & 0 \\ \vdots & \ddots & \vdots \\ 0 & \cdots & Z_{\mathrm{N}}^{\mathrm{MM}} \end{bmatrix}. \tag{3.26}$$

By substituting (3.18a) and (3.18b) into (3.25a) and (3.25b), the equivalent incident and reflected waves of each mode can be written in terms of the SE voltages and currents

$$\mathbf{a}^{\mathrm{MM}} = \frac{1}{2}\left[\mathbf{Z}_{\mathrm{MM}}\right]^{-\frac{1}{2}}\mathbf{K}^{\mathrm{v}}\mathbf{V}^{\mathrm{SE}} + \frac{1}{2}\left[\mathbf{Z}_{\mathrm{MM}}\right]^{\frac{1}{2}}\mathbf{K}^{\mathrm{i}}\mathbf{I}^{\mathrm{SE}} \tag{3.27a}$$

$$\mathbf{b}^{\mathrm{MM}} = \frac{1}{2}\left[\mathbf{Z}_{\mathrm{MM}}\right]^{-\frac{1}{2}}\mathbf{K}^{\mathrm{v}}\mathbf{V}^{\mathrm{SE}} - \frac{1}{2}\left[\mathbf{Z}_{\mathrm{MM}}\right]^{\frac{1}{2}}\mathbf{K}^{\mathrm{i}}\mathbf{I}^{\mathrm{SE}} \tag{3.27b}$$

and can further be related to the SE incident and reflected waves given that

$$\mathbf{V}^{\mathrm{SE}} = \left[\mathbf{Z}^{\mathrm{SE}}\right]^{\frac{1}{2}}\left(\mathbf{a}^{\mathrm{SE}} + \mathbf{b}^{\mathrm{SE}}\right) \tag{3.28a}$$

$$\mathbf{I}^{\mathrm{SE}} = \left[\mathbf{Z}^{\mathrm{SE}}\right]^{-\frac{1}{2}}\left(\mathbf{a}^{\mathrm{SE}} - \mathbf{b}^{\mathrm{SE}}\right) \tag{3.28b}$$

where $\{\mathbf{a}^{\mathrm{SE}}, \mathbf{b}^{\mathrm{SE}}\}$ denote $[N \times 1]$ vectors containing the SE incident and reflected waves, respectively, and $\mathbf{Z}^{\mathrm{SE}}$ is a diagonal matrix containing the SE characteristic port impedances

$$\mathbf{Z}_{\mathrm{SE}} = \begin{bmatrix} Z_{01} & \cdots & 0 \\ \vdots & \ddots & \vdots \\ 0 & \cdots & Z_{0\mathrm{N}} \end{bmatrix}. \tag{3.29}$$

Hence, the multi-mode incident and reflected waves can be expressed in terms of the SE waves by substituting (3.28a) and (3.28b) into (3.27a) and (3.27b). That is

$$\mathbf{a}^{\mathrm{MM}} = \frac{1}{2}\left[\mathbf{Z}_{\mathrm{MM}}\right]^{-\frac{1}{2}}\mathbf{K}^{\mathrm{v}}\left[\mathbf{Z}_{\mathrm{SE}}\right]^{\frac{1}{2}}\left(\mathbf{a}^{\mathrm{SE}} + \mathbf{b}^{\mathrm{SE}}\right) + \frac{1}{2}\left[\mathbf{Z}_{\mathrm{MM}}\right]^{\frac{1}{2}}\mathbf{K}^{\mathrm{i}}\left[\mathbf{Z}_{\mathrm{SE}}\right]^{-\frac{1}{2}}\left(\mathbf{a}^{\mathrm{SE}} - \mathbf{b}^{\mathrm{SE}}\right) \tag{3.30a}$$

$$\mathbf{b}^{\mathrm{MM}} = \frac{1}{2}\left[\mathbf{Z}_{\mathrm{MM}}\right]^{-\frac{1}{2}}\mathbf{K}^{\mathrm{v}}\left[\mathbf{Z}_{\mathrm{SE}}\right]^{\frac{1}{2}}\left(\mathbf{a}^{\mathrm{SE}} + \mathbf{b}^{\mathrm{SE}}\right) - \frac{1}{2}\left[\mathbf{Z}_{\mathrm{MM}}\right]^{\frac{1}{2}}\mathbf{K}^{\mathrm{i}}\left[\mathbf{Z}_{\mathrm{SE}}\right]^{-\frac{1}{2}}\left(\mathbf{a}^{\mathrm{SE}} - \mathbf{b}^{\mathrm{SE}}\right). \tag{3.30b}$$

The expressions in (3.30a) and (3.30b) can be condensed to

$$\mathbf{a}^{\mathrm{MM}} = \mathbf{K}_{\mathrm{aa}}\mathbf{a}^{\mathrm{SE}} + \mathbf{K}_{\mathrm{ab}}\mathbf{b}^{\mathrm{SE}} \tag{3.31a}$$

$$\mathbf{b}^{\mathrm{MM}} = \mathbf{K}_{\mathrm{ab}}\mathbf{a}^{\mathrm{SE}} + \mathbf{K}_{\mathrm{aa}}\mathbf{b}^{\mathrm{SE}} \tag{3.31b}$$

where

$$\mathbf{K}_{\mathrm{aa}} = \frac{1}{2}\left[\mathbf{Z}_{\mathrm{MM}}\right]^{-\frac{1}{2}}\mathbf{K}^{\mathrm{v}}\left[\mathbf{Z}_{\mathrm{SE}}\right]^{\frac{1}{2}} + \frac{1}{2}\left[\mathbf{Z}_{\mathrm{MM}}\right]^{\frac{1}{2}}\mathbf{K}^{\mathrm{i}}\left[\mathbf{Z}_{\mathrm{SE}}\right]^{-\frac{1}{2}} \tag{3.32a}$$

$$\mathbf{K}_{\mathrm{ab}} = \frac{1}{2}\left[\mathbf{Z}_{\mathrm{MM}}\right]^{-\frac{1}{2}}\mathbf{K}^{\mathrm{v}}\left[\mathbf{Z}_{\mathrm{SE}}\right]^{\frac{1}{2}} - \frac{1}{2}\left[\mathbf{Z}_{\mathrm{MM}}\right]^{\frac{1}{2}}\mathbf{K}^{\mathrm{i}}\left[\mathbf{Z}_{\mathrm{SE}}\right]^{-\frac{1}{2}}. \tag{3.32b}$$

The multi-mode S-matrix $\left(\mathbf{S}^{\mathrm{MM}}\right)$ can now be defined in terms of the SE S-matrix using the relationship

$$\mathbf{b}^{\mathrm{SE}} = \mathbf{S}^{\mathrm{SE}}\mathbf{a}^{\mathrm{SE}}. \tag{3.33}$$

The incident and reflected multi-mode waves then equate to

$$\mathbf{a}^{\mathrm{MM}} = \left[\mathbf{K}_{\mathrm{aa}} + \mathbf{K}_{\mathrm{ab}}\mathbf{S}^{\mathrm{SE}}\right]\mathbf{a}^{\mathrm{SE}} \tag{3.34a}$$

$$\mathbf{b}^{\mathrm{MM}} = \left[\mathbf{K}_{\mathrm{ab}} + \mathbf{K}_{\mathrm{aa}}\mathbf{S}^{\mathrm{SE}}\right]\mathbf{a}^{\mathrm{SE}} \tag{3.34b}$$

$$= \left[\mathbf{K}_{\mathrm{ab}} + \mathbf{K}_{\mathrm{aa}}\mathbf{S}^{\mathrm{SE}}\right]\left[\mathbf{K}_{\mathrm{aa}} + \mathbf{K}_{\mathrm{ab}}\mathbf{S}^{\mathrm{SE}}\right]^{-1}\mathbf{a}^{\mathrm{MM}} \tag{3.34c}$$

$$= \mathbf{S}^{\mathrm{MM}}\mathbf{a}^{\mathrm{MM}} \tag{3.34d}$$

where it follows from (3.34c) and (3.34d) that

$$\mathbf{S}^{\mathrm{MM}} = \left[\mathbf{K}_{\mathrm{ab}} + \mathbf{K}_{\mathrm{aa}}\mathbf{S}^{\mathrm{SE}}\right]\left[\mathbf{K}_{\mathrm{aa}} + \mathbf{K}_{\mathrm{ab}}\mathbf{S}^{\mathrm{SE}}\right]^{-1}. \tag{3.35}$$

The equivalent multi-mode S-matrix can therefore be solved using the voltage and current coefficient matrices $\{\mathbf{K}^{\mathrm{v}}, \mathbf{K}^{\mathrm{i}}\}$, the SE and multi-mode characteristic impedance matrices $\{\mathbf{Z}_{\mathrm{SE}}, \mathbf{Z}_{\mathrm{MM}}\}$, and the SE S-matrix of the antenna $\mathbf{S}^{\mathrm{SE}}$, using (3.35). It is worth noting that, for a symmetric multiconductor transmission line comprising isolated SE transmission lines, it can be shown, using (3.18a) and (3.18b), that the multi-mode characteristic impedance matrix is related to the SE characteristic impedance matrix by

$$\mathbf{Z}_{\mathrm{MM}} = \mathbf{K}^{\mathrm{v}}\,\mathbf{Z}_{\mathrm{SE}}\left[\mathbf{K}^{\mathrm{i}}\right]^{-1}. \tag{3.36}$$

With the SE to multi-mode transformation of the S-matrix derived, a corresponding expression by which the SE radiated electric field patterns can be transformed to the equivalent multi-mode radiation patterns can be defined, similar to the transformation defined for the dual-mode antenna in Sec. 3.1.2. Therefore, consider the SE electric field patterns, defined in a set of spherical coordinates, radiated by the multi-mode antenna when excited by wave excitations $\mathbf{a}^{\mathrm{SE}}$

$$\boldsymbol{f}_{\mathrm{n}}^{\mathrm{SE}}(\theta,\phi) = f_{\mathrm{n}}^{\mathrm{SE}\theta}(\theta,\phi)\,\hat{\boldsymbol{\alpha}}_{\boldsymbol{\theta}} + f_{\mathrm{n}}^{\mathrm{SE}\phi}(\theta,\phi)\,\hat{\boldsymbol{\alpha}}_{\boldsymbol{\phi}} \quad \text{for} \quad \mathrm{n} = 1, ..., N \tag{3.37}$$

where the superscripts SE_θ and SE_ϕ denote the theta and phi components of the SE radiated electric field, respectively. Once again, given the linearity between the radiated electric field and the excitation applied to the antenna port, the components of the radiated SE electric field can be transformed into the equivalent components of the multi-mode radiated electric field – corresponding to multi-mode incident waves $\left(\mathbf{a}^{\mathrm{MM}}\right)$ – using the expression in (3.34a). That is

$$\mathbf{F}^{\mathrm{p}}_{\mathrm{MM}} = \left[\mathbf{K}_{\mathrm{aa}} + \mathbf{K}_{\mathrm{ab}}\mathbf{S}^{\mathrm{SE}}\right] \mathbf{F}^{\mathrm{p}}_{\mathrm{SE}} \quad \text{for} \quad \mathrm{p} = \theta, \phi \tag{3.38}$$

where $\mathbf{F}^{\mathrm{p}}_{\mathrm{MM}} = [f_1^{\mathrm{MMp}}(\theta,\phi) \ \ldots \ f_{\mathrm{N}}^{\mathrm{MMp}}(\theta,\phi)]^T$ and $\mathbf{F}^{\mathrm{p}}_{\mathrm{SE}} = [f_1^{\mathrm{SEp}}(\theta,\phi) \ \ldots \ f_{\mathrm{N}}^{\mathrm{SEp}}(\theta,\phi)]^T$ denote $[N \times 1]$ vectors containing the p component of the multi-mode and SE radiated electric fields, respectively, with $p = \theta,\ \phi$.

To the author's knowledge, the transformation given in (3.35) is the first generalised expression relating the SE S-parameters of a multiconductor network to the equivalent S-parameters corresponding to an arbitrary combination of excitations defined according to the coefficient matrices $\mathbf{K}^{\mathrm{v}}$ and $\mathbf{K}^{\mathrm{i}}$. In the following section it is illustrated that (3.35) reduces to the same expression reported in [42, 43] for the case where $N = 2$.

3.2.2 Dual-mode antenna: Single-ended to mixed differential- and common-mode transformation

To demonstrate the implementation of the transformations derived in this section, the expressions are used to derive the transformation matrix of the dual-mode antenna introduced in Sec. 3.1.2, starting with the voltage and current coefficient matrices. Given the definitions of the differential- and common-mode voltages and currents in (3.2a) – (3.3b), the voltage and current coefficient matrices can be obtained by expressing the differential- and common-mode voltages and currents as linear combinations of the corresponding single-ended signals. That is,

$$\mathbf{V}^{\mathrm{MM}} = \begin{bmatrix} V_{\mathrm{DM}} \\ V_{\mathrm{CM}} \end{bmatrix} = \mathbf{K}^{\mathrm{v}}\mathbf{V}^{\mathrm{SE}} = \begin{bmatrix} 1 & -1 \\ \frac{1}{2} & \frac{1}{2} \end{bmatrix} \begin{bmatrix} V_1 \\ V_2 \end{bmatrix} \tag{3.39}$$

and

$$\mathbf{I}^{\mathrm{MM}} = \begin{bmatrix} I_{\mathrm{DM}} \\ I_{\mathrm{CM}} \end{bmatrix} = \mathbf{K}^{\mathrm{i}}\mathbf{I}^{\mathrm{SE}} = \begin{bmatrix} \frac{1}{2} & -\frac{1}{2} \\ 1 & 1 \end{bmatrix} \begin{bmatrix} I_1 \\ I_2 \end{bmatrix}. \tag{3.40}$$

Note that, for these definitions of $\mathbf{K}^{\mathrm{v}}$ and $\mathbf{K}^{\mathrm{i}}$, the relation given in (3.24) holds. Furthermore, since the transmission lines through which the dual-mode antenna is excited are symmetric and uncoupled, it follows from (3.6a) and (3.6b) that the SE and mixed differential- and common-mode characteristic impedance matrices equate to

$$\mathbf{Z}_{\mathrm{SE}} = Z_0 \begin{bmatrix} 1 & 0 \\ 0 & 1 \end{bmatrix} \tag{3.41}$$

and

$$\mathbf{Z}_{\mathrm{MM}} = Z_0 \begin{bmatrix} 2 & 0 \\ 0 & \frac{1}{2} \end{bmatrix} \tag{3.42}$$

with Z_0 denoting the SE characteristic impedance. For this set of matrices, the matrix $\mathbf{K}_{\mathrm{ab}}$ (3.32b) equates to a $[2 \times 2]$ zero matrix, and the matrix $\mathbf{K}_{\mathrm{aa}}$ (3.32a) equates to

$$\mathbf{K}_{\mathrm{aa}} = \frac{1}{\sqrt{2}} \begin{bmatrix} 1 & -1 \\ 1 & 1 \end{bmatrix} \tag{3.43}$$

which is the same as the transformation matrix $\mathbf{M}$, introduced in Sec. 3.1.2. With these values for $\mathbf{K}_{\mathrm{aa}}$ and $\mathbf{K}_{\mathrm{ab}}$, the transformations in (3.35) and (3.38) are seen to reduce to the same expressions shown in (3.13) and (3.16), respectively.

In Sec. 3.3 a quad-mode antenna, supporting four orthogonal TEM modes, is presented and the voltage and current coefficient matrices are derived to transform the SE response of the quad-mode antenna into the equivalent response of the orthogonal TEM excitation modes.

3.3 Quad-Mode Antenna

As discussed in Sec. 2.1.1 the aperture array antennas for the SKA telescope should be able to discern the polarisation state of an incident electromagnetic wave front for up to angles of 60° from zenith. Following from the dual-mode antenna design presented in Sec. 3.1.3, this section presents a dual-polarised quad-mode antenna which integrates two perpendicular dipole elements and a monopole into a single antenna element excited through a quadraxial transmission line [5].

3.3.1 Cylindrical quad-mode antenna design

Similar to the dual-mode antenna design presented in Sec. 3.1.3, the cylindrical quad-mode antenna is realised by connecting each arm of two perpendicularly oriented dipoles to one of the four inner conductors of a quadraxial transmission line, while the monopole element is realised by folding the ground shield of the quadraxial transmission line back towards the ground plane as shown in Fig. 3.14. Given the symmetrical design the cross-sectional cut of the quad-mode antenna, normal to either the x- or y-axis, is identical to that of the dual-mode antenna shown in Sec. 3.1.

Alternatively to four SE port modes, the quadraxial feed supports four orthogonal TEM port modes depicted in Figs. 3.15(a)–(d) and denoted by MM_1 – MM_4. When placed above an infinite ground plane, the four orthogonal TEM port modes result in the radiated far-field patterns illustrated in Figs. 3.15(e)–(h). It is seen that port modes MM_1 and MM_2 excite each of the dipole arms out-of-phase and create two orthogonal dipole-over-ground radiation patterns. A common-mode excitation is realised by exciting all four centre conductors in-phase

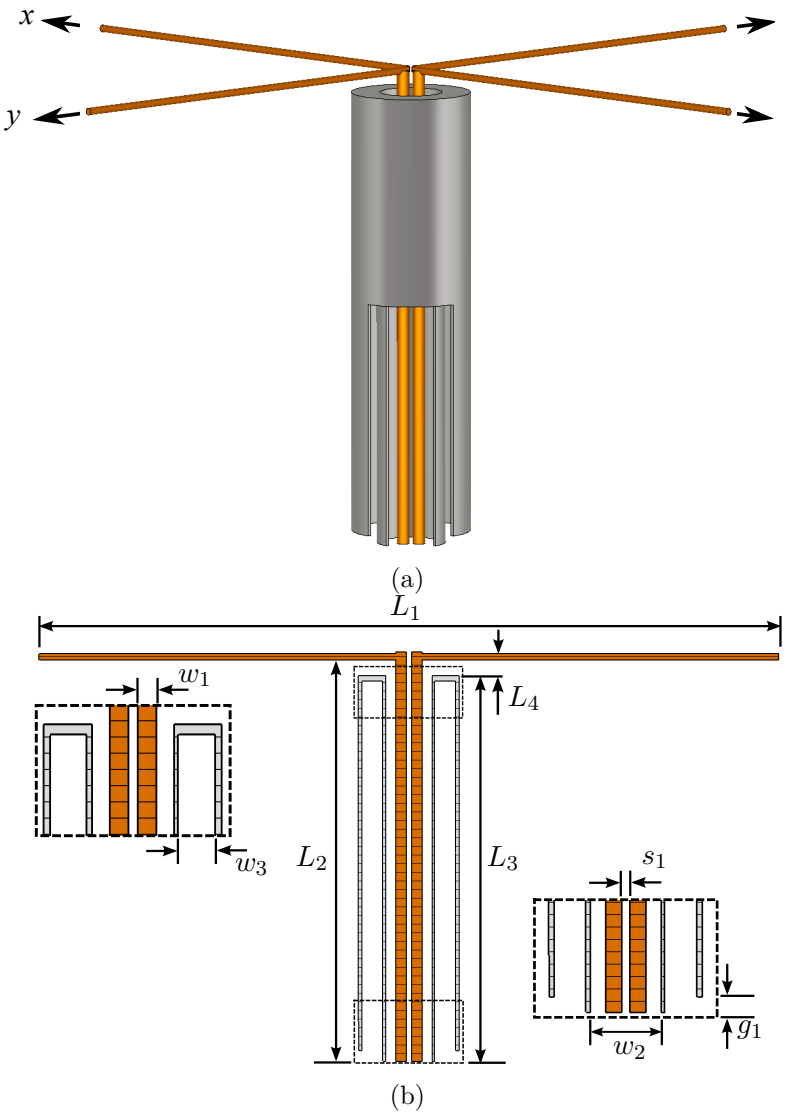

Figure 3.14: Quad-mode antenna design (a) showing inner quadraxial transmission line and cylindrical monopole sleeve (b) y-axis normal to cut-plane.

to give port mode MM_3 shown in Fig. 3.15(c). Due to the integrated monopole element, port mode MM_3 is seen to create a typical monopole far-field radiation pattern [c.f. 3.15(g)]. The fourth orthogonal port mode, MM_4, shown in Fig. 3.15(d) excites each orthogonal dipole arm out-of-phase, resulting in power radiated diagonally to the orientation of the dipole elements [c.f. 3.15(h)].

To illustrate the design procedure for the quad-mode antenna the parameters indicated in Fig. 3.14(b) are solved for a centre operating frequency of 1 GHz using CST Microwave Studio. Starting with the two perpendicular dipole elements, the length L_1 and height L_2 are set to approximately half and quarter wavelength at 1 GHz. Inserting the quadraxial transmission line into the design with the ground shield extending a height L_3 up to a small distance L_4 from the dipole arms, the four orthogonal port modes depicted in Figs. 3.15(a)–(d) are simulated in CST by defining the corresponding polarities on each of the inner conductors using a multi-pin port. First considering only port modes MM_1 and MM_2, the inner conductor width w_1, separation s_1,

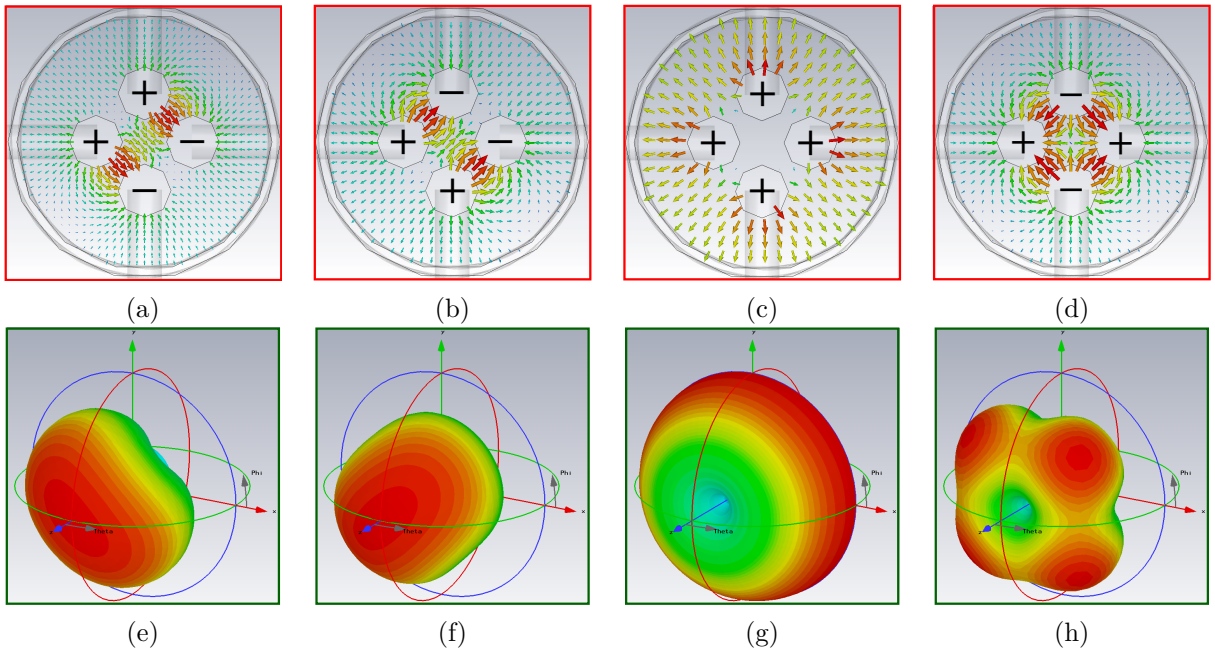

Figure 3.15: Simulated excitation field distributions for port modes (a) MM_1 (b) MM_2 (c) MM_3 (d) MM_4 and corresponding far-field radiation patterns for (e) MM_1 (f) MM_2 (g) MM_3 and (h) MM_4 excitation modes.

and the ground shield diameter w_2 are solved to realise a characteristic port impedance equal to the real part of the input impedance of the perpendicular dipole antennas when resonant at 1 GHz. Similar to the dual-mode antenna, the monopole sleeve is added by extending the ground shield radially outward a distance w_3 at the height L_3 and extending the shield back towards the ground plane, leaving a small gap g_1 between the shield and the ground plane. Since the monopole sleeve is excited through port mode MM_3, the ground shield diameter w_2 is solved such that the characteristic port impedance of mode MM_3 matches the real part of the input impedance of the same mode. Finally, adjusting the dimensions w_3 and L_4, the resonant frequency of mode MM_3 can be centred around 1 GHz.

The dimensions of the quad-mode antenna solved using CST Microwave Studio for a dipole arm diameter of 1.15 mm and a shield conductor thickness of 0.5 mm are indicated in Table 3.3.

Table 3.3: Design parameters of cylindrical quad-mode antenna depicted in Fig. 3.14(b).

Parameter	Value [mm]	Description
L_1	141	Dipole length
L_2	75	Dipole height
L_3	72	Feed/Monopole height
L_4	3	Dipole-Monopole separation
w_1	2	Feed inner conductor diameter
w_2	10	Feed ground shield inner diameter
w_3	2.75	Sleeve-Ground separation
g_1	2	Monopole-Ground plane gap height
s_1	1.5	Feed inner conductor separation

By comparing the input reflection coefficients of the four quadraxial port modes of the quad-mode antenna with the corresponding input reflection coefficients of a conventional dual-polarised crossed dipole antenna of similar dimensions, as shown in Fig. 3.16, the additional resonance introduced by the monopole sleeve can clearly be seen. Once again, the curves show the input reflection coefficients over the frequency range from 0.7 GHz to 1.4 GHz, with the markers on each curve indicating the input reflection coefficient of each mode at 1 GHz.

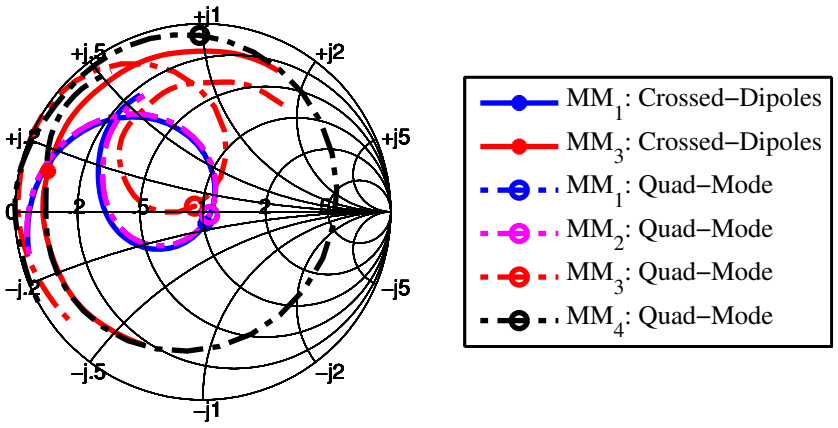

Figure 3.16: Input reflection coefficients of the quad-mode antenna compared with a conventional crossed dipole antenna.

As expected from the symmetric design, the input reflection coefficients of port modes MM_1 and MM_2 are seen to be identical over the entire frequency range. Analogous to the dual-mode antenna design presented in Sec. 3.1.3, the input reflection coefficients of port modes MM_1 and MM_2 are seen to remain virtually unchanged when introducing the monopole sleeve into the quad-mode antenna design. Considering the input reflection coefficient of mode MM_3 for the crossed dipoles it is seen that the mode remains mismatched over all frequencies. The introduction of the monopole sleeve with the quad-mode antenna design is seen to result in a resonance of mode MM_3 with the mode matched at 1 GHz. Also indicated in the graph is the input reflection coefficient of mode MM_4. It is noted that this mode remains mismatched over the frequency band, resulting in low radiated power from the MM_4 port mode.

The response of the quad-mode antenna can therefore be defined by a $[4 \times 4]$ S-matrix $\left(\mathbf{S}^{\mathrm{MM}}\right)$ – containing the input reflection coefficients of each orthogonal mode as well as the coupling between the modes – and four associated radiated electric field patterns $\left(\boldsymbol{f}_1^{\mathrm{MM}}(\theta,\phi) - \boldsymbol{f}_4^{\mathrm{MM}}(\theta,\phi)\right)$, depicted in Fig. 3.15(e)–(h). With the voltage and current coefficient matrices of the four orthogonal modes known, the response of the cylindrical quad-mode antenna for the four port modes can be transformed from the equivalent $[4 \times 4]$ SE S-matrix $\left(\mathbf{S}^{\mathrm{SE}}\right)$ and the radiated SE electric field patterns $\left(\boldsymbol{f}_1^{\mathrm{SE}}(\theta,\phi) - \boldsymbol{f}_4^{\mathrm{SE}}(\theta,\phi)\right)$ corresponding to wave excitations applied to each inner conductor, with the remaining three terminated in a matched load. To enable this, the voltage and current coefficient matrices of a quadraxial transmission line are derived in Sec. 3.3.2.

3.3.2 Single-ended to quad-mode transformation

To obtain the voltage and current coefficient matrices introduced in Sec. 3.2.1, expressions are presented to relate the voltage and current corresponding to each of the orthogonal modes depicted in Figs. 3.15(a)–(d) to the SE voltages and currents on the four inner conductors of the quadraxial transmission line. To this end, consider the schematic representations of the quadraxial transmission line, depicted in Figs. 3.17(a) and (b), showing the voltage and current applied to the constituent inner conductors for mode MM_1 [c.f. Fig. 3.15(a)].

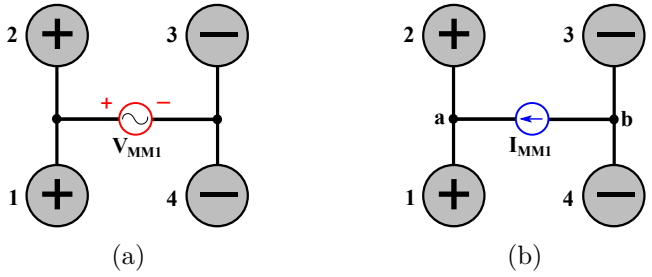

Figure 3.17: Transverse view of the four inner conductors of a quadraxial transmission line showing the (a) voltage and (b) current of mode MM_1.

The voltage and current on the four inner conductors can be defined in terms of four SE open circuited voltages and short circuited currents with respect to the common ground conductor as illustrated in Figs. 3.18(a) and (b).

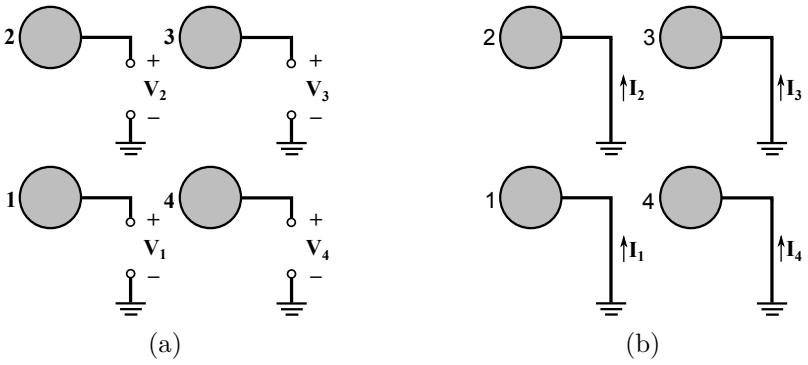

Figure 3.18: Transverse view of the four inner conductors of a quadraxial transmission line showing the (a) SE open circuited voltages and (b) SE short circuited currents on each conductor.

To define the voltage corresponding to mode MM_1 as a linear combination of the SE voltages shown in Fig. 3.18(a), the voltage V_{MM1} is first defined with respect to the common ground conductor, resulting in the equivalent circuit in Fig. 3.19.

Comparing the ground referenced voltage of mode MM_1 in Fig. 3.19 to the SE voltages defined

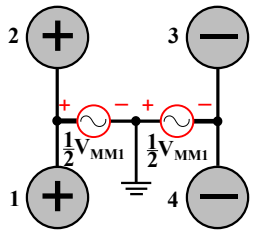

Figure 3.19: Transverse view of the four inner conductors of a quadraxial transmission line showing the ground referenced voltage of mode MM_1.

in Fig. 3.18(a) it follows that

$$V_1 = V_2 = \frac{V_{MM1}}{2} \tag{3.44a}$$

$$V_3 = V_4 = -\frac{V_{MM1}}{2}. \tag{3.44b}$$

The voltage of mode MM_1 can therefore be expressed as the linear combination

$$V_{MM1} = \frac{1}{2}\left(V_1 + V_2 - V_3 - V_4\right). \tag{3.45}$$

Next, consider the current induced by mode MM_1, shown in Fig. 3.17(b). By summing the currents at nodes **a** and **b**, the current I_{MM1} can be defined as a linear combination of the SE currents depicted Fig. 3.18(b). That is, at node **a** and **b**

$$I_1 + I_2 = I_{MM1} \tag{3.46a}$$

$$I_3 + I_4 = -I_{MM1} \tag{3.46b}$$

from which it follows that

$$I_{MM1} = \frac{1}{2}\left(I_1 + I_2 - I_3 - I_4\right). \tag{3.47}$$

Given the similarity between the polarities defined on the inner conductors of the quadraxial transmission line for modes MM_1, MM_2, and MM_4 [c.f. Figs. 3.15(a), (b) and (d)], equivalent circuits, similar to Figs. 3.17(a), (b), and Fig. 3.19, can be defined for the voltages and currents of modes MM_2 and MM_4. The same procedure used to obtain (3.45) and (3.47) can then be applied to derive expressions for the voltages and currents of modes MM_2 and MM_4 as linear combinations of the SE voltages and currents, where

$$V_{MM2} = \frac{1}{2}\left(V_1 - V_2 - V_3 + V_4\right) \tag{3.48a}$$

$$V_{MM4} = \frac{1}{2}\left(V_1 - V_2 + V_3 - V_4\right), \tag{3.48b}$$

and

$$I_{\text{MM2}} = \frac{1}{2}\left(I_1 - I_2 - I_3 + I_4\right) \tag{3.49a}$$

$$I_{\text{MM4}} = \frac{1}{2}\left(I_1 - I_2 + I_3 - I_4\right). \tag{3.49b}$$

Lastly, consider the remaining mode, MM_3. As shown in Fig. 3.15(c), the four inner conductors are simulated in-phase, therefore the equivalent ground referenced voltage and current associated with the MM_3 mode can be depicted as in Figs. 3.20(a) and (b).

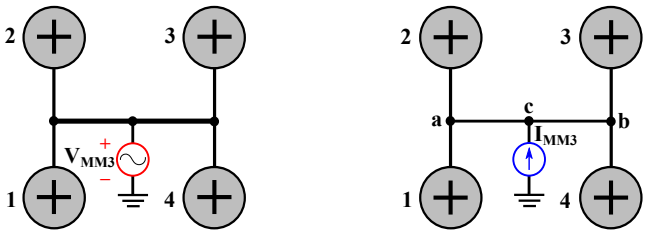

Figure 3.20: Transverse view of the four inner conductors of a quadraxial transmission line showing the ground referenced (a) voltage and (b) current of mode MM_3.

Comparing Figs. 3.20(a) and (b) to Figs. 3.18(a) and (b), it is seen that for mode MM_3

$$V_1 = V_2 = V_3 = V_4 \tag{3.50}$$

$$= V_{\text{MM3}} \tag{3.51}$$

or

$$V_{\text{MM3}} = \frac{1}{4}\left(V_1 + V_2 + V_3 + V_4\right) \tag{3.52}$$

and through summing the currents at node **c** in Fig. 3.20(b) that

$$I_{\text{MM3}} = I_1 + I_2 + I_3 + I_4. \tag{3.53}$$

With the voltages and currents of the four orthogonal modes shown in Figs. 3.15(a)–(d) defined as linear combinations of the equivalent SE voltages and currents, it follows from (3.45), (3.48a), (3.52), and (3.48b) that the voltage coefficient matrix (3.19) for the quadraxial transmission line is of the form

$$\mathbf{K}^{\text{v}} = \begin{bmatrix} \frac{1}{2} & \frac{1}{2} & -\frac{1}{2} & -\frac{1}{2} \\ \frac{1}{2} & -\frac{1}{2} & -\frac{1}{2} & \frac{1}{2} \\ \frac{1}{4} & \frac{1}{4} & \frac{1}{4} & \frac{1}{4} \\ \frac{1}{2} & -\frac{1}{2} & \frac{1}{2} & -\frac{1}{2} \end{bmatrix} \tag{3.54}$$

and from (3.47), (3.49a), (3.53), and (3.49b) that the current coefficient matrix (3.20) equates

to

$$\mathbf{K}^{\mathrm{i}} = \begin{bmatrix} \frac{1}{2} & \frac{1}{2} & -\frac{1}{2} & -\frac{1}{2} \\ \frac{1}{2} & -\frac{1}{2} & -\frac{1}{2} & \frac{1}{2} \\ 1 & 1 & 1 & 1 \\ \frac{1}{2} & -\frac{1}{2} & \frac{1}{2} & -\frac{1}{2} \end{bmatrix}, \tag{3.55}$$

both conforming to relation given in (3.24).

3.3.3 Quad-mode antenna S-matrix transformation

To illustrate the validity of the voltage (3.54) and current (3.55) coefficient matrices derived in Sec. 3.3.2, the matrices are used to transform the SE S-matrix of the cylindrical quad-mode antenna to the S-matrix corresponding to the four modes shown in Figs. 3.15(a)–(d). In the analysis to follow, both the SE and multi-mode results are obtained by simulating the quad-mode antenna with the corresponding excitations over an infinite ground plane in CST Microwave Studio. The SE S-matrix of the quad-mode antenna is simulated using a multi-pin port with the Single-Ended function enabled, resulting in the four SE port excitations shown in Fig. 3.21, and the corresponding SE S-parameters depicted in the graph in Fig. 3.22. Due to

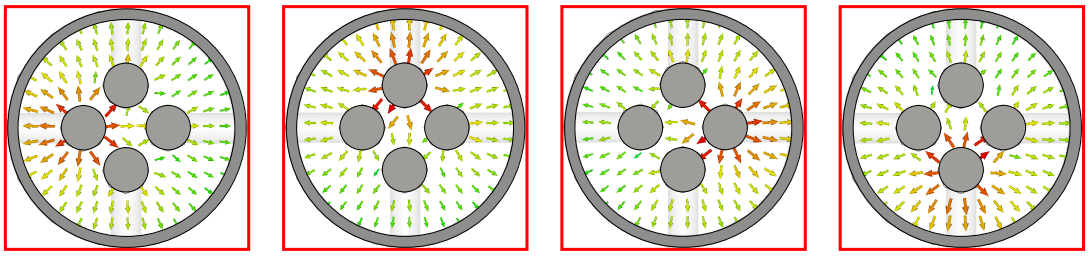

(a) (b) (c) (d)

Figure 3.21: Simulated single-ended excitation field distributions (a) SE_1, (b) SE_2, (c) SE_3, and (d) SE_4 of the quad-mode antenna.

symmetry, the input reflection coefficients and coupling between two adjacent inner conductors and the inner conductors across from one another are respectively equal. Therefore only three curves are shown in Fig. 3.22. Note that the SE modes are not well matched at 1 GHz.

Given the transformation in (3.35), the SE response of the quad-mode antenna can be transformed into the S-matrix corresponding to the four orthogonal excitation modes shown in Figs. 3.15(a)–(d), using the voltage and current coefficient matrices $\{\mathbf{K}^{\mathrm{v}}, \mathbf{K}^{\mathrm{i}}\}$ as in (3.54) and (3.55), the SE S-matrix of the quad-mode antenna $\mathbf{S}^{\mathrm{SE}}$, as well as the impedance matrices containing the SE and multi-mode characteristic impedance of each port or mode $\{\mathbf{Z}_{\mathrm{SE}}, \mathbf{Z}_{\mathrm{MM}}\}$ simulated in CST. For the dimensions of the quadraxial transmission line of the quad-mode antenna, shown in Fig. 3.14, the following SE and multi-mode characteristic impedance matrices

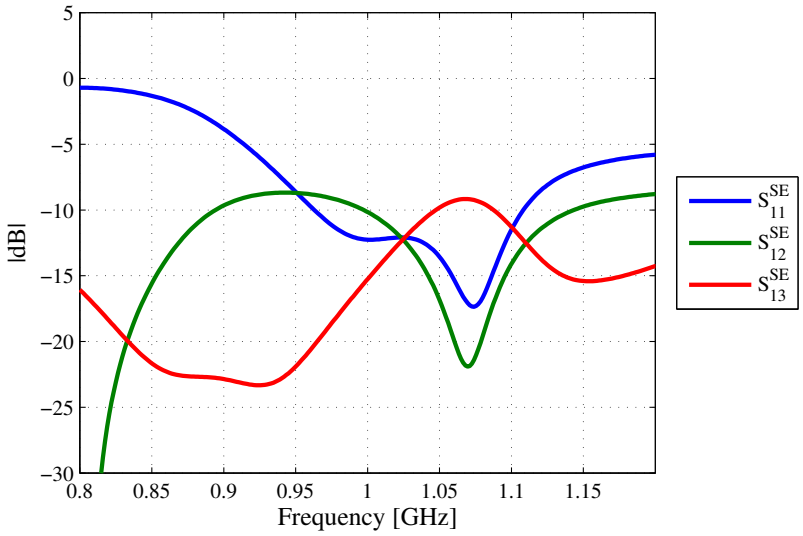

Figure 3.22: Single-ended S-parameters of the cylindrical quad-mode antenna simulated in CST.

result,

$$\mathbf{Z}_{\text{SE}} = \begin{bmatrix} 70 & 0 & 0 & 0 \\ 0 & 70 & 0 & 0 \\ 0 & 0 & 70 & 0 \\ 0 & 0 & 0 & 70 \end{bmatrix} \tag{3.56a}$$

$$\mathbf{Z}_{\text{MM}} = \begin{bmatrix} 44 & 0 & 0 & 0 \\ 0 & 44 & 0 & 0 \\ 0 & 0 & 43 & 0 \\ 0 & 0 & 0 & 25 \end{bmatrix} \tag{3.56b}$$

where the characteristic impedances of the four SE excitations are seen to be equal for the symmetric quadraxial transmission line. It is worth noting that, given the fact that the inner conductors of the quadraxial feed are not isolated at the port plane, the SE and multi-mode characteristic impedance matrices are not related through the expression in (3.36).

The graph in Fig. 3.23 compares the input reflection coefficients of the four orthogonal port modes transformed from the simulated SE S-matrix using (3.35) to the results obtained for the orthogonal quad-mode excitations using CST. Since the four modes are orthogonal, the simulated isolation between the modes are below -50 dB across the frequency band, and is therefore omitted from the graph. The curves clearly show that the voltage and current coefficient matrices derived in this section and (3.35) derived in Sec. 3.2.1 give an exact transformation of the SE S-parameters.

It follows that the same transformation process can be used to calculate the multi-mode radiation patterns from the SE radiation patterns of the quad-mode antenna, allowing for full characterisation using SE measurements. This is shown in the following section, where an improved

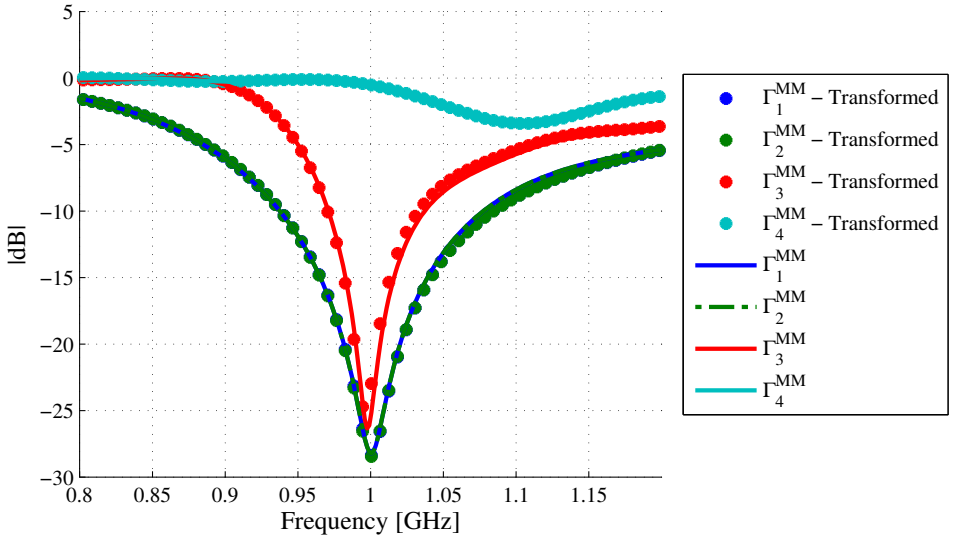

Figure 3.23: Comparison of the simulated and transformed input reflection coefficients of the cylindrical quad-mode antenna for the four orthogonal port modes.

quad-mode antenna is presented, featuring a more robust construction and much improved bandwidth.

3.4 Quad-Mode Antenna with Improved Operating Bandwidth

While the quad-mode antenna of Sec. 3.3 illustrates the principle of such an antenna, it has a relatively narrow operating bandwidth. This section presents a conical quad-mode antenna design operating over an improved frequency bandwidth. The design considerations of the antenna is presented in Sec. 3.4.1 and the measured performance of a conical quad-mode antenna design obtained through the transformations derived in Sec. 3.3.2 is given in Sec. 3.4.2.

3.4.1 Conical quad-mode antenna design

Similar to the cylindrical design, the conical quad-mode antenna design presented here is excited with a quadraxial transmission line supporting the four orthogonal excitation modes depicted in Figs. 3.15(a) to (d). The conical quad-mode antenna design analysed in this section is based on the same operating principle of the cylindrical design introduced in Sec. 3.3.1, where the operating frequency bandwidth of the constituent orthogonal dipole elements are improved through the implementation of two perpendicularly oriented bow-tie dipole elements, and the improved bandwidth of the monopole is achieved by integrating a conical monopole element into the design based on the principles of the wideband Discone antenna [12]. Conventionally the discone antenna is realised by terminating the centre conductor of a coaxial transmission line in the centre of a planar disc positioned perpendicular to the coaxial line. As illustrated

in Fig. 3.24 a conical section is placed a small distance under the planar disc with the apex connected to the ground shield of the coaxial transmission line.

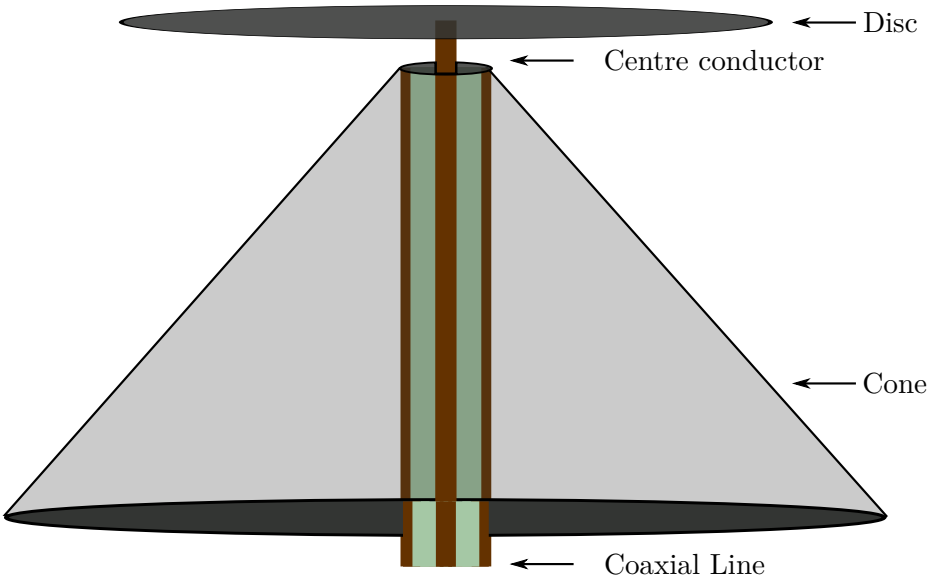

Figure 3.24: Graphic illustration of a discone antenna.

Given that excitation MM_3 [c.f. Fig. 3.15(c)] excites the four inner conductors of the quadraxial transmission line in-phase, the coaxial transmission line exciting the discone antenna can be replaced with a quadraxial transmission line excited by mode MM_3 without changing the radiation characteristics of the discone antenna. As expected the planar disc connected to the four inner conductors acts as a short for the remaining three port modes depicted in Fig. 3.15(a), (b), and (d). Hence, to allow for excitation through additional port modes, the conical quad-mode antenna approximates the planar disc using two perpendicularly oriented bow-tie dipoles with wide flare angels. To illustrate the design procedure of a conical quad-mode antenna, consider the following design performed over an infinite ground plane in CST Microwave Studio for a centre frequency near 1 GHz.

Starting with port mode MM_3, the dimensions of the conical monopole sleeve are solved using the design shown in Fig. 3.25. Initially the four inner conductors of the quadraxial feed are terminated in a solid planar disc positioned a quarter wavelength at the centre frequency (h_3) above the ground plane with diameter (l_3) equal to approximately half a wavelength at the same frequency. As indicated in Fig. 3.25 the planar disc is printed on a FR-4 substrate with a thickness t_4 and the apex of the conical section is connected to the ground shield of the quadraxial feed at a height h_2 a small distance below the substrate. Similar to the cylindrical quad-mode design, the conical monopole sleeve extends towards the ground plane up to a height h_1 from the ground plane. Considering only excitation mode MM_3, the bottom and top diameters of the cone (l_1 and l_2), as well as the dimensions h_1 and h_2 are solved to match mode MM_3 at the desired centre frequency. The Smith chart in Fig. 3.26 shows the input reflection coefficient of

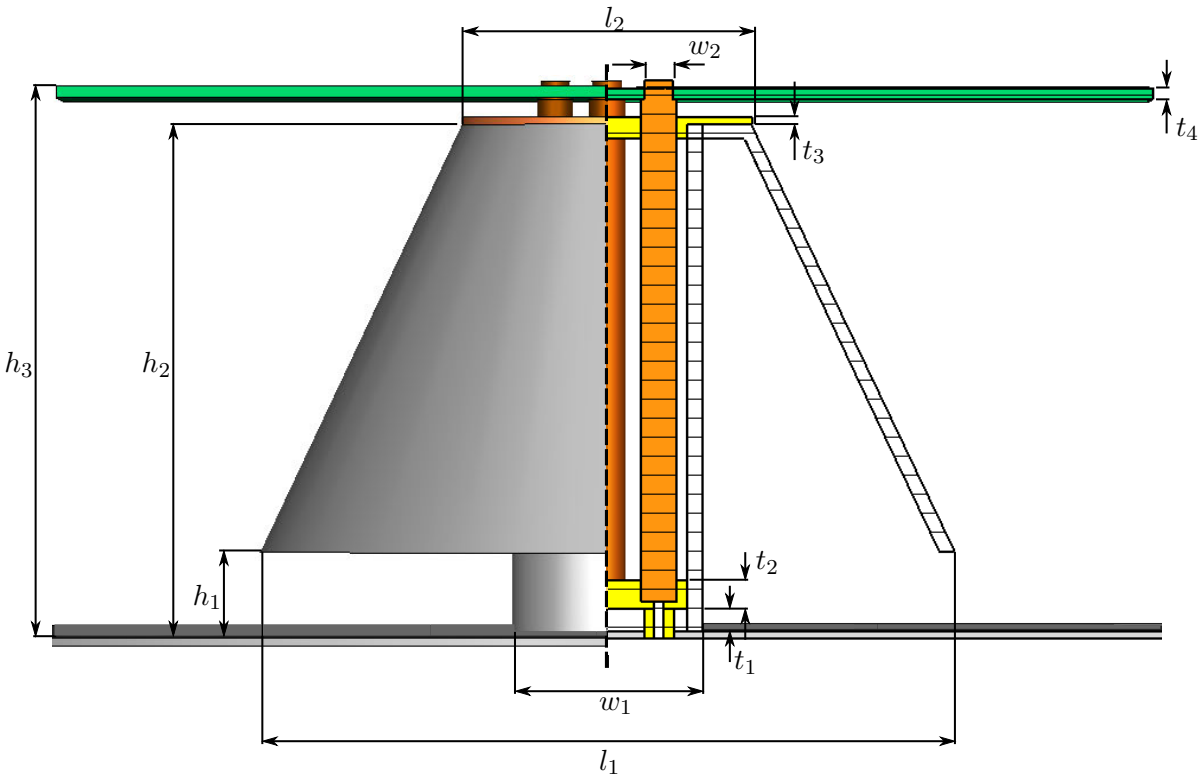

Figure 3.25: Side view of conical quad-mode antenna design showing the quadraxial feed.

modes MM_1 and MM_3 over the frequency band ranging from 0.8 GHz to 1.2 GHz for the conical quad-mode antenna with a solid disc and cone dimensions listed in Table 3.4.

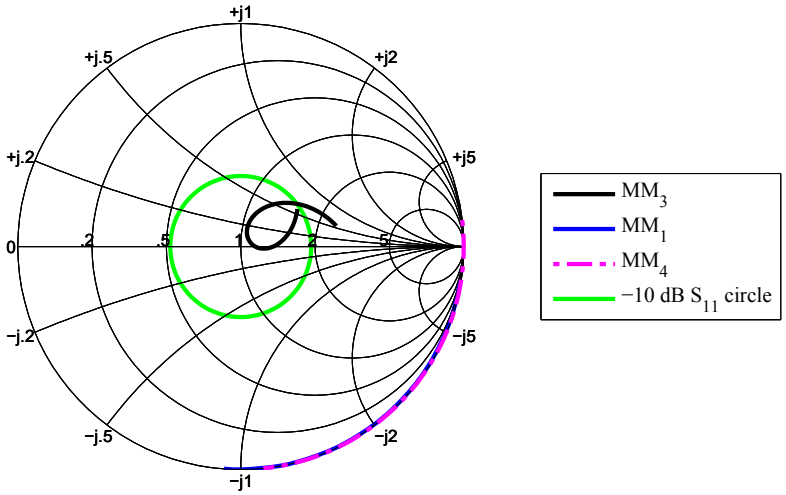

Figure 3.26: Input reflection coefficients of port modes MM_1 and MM_3 of the conical quad-mode antenna with a solid disc.

Also indicated on the Smith chart in Fig. 3.26 is the 10 dB return loss circle. As shown, a reflection coefficient below -10 dB is achieved for mode MM_3 from 0.8 GHz up to 1.1 GHz, where mode MM_1 is seen to be completely mismatched due to the solid disc. Given the similarity between the potentials defined on the inner conductors for modes MM_1, MM_2, and MM_4 all three

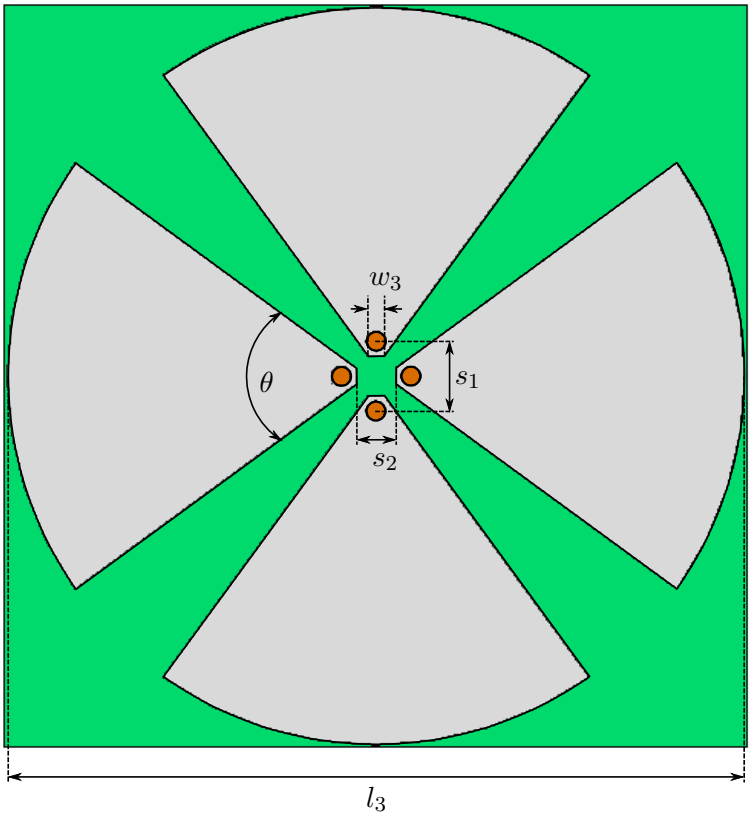

Figure 3.27: Top view of the conical quad-mode antenna design showing the two integrated bow-tie dipole elements.

modes display the same mismatch across the frequency band. In order to improve the match of the additional modes, the planar disc is replaced by two perpendicular bow-tie elements shown in Fig. 3.27.

The arm of each bow-tie has a flare angle θ and the length of each bow-tie element is kept the same as the diameter of the solid disc (l_3) used during the previous step. Analogous to the cylindrical quad-mode antenna the two bow-tie elements allow for two orthogonal dipole-over-ground radiation patterns through excitation modes MM_1 and MM_2. By altering the flare angle of each dipole arm, these two additional modes can be matched over the same frequency band as mode MM_3. The Smith chart in Fig. 3.28 shows the input reflection coefficient of mode MM_1 from 0.8 GHz up to 1.2 GHz when varying the flare angle θ from 89° down to 72°. Once again a 10 dB return loss circle is included for reference.

From the curves shown in Fig. 3.28 a clear improvement in the matching of port mode MM_1 is seen across the band, with an optimum match achieved for a flare angle of 72°. Since modes MM_1 and MM_2 excite both dipoles in a similar fashion, the input reflection coefficients of both modes are equal across the band, therefore only mode MM_1 is shown. Also shown in the graph is the input reflection coefficient of mode MM_3 for an arm flare angle of 72° as well as the input reflection coefficient solved for a solid disc. It is clearly noted that the bow-tie dipole elements result in only a small variation in the match of mode MM_3. Lastly, the input reflection coefficient of mode MM_4 is also included in the graph. Similar to the cylindrical quad-mode antenna design,

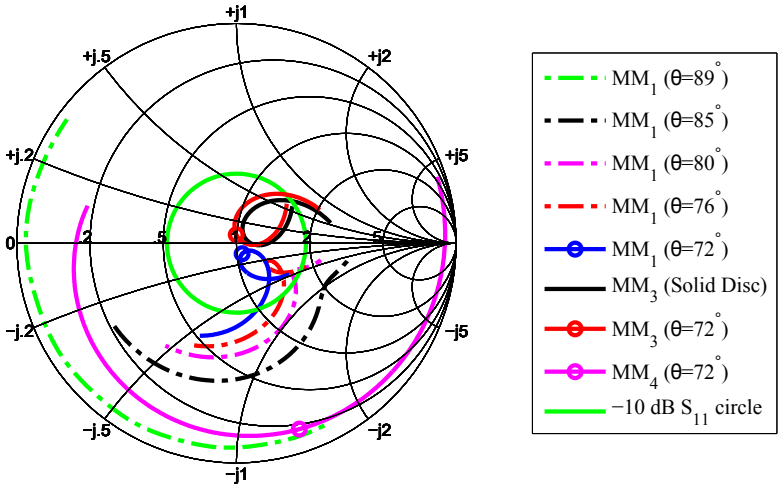

Figure 3.28: Input reflection coefficients of port modes MM_1 and MM_3 of the conical quad-mode antenna with integrated bow-tie dipole elements.

this mode is still mismatched within the frequency band from 0.8 GHz to 1.1 GHz. In Chapter 4 the effect this mismatched mode has on the gain, sensitivity, and polarimetric performance of the conical quad-mode antenna is investigated and beamforming algorithms are proposed by which complex weights can be allocated to each of the four port modes to mitigate the effects resulting from this mismatch.

As shown in Fig. 3.25, the conical quad-mode antenna is excited through an air-core quadraxial transmission line comprising a 2 mm thick aluminium ground shield, and four brass centre conductors each with a diameter of 5 mm. The bottom of the quadraxial line is shorted with a cylindrical block of aluminium with thickness (t_1) through which the centre conductor of four SMA connectors are connected to the inner conductors of the quadraxial transmission line. To keep the inner conductors in place, two Teflon spacers are implemented, one at the bottom with thickness (t_2), and the other positioned at the top of the feed extending a thickness (t_3) above the conical monopole and a further 2 mm into the quadraxial feed. Each of the inner conductors is connected to one of the constituent arms of the perpendicular bow-tie dipole elements as shown in Fig. 3.27. The design dimensions depicted in Figs. 3.25 and 3.27 are summarised in Table 3.4.

The graph in Fig. 3.29 shows the input reflection coefficients of the conical quad-mode antenna, simulated over an infinite ground plane in CST Microwave Studio, for four orthogonal excitation modes with field distributions corresponding to the modes illustrated in Figs. 3.15(a)–(d). As seen from the graph, modes MM_1 – MM_3 are matched to below -10 dB within the frequency band ranging from 0.8 GHz to 1.1 GHz – an improvement of a factor three compared with the cylindrical quad-mode antenna of Sec. 3.3.1 – with mode MM_4 largely mismatched within the frequency band.

Figures 3.30(a)–(d) and Figs. 3.30(e)–(h) show the simulated far-field radiation pattern of each mode at 0.8 GHz and 1.1 GHz, respectively.

Table 3.4: Conical quad-mode antenna design parameters

Parameter	Value [mm]	Description
w_1	26.15	Ground shield outer diameter
w_2	4	Reduced inner conductor diameter
w_3	3.3	Bow-tie inner edge width
t_1	3	Aluminium feed short thickness
t_2	4	Bottom Teflon spacer thickness
t_3	1	Top Teflon spacer thickness
t_4	1.6	FR-4 substrate thickness
l_1	96	Conical monopole bottom length
l_2	40	Conical monopole top length
l_3	150	Bow-tie dipole length
h_1	11	Conical monopole - ground plane separation
h_2	70	Quadraxial feed height
h_3	75	Dipole height
s_1	14.15	SMA feed centre separation
s_2	8	Bow-tie arm inner edge separation
θ	72	Bow-tie arm flare angle

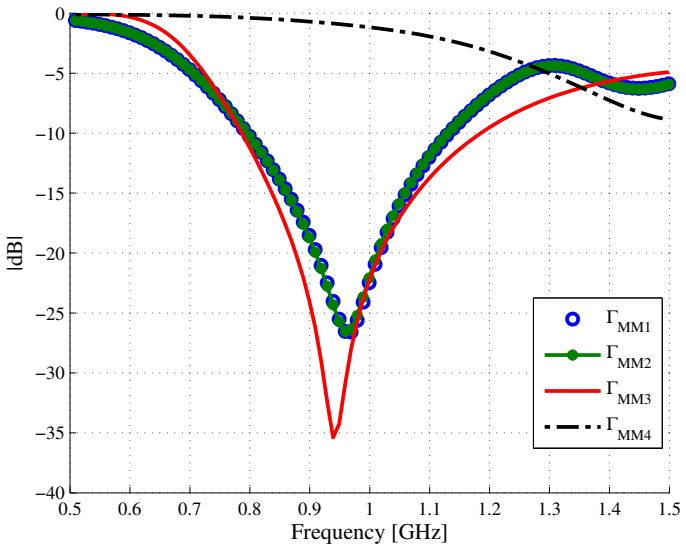

Figure 3.29: Simulated input reflection coefficients of the four orthogonal excitation modes for the conical quad-mode antenna above an infinite ground plane.

Similar to the cylindrical quad-mode antenna design, two typical dipole-over-ground radiation patterns are seen to result for excitation modes MM_1 and MM_2, with a slight deformation of the radiated far-fields observed at the higher end of the band. Excitation mode MM_3 results in a typical monopole radiation pattern throughout the frequency band, and the fourth mode, MM_4, is seen to radiate in a similar fashion as observed for the cylindrical quad-mode antenna design. The graphs in Fig. 3.31 show the realised gain in the $\phi = 0°$ plane for each excitation mode simulated at 100 MHz intervals over the frequency range from 0.8 GHz to 1.1 GHz.

As expected, the realised gain of modes MM_1 and MM_2 are seen to be identical at all frequencies,

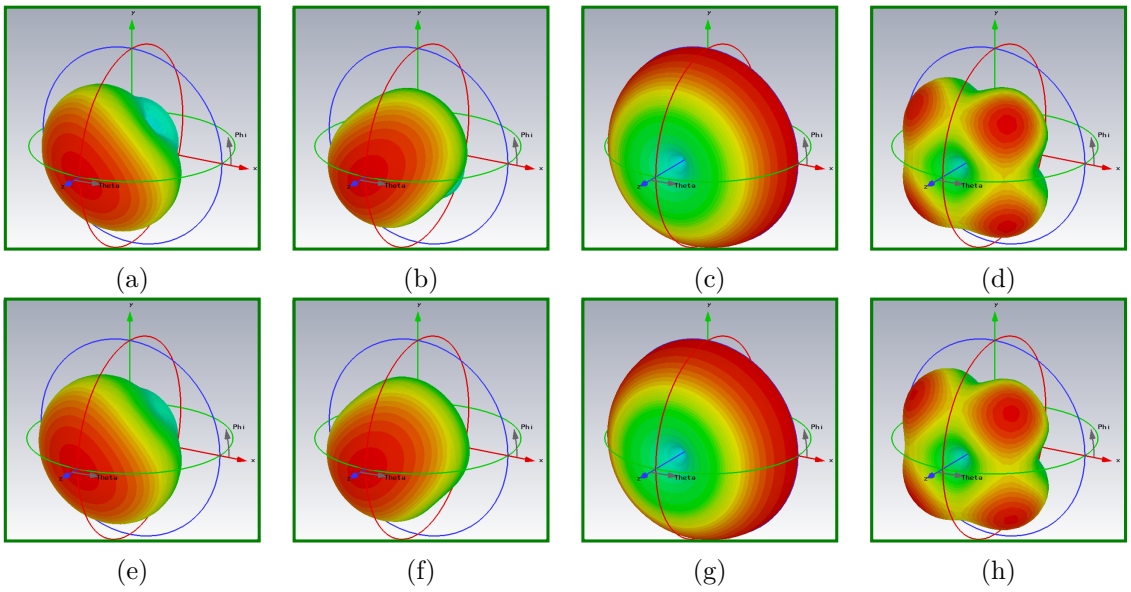

Figure 3.30: Simulated far-fields of the conical quad-mode antenna radiated at 0.8 GHz by modes (a) MM_1 (b) MM_2 (c) MM_3 (d) MM_4 and 1.1 GHz by modes (e) MM_1 (f) MM_2 (g) MM_3 and (h) MM_4.

radiating in a typical dipole-over-ground fashion with a peak gain values above 7.5 dB at zenith. The realised gain for excitation mode MM_3 is seen to resemble that of a monopole, with a maximum gain of approximately 5 dB toward $\theta = 90°$ across the frequency band. Regardless of the fact that the power radiated by mode MM_4 is a maximum along the diagonal planes, the mismatch of mode MM_4 [c.f. Fig. 3.29] is seen to result in much lower realised gain values in the $\phi = 0°$ plane and noted to increase with frequency. This increase in the realised gain of mode MM_4 corresponds to the decrease in input reflection coefficient observed at higher frequencies. Considering the realised gain of the conical quad-mode antenna at 1.2 GHz and 1.3 GHz shown in Fig. 3.32, deformation of the radiation patterns of modes MM_1 and MM_2 is noted with the dipole-over-ground radiation characteristic disappearing completely at 1.3 GHz. Excitation mode MM_3 is still seen to radiate in a typical monopole fashion but with lower gain due to the increased mismatch at these frequencies.

In the following section, Sec. 3.4.2, the performance of the conical quad-mode antenna is verified through SE measurements and implementing the S-matrix and far-field transformations given in (3.35) and (3.38), respectively.

3.4.2 Conical quad-mode antenna: Measured response

To allow for feasible measurement of the conical quad-mode antenna, introduced in Sec. 3.4.1, the antenna is placed in the centre of a circular ground plane with a diameter of 450 mm. The manufactured conical quad-mode antenna, together with the four SE SMA connectors by which each of the inner conductors of the quadraxial transmission line is excited, are depicted in Fig. 3.33.

Using a four-port vector network analyser, the full four-port SE S-matrix of the antenna $\left(\mathbf{S}^{\mathrm{SE}}\right)$

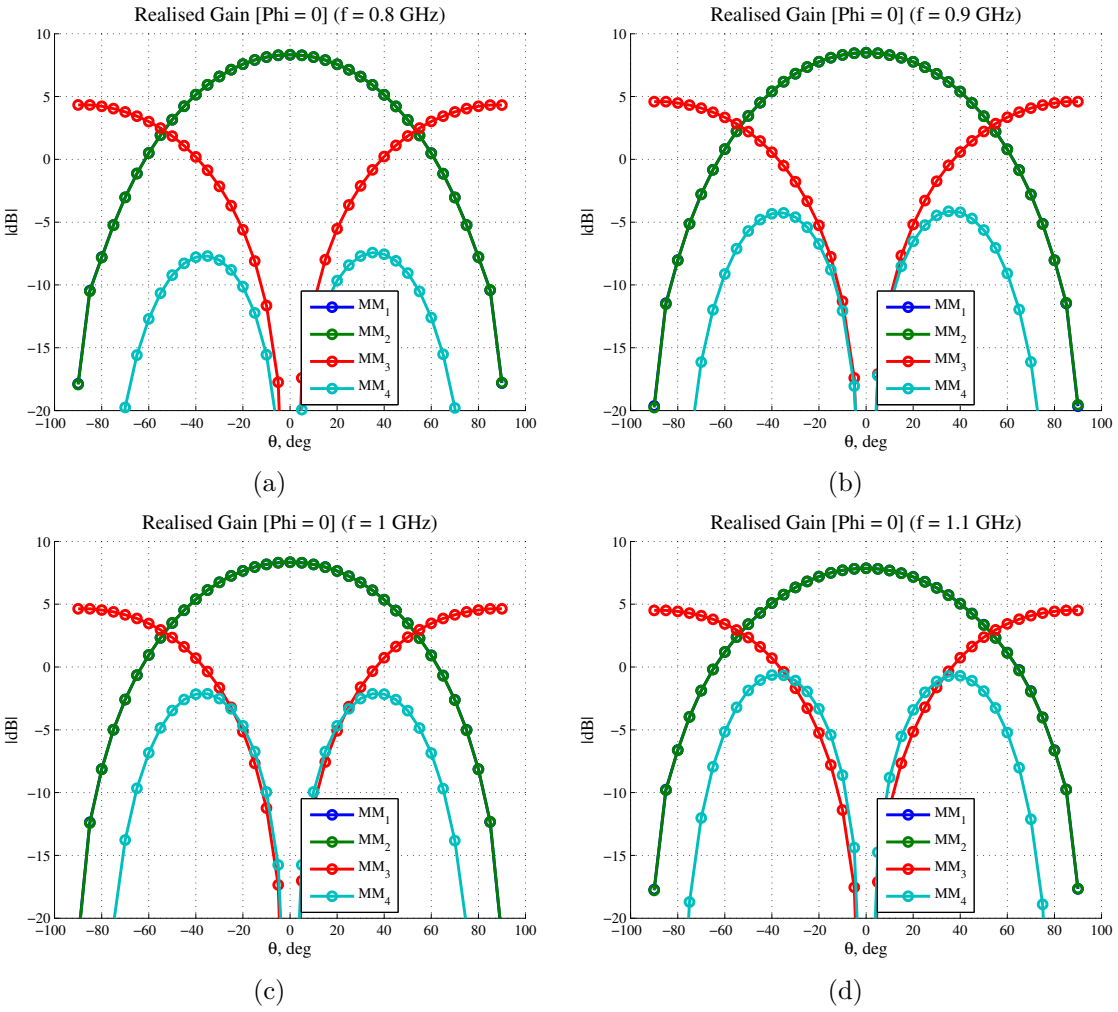

Figure 3.31: Simulated realised gain of the conical quad-mode antenna over an infinite ground plane for the four orthogonal TEM excitation modes at (a) 0.8 GHz, (b) 0.9 GHz, (c) 1 GHz, and (d) 1.1 GHz in the $\phi = 0$ plane.

can be obtained. Through (3.35), the input reflection coefficients for the four orthogonal modes can then be solved from the measured SE S-matrix, the voltage and current coefficient matrices as defined in (3.54) and (3.55), and the characteristic impedance matrices $\{\mathbf{Z}_{\text{MM}}, \mathbf{Z}_{\text{SE}}\}$ where, for the four SE SMA connectors,

$$\mathbf{Z}_{\text{SE}} = \begin{bmatrix} 50 & 0 & 0 & 0 \\ 0 & 50 & 0 & 0 \\ 0 & 0 & 50 & 0 \\ 0 & 0 & 0 & 50 \end{bmatrix} \tag{3.57}$$

and, given that the SE ports are isolated at the port plane, it follows from (3.36) that,

$$\mathbf{Z}_{\text{MM}} = \begin{bmatrix} 50 & 0 & 0 & 0 \\ 0 & 50 & 0 & 0 \\ 0 & 0 & 12.5 & 0 \\ 0 & 0 & 0 & 50 \end{bmatrix}. \tag{3.58}$$

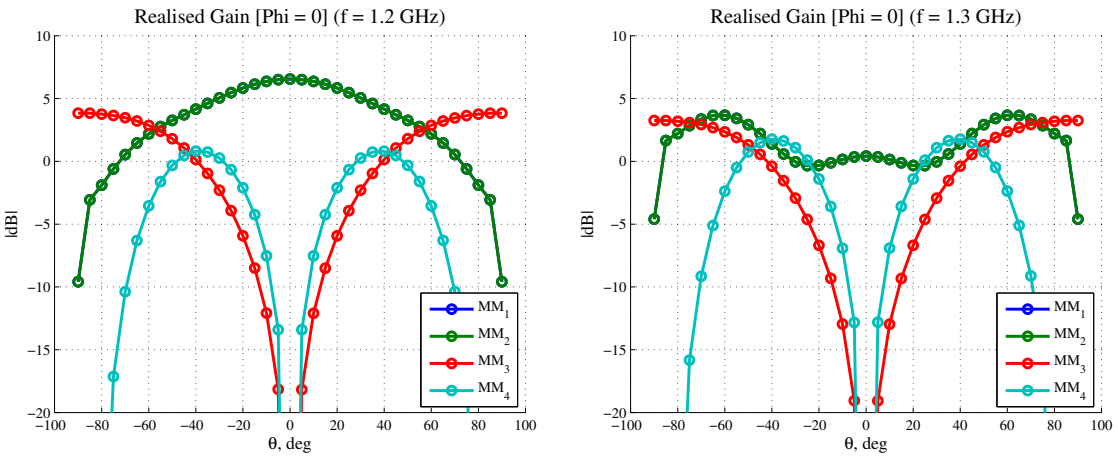

(a) (b)

Figure 3.32: Simulated realised gain of the conical quad-mode antenna over an infinite ground plane for the four orthogonal TEM excitation modes at (a) 1.2 GHz and (b) 1.3 GHz in the $\phi = 0$ plane.

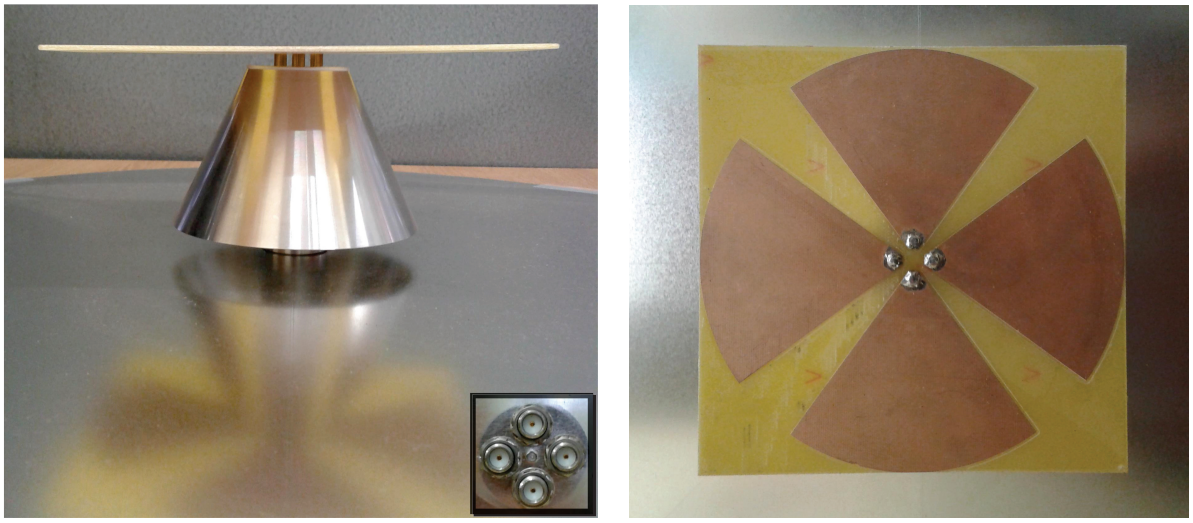

(a) (b)

Figure 3.33: Conical quad-mode antenna design on finite circular ground plane (a) side view showing the four SE SMA connectors (b) top view of printed bow-ties.

The input reflection coefficients of the four orthogonal modes simulated in CST using a multi-pin port excitation are compared to the results obtained from the transformed SE S-matrix in the graph in Fig. 3.34. Similar to the input reflection coefficients of the conical quad-mode antenna simulated over an infinite ground plane, shown in Fig. 3.29, the input reflection coefficients of modes MM_1 – MM_3 are seen to be below -10 dB over the frequency band ranging from 0.8 GHz to 1.1 GHz, with the reflection coefficients of modes MM_1 and MM_2 near identical over the entire frequency band. The simulated response of mode MM_3 is seen to be slightly dissimilar for the measured design, where this difference in input reflection coefficient can be ascribed to the finite ground plane implemented in the manufactured design.

Next, consider the measured input reflection coefficient of mode MM_3 transformed from the

measured SE S-matrix using (3.35). The measured input reflection coefficient is seen to be shifted in frequency when compared to the simulated response. Regardless of this shift in frequency, the -10 dB match of mode MM_3 is still seen to coincide with the -10 dB frequency bandwidth of modes MM_1 and MM_2. The input reflection coefficients of modes MM_1 and MM_2, are seen to be in better agreement with the simulated response, with both approximately equal to one another over the entire frequency band. Lastly, similar to the simulated response, the measurements show that mode MM_4 is largely mismatched across the band.

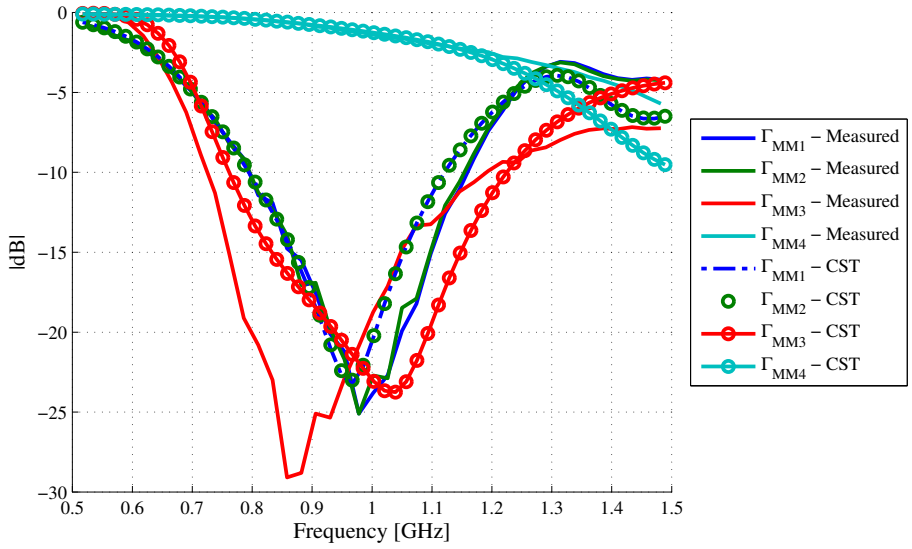

Figure 3.34: Input reflection coefficients of the four orthogonal excitation modes for the conical quad–mode antenna transformed from SE measurements compared to results simulated using the finite ground plane.

Despite these small discrepancies between the simulated and measured response, the measurements still illustrate that two orthogonal dipoles and a conical monopole element can be integrated and individually excited through a single quadraxial transmission line. As the curves in Fig. 3.34 show, an input match below -10 dB can be achieved within the same frequency bandwidth for all three integrated elements of the conical quad-mode antenna.

The radiated far-field patterns corresponding to each of the four orthogonal excitation modes can be solved from the measured radiated far-field of the four SE excitations, using the transformation in (3.38), where similar to the S-matrix transformation, the voltage and current coefficient matrices are given by (3.54) and (3.55), and the SE and multi-mode characteristic impedance matrices are given by (3.57) and (3.58), respectively. The SE far-field patterns are obtained by measuring the co- and cross-polar field components radiated by the conical quad-mode antenna when exciting each SE port, in turn, with the remaining three ports characteristically terminated. The performance of the conical quad-mode antenna is measured in two planes, $\phi = 0°$ and $\phi = 90°$, each respectively parallel to the electric field radiated by the two orthogonal bow-tie dipole elements. The graphs in Fig. 3.35 and Fig. 3.36 compare the simulated co-polar

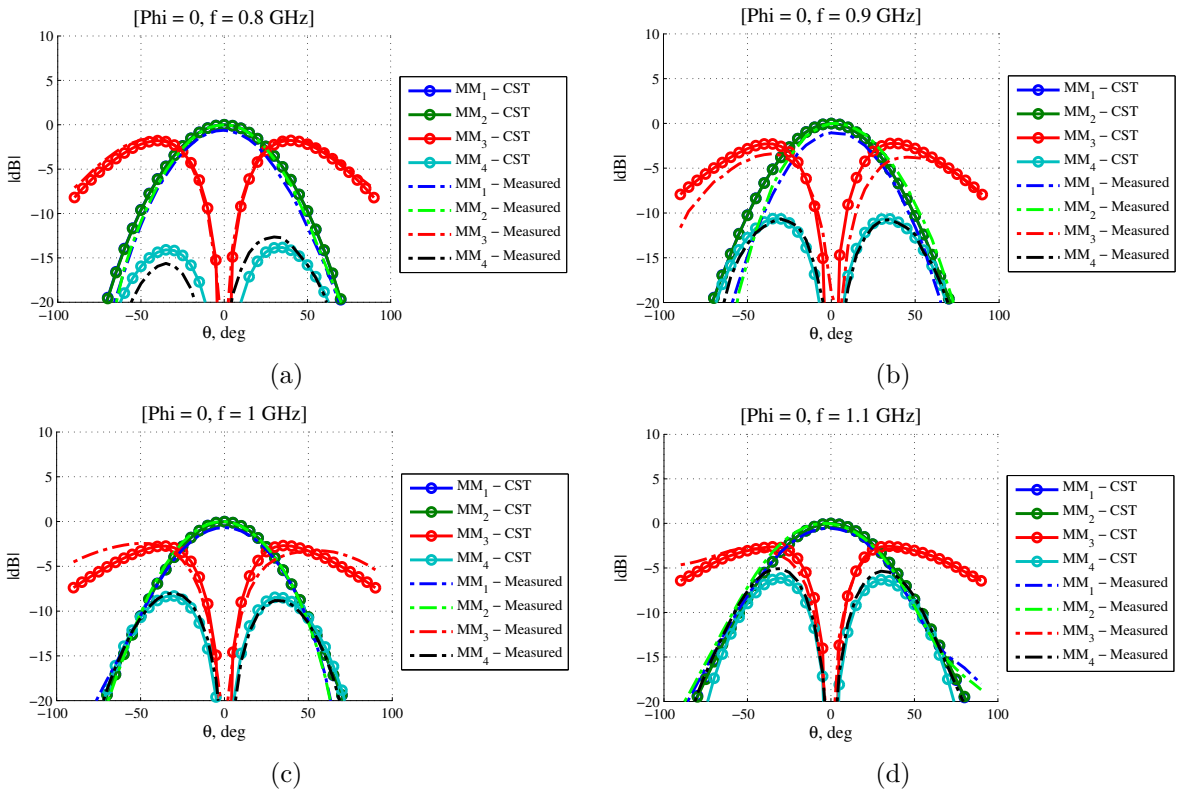

Figure 3.35: Normalised co-polar gain of the conical quad-mode antenna for the four orthogonal excitation modes transformed from SE measurements compared to simulations in the $\phi = 0°$ plane at (a) 0.8 GHz, (b) 0.9 GHz, (c) 1 GHz, and (d) 1.1 GHz.

gain, normalised to the maximum value, to the normalised co-polar gain of each mode obtained through the transformation of the measured SE radiated far-fields in the $\phi = 0°$ and $\phi = 90°$ planes, respectively, at 100 MHz intervals within the frequency band ranging from 0.8 GHz to 1.1 GHz. The effect the finite ground plane has on the radiated far-fields can be seen when comparing the radiation patterns in Fig. 3.35 to the patterns shown in the graphs in Fig. 3.31, where a narrower beamwidth is observed for modes MM_1 and MM_2 and the power radiated by mode MM_3 is seen to be much lower toward $\theta = 90°$. Considering the measured results transformed from the SE radiation patterns, it is seen that the measured response conform to the simulated response. The radiated co-polar fields for excitation modes MM_1 and MM_2 are nearly equal at each frequency point and seen to radiate in a dipole-over-ground fashion. Some measurement artefacts are observed for the measured response of mode MM_3, with regard to asymmetry in the measured patterns and slight variations in the measured power levels as seen in Fig. 3.35(b) and (c). Despite these deviations, the measurements still illustrate the typical monopole radiation pattern excited by mode MM_3. Lastly, excitation mode MM_4 is seen to conform well to the simulated results, displaying an increase in radiated power levels over frequency, that correspond to the decrease in the measured input reflection coefficient in Fig. 3.34.

The same radiation characteristics can be seen in the patterns simulated and measured in the $\phi = 90°$ plane, shown in Fig. 3.36. As expected from the symmetrical design, the radiation

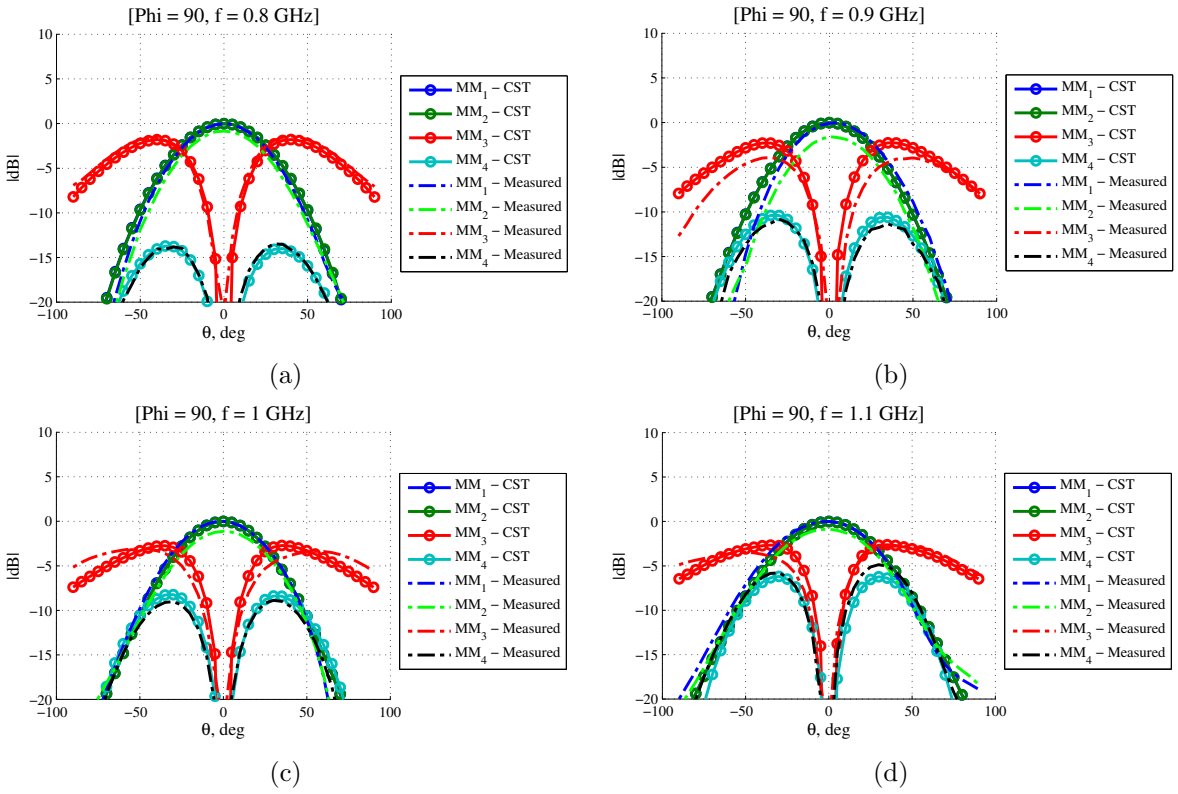

Figure 3.36: Normalised co-polar gain of the conical quad-mode antenna for the four orthogonal excitation modes transformed from SE measurements compared to simulations in the $\phi = 90°$ plane at (a) 0.8 GHz, (b) 0.9 GHz, (c) 1 GHz, and (d) 1.1 GHz.

patterns of each mode is seen to be nearly identical in both the $\phi = 0°$ and $\phi = 90°$ planes. Regardless of these small differences observed between the measured and simulated radiated response, the graphs in Fig. 3.35 and Fig. 3.36 still illustrate that an accurate description of the radiated power corresponding to each orthogonal excitation mode can be obtained from purely SE measurements using the transformation given in (3.38).

3.5 Conclusion

This chapter presents three multi-mode antenna designs allowing for excitation through multiple TEM port modes supported by their multiconductor transmission line feeds. These designs include a dual-mode antenna integrating a single polarisation dipole and monopole excited through a twinaxial transmission line supporting two orthogonal port modes. Through measurements it is illustrated that the dual-mode antenna design allows for two complimentary dipole and monopole radiation patterns each associated with a purely differential- or common-mode excitation. Following from the dual-mode antenna a narrowband cylindrical quad-mode antenna integrating dual-polarised dipoles with a monopole is presented. The cylindrical quad-mode antenna feed comprises a quadraxial transmission line supporting four orthogonal TEM modes through which the quad-mode antenna can be excited. Similar to the dual-mode antenna it is illustrated that each excitation mode results in a unique radiation pattern. The dual-polarised

dipoles are shown to allow for two orthogonal dipole-over-ground radiation patterns and the integrated monopole sleeve enabling the quad-mode antenna to radiate in a typical monopole fashion. Lastly the conical quad-mode antenna design presented in this chapter displays the same radiation characteristics as the cylindrical design but over an improved operating frequency bandwidth. Since these multi-mode antenna designs are excited through multiconductor transmission lines comprising multiple SE inner conductors, an equivalent network representation of a generalised multi-mode antenna is presented to relate the equivalent multi-mode response of the antenna to the case where the antenna is excited solely through the SE conductors. Two expressions are derived by which the S-parameters and radiated far-field patterns corresponding to the multi-mode excitations can be transformed from measured SE S-parameters and far-field patterns. These expressions are validated through all three antenna designs using either simulated results as in the case of the cylindrical quad-mode antenna, or measured results as done for the dual-mode and conical quad-mode antenna designs. Given the complimentary nature of the dipole and monopole radiation patterns supported by these antenna designs, all three antennas allow for near-hemispherical FoV coverage. In Chapter 4 an equivalent model for an active multi-mode antenna element applying complex beamforming weights to each excitation mode is presented. Using beamforming algorithms conventionally applied to single-mode phased array antenna elements, complex beamforming weights are derived for an active dual-mode as well as an active quad-mode antenna in order to maximise the gain, sensitivity and polarimetric performance of the antennas over the hemispherical FoV coverage.

Chapter 4

Active Multi-Mode Antennas

Chapter 3 introduced the concept of a multi-mode antenna element excited through a multi-conductor transmission line, allowing for multiple orthogonal transverse electromagnetic (TEM) excitation modes. The theory is applied to the analysis and design of three multi-mode antenna elements: a dual-mode antenna excited through two orthogonal excitation modes and cylindrical and conical quad-mode antennas allowing for excitation through four orthogonal TEM modes. As illustrated in Chapter 3, each excitation mode results in a unique radiation pattern.

This chapter presents beamforming algorithms which allow designers to exploit the capabilities of multi-mode antenna elements, by combining the radiation patterns of the different modes in a controlled fashion to create patterns which offer improved sensitivity and polarimetric performance over an enhanced Field-of-View (FoV) coverage. Firstly, an equivalent receiver model through which the signal, noise, and polarimetric performance of these multi-mode antenna elements can be characterised is presented. The application of classical beamforming algorithms to the multi-mode network and noise model descriptions is demonstrated [45, 46]. An equivalent model of a multi-mode active receiving antenna is introduced in Sec. 4.1 along with derivations of the multi-mode Low-Noise Amplifier (LNA) signal and noise models. Using the equivalent receiver model an expression is derived for the sensitivity of an active multi-mode receiving antenna. In order to assess the polarimetric performance, a polarimeter model for a multi-mode receiving antenna is presented and the figure-of-merit used to characterise the polarimetric performance is introduced. In Sec. 4.2 popular beamforming algorithms are introduced that can be implemented to maximise the antenna gain or sensitivity, and to polarimetrically calibrate the response of a multi-mode antenna. Using the equivalent receiver model, the performance of the dual-mode and conical quad-mode antenna are characterised through the implementation of various beamforming algorithms in Sec. 4.3 and 4.4.

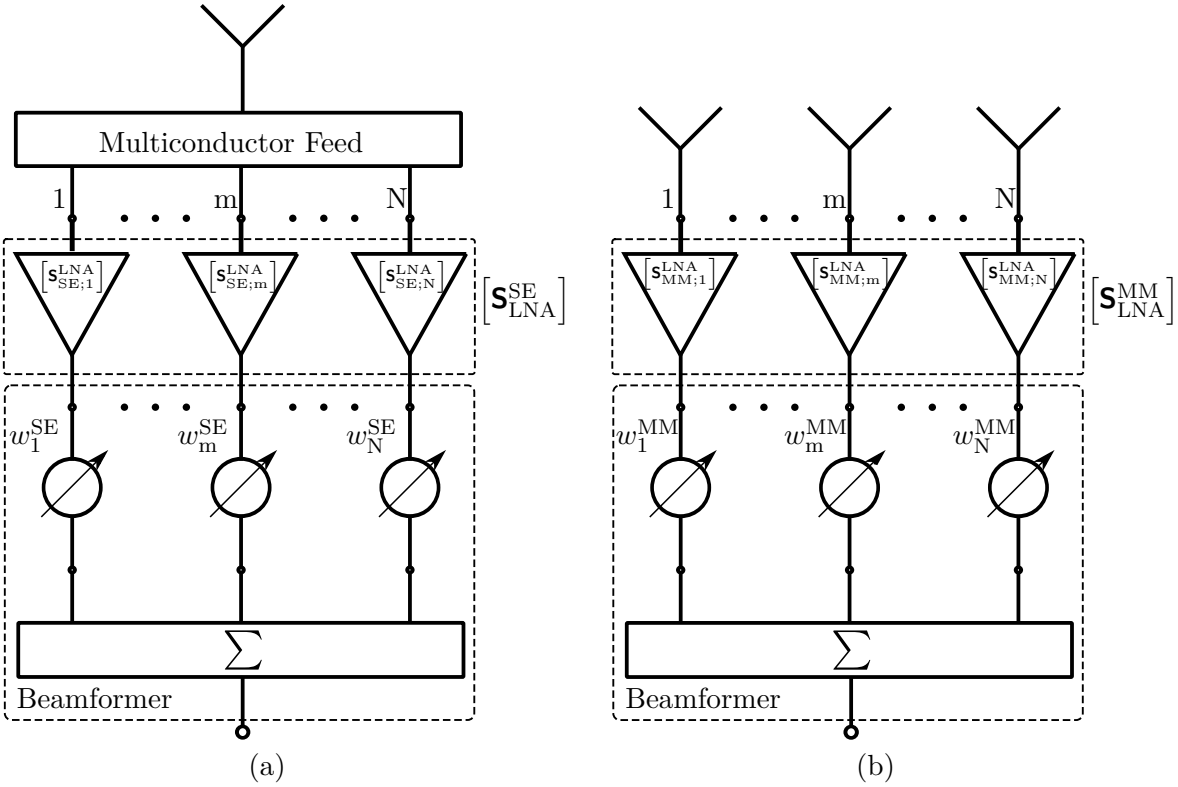

Figure 4.1: Multi-mode active receiver model (a) SE representation (b) Multi-mode representation.

4.1 Multi-Mode Receivers

Following on the network representation of a multi-mode antenna element derived in Sec. 3.2.1, an equivalent model for an active multi-mode receiving antenna is introduced in this section. To this end, consider a single multi-mode antenna element consisting of a number of co-located radiating elements excited through a single multiconductor transmission line comprising N Single-Ended (SE) conductors. As shown in Fig. 4.1(a), each of the SE transmission lines are connected to a SE LNA resulting in an active multiconductor antenna element. The output of each SE LNA is connected to a beamformer that assigns a complex weight value to each of the SE channels and sums all the channels to form a single beam produced at the output port. Throughout the analysis presented in this section the following assumptions are applied: (1) each SE LNA is identical to all the others, unilateral, and isolated from the others, with uncorrelated noise sources, (2) the output of the LNAs are matched to the input of the beamformer, which is considered lossless. Applying these theoretical constraints on the receiver components do not affect the conclusions drawn from the presented work.

4.1.1 Equivalent multi-mode signal and noise model

To derive an equivalent model for a multi-mode active receiver, first consider the SE radiation patterns excited by each SE conductor of the multiconductor transmission line. Analogous to the description given in Sec. 3.2.1, the vector of radiated fields ($\mathbf{F}^{\mathrm{p}}_{\mathrm{SE}}$) is defined in a set

of spherical coordinates in the far-field region and can therefore be expressed as in (3.37), where p denotes either the θ or ϕ field components. Applying the transformations in (3.35) and (3.38), the SE far-fields and S-matrix ($\mathbf{S}_{\text{SE}}$) of the multi-mode antenna element can be transformed into the equivalent response corresponding to the N orthogonal TEM excitation modes supported by the multiconductor transmission line. With the response of the multi-mode antenna element described by the S-matrix $\mathbf{S}_{\text{MM}}$ and the radiated far-field vectors $\mathbf{F}^{\text{p}}_{\text{MM}}$, a multi-mode antenna element can be represented by an N element antenna array, shown in Fig. 4.1(b), where each array element corresponds to one of the orthogonal TEM excitation modes. In order to characterise the signal and noise performance of the multi-mode active receiving antenna, equivalent multi-mode S- and noise parameters of the SE LNAs connected to the multiconductor transmission line feed are first derived. Note that currently, no general multi-mode noise description for embedded noisy two-ports exist.

Low-noise amplifier: Multi-mode S-matrix

Consider the network representation of identical SE LNAs connected to the N symmetric inner conductors of a multiconductor transmission line illustrated in Fig. 4.2(a). The response of each LNA is described by the same $[2 \times 2]$ S-matrix for an input and output characteristic port impedance Z_0. Hence $\mathbf{S}^{\text{LNA}}_{\text{SE;1}} = ... = \mathbf{S}^{\text{LNA}}_{\text{SE;N}}$ and, given that the SE LNAs are isolated from each other, the response of all SE LNAs can be represented by a $[2N \times 2N]$ block diagonal matrix containing the N S-matrices of all the SE LNAs, i.e.

$$\mathbf{S}^{\text{SE}}_{\text{LNA}} = \begin{bmatrix} \left[\mathbf{S}^{\text{LNA}}_{\text{SE;1}}\right] & \cdots & [\mathbf{0}] \\ \vdots & \ddots & \vdots \\ [\mathbf{0}] & \cdots & \left[\mathbf{S}^{\text{LNA}}_{\text{SE;N}}\right] \end{bmatrix}, \tag{4.1}$$

where $[\mathbf{0}]$ denotes a $[2 \times 2]$ zero matrix. For a multi-mode model, the aim is to develop an equivalent representation such as shown in Fig. 4.2(b).

Figure 4.2(b) shows the network representation of a set of equivalent LNAs when excited by the N orthogonal TEM modes supported by the multiconductor transmission line feed. It follows from Sec. 3.2.1 that the equivalent multi-mode voltages and currents at the ports of the LNAs can be defined as linear combinations of the SE voltages and currents depicted in Fig. 4.2(a) using the coefficients expressed in (3.19) and (3.20). For the port numbering illustrated in Fig. 4.2 the multi-mode voltages and currents can therefore be expressed in terms of the SE

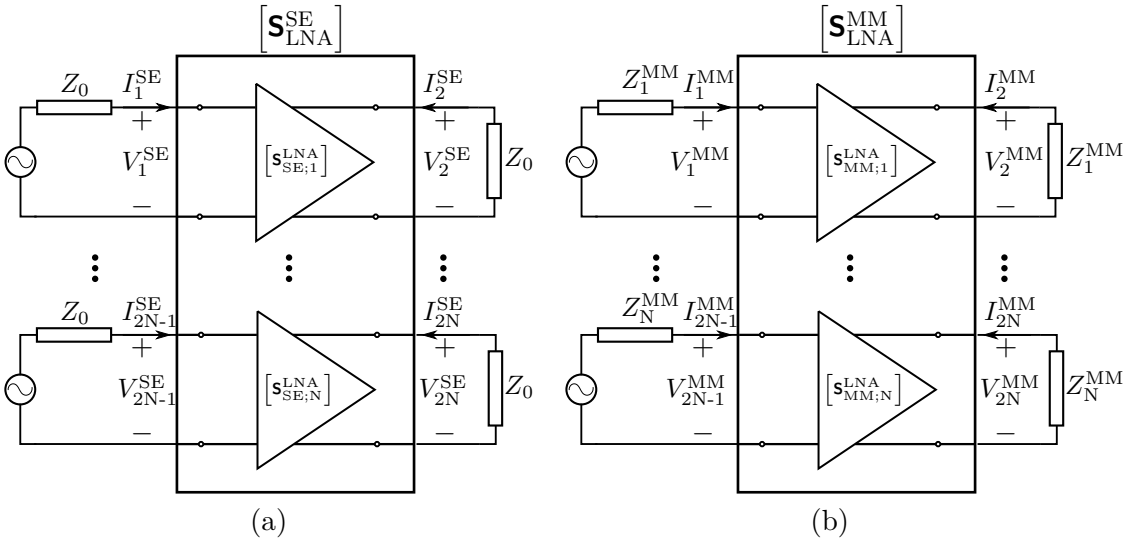

Figure 4.2: Network representations of (a) the N SE LNAs (b) the equivalent multi-mode response of the N orthogonal TEM excitations.

voltages and currents as

$$\mathbf{V}^{\mathrm{MM}}_{\mathrm{LNA}} = \begin{bmatrix} V^{\mathrm{MM}}_1 \\ V^{\mathrm{MM}}_2 \\ \vdots \\ V^{\mathrm{MM}}_{2N-1} \\ V^{\mathrm{MM}}_{2N} \end{bmatrix} = \mathbf{K}^{\mathrm{v}}_{\mathrm{LNA}} \mathbf{V}^{\mathrm{SE}}_{\mathrm{LNA}} = \begin{bmatrix} k^{\mathrm{v}}_{11} & 0 & k^{\mathrm{v}}_{12} & 0 & \cdots & k^{\mathrm{v}}_{1N} & 0 \\ 0 & k^{\mathrm{v}}_{11} & 0 & k^{\mathrm{v}}_{12} & \cdots & 0 & k^{\mathrm{v}}_{1N} \\ \vdots & 0 & \vdots & 0 & \cdots & \vdots & 0 \\ 0 & \vdots & 0 & \vdots & \cdots & 0 & \vdots \\ k^{\mathrm{v}}_{N1} & 0 & k^{\mathrm{v}}_{N2} & 0 & \cdots & k^{\mathrm{v}}_{NN} & 0 \\ 0 & k^{\mathrm{v}}_{N1} & 0 & k^{\mathrm{v}}_{N2} & \cdots & 0 & k^{\mathrm{v}}_{NN} \end{bmatrix} \begin{bmatrix} V^{\mathrm{SE}}_1 \\ V^{\mathrm{SE}}_2 \\ \vdots \\ V^{\mathrm{SE}}_{2N-1} \\ V^{\mathrm{SE}}_{2N} \end{bmatrix} \tag{4.2a}$$

$$\mathbf{I}^{\mathrm{MM}}_{\mathrm{LNA}} = \begin{bmatrix} I^{\mathrm{MM}}_1 \\ I^{\mathrm{MM}}_2 \\ \vdots \\ I^{\mathrm{MM}}_{2N-1} \\ I^{\mathrm{MM}}_{2N} \end{bmatrix} = \mathbf{K}^{\mathrm{i}}_{\mathrm{LNA}} \mathbf{I}^{\mathrm{SE}}_{\mathrm{LNA}} = \begin{bmatrix} k^{\mathrm{i}}_{11} & 0 & k^{\mathrm{i}}_{12} & 0 & \cdots & k^{\mathrm{i}}_{1N} & 0 \\ 0 & k^{\mathrm{i}}_{11} & 0 & k^{\mathrm{i}}_{12} & \cdots & 0 & k^{\mathrm{i}}_{1N} \\ \vdots & 0 & \vdots & 0 & \cdots & \vdots & 0 \\ 0 & \vdots & 0 & \vdots & \cdots & 0 & \vdots \\ k^{\mathrm{i}}_{N1} & 0 & k^{\mathrm{i}}_{N2} & 0 & \cdots & k^{\mathrm{i}}_{NN} & 0 \\ 0 & k^{\mathrm{i}}_{N1} & 0 & k^{\mathrm{i}}_{N2} & \cdots & 0 & k^{\mathrm{i}}_{NN} \end{bmatrix} \begin{bmatrix} I^{\mathrm{SE}}_1 \\ I^{\mathrm{SE}}_2 \\ \vdots \\ I^{\mathrm{SE}}_{2N-1} \\ I^{\mathrm{SE}}_{2N} \end{bmatrix} \tag{4.2b}$$

where the odd and even numbered voltage and current indexes refer to the input and output ports of each network representation. Once again the elements of the voltage and current coefficient matrices $\{\mathbf{K}^{\mathrm{v}}_{\mathrm{LNA}}, \mathbf{K}^{\mathrm{i}}_{\mathrm{LNA}}\}$ should conform to the power relation given in (3.24).

From these definitions for the voltage and current coefficient matrices the SE S-matrix $\mathbf{S}^{\mathrm{SE}}_{\mathrm{LNA}}$ can be transformed into the equivalent multi-mode S-matrix using

$$\mathbf{S}^{\mathrm{MM}}_{\mathrm{LNA}} = \left[\mathbf{K}^{\mathrm{LNA}}_{\mathrm{ab}} + \mathbf{K}^{\mathrm{LNA}}_{\mathrm{aa}} \mathbf{S}^{\mathrm{SE}}_{\mathrm{LNA}}\right] \left[\mathbf{K}^{\mathrm{LNA}}_{\mathrm{aa}} + \mathbf{K}^{\mathrm{LNA}}_{\mathrm{ab}} \mathbf{S}^{\mathrm{SE}}_{\mathrm{LNA}}\right]^{-1}, \tag{4.3}$$

where similar to (3.32a) and (3.32b), the matrices $\mathbf{K}_{\mathrm{aa}}^{\mathrm{LNA}}$ and $\mathbf{K}_{\mathrm{ab}}^{\mathrm{LNA}}$ are defined as

$$\mathbf{K}_{\mathrm{aa}}^{\mathrm{LNA}} = \frac{1}{2}\left[\mathbf{Z}_{\mathrm{MM}}\right]^{-\frac{1}{2}}\mathbf{K}_{\mathrm{LNA}}^{\mathrm{v}}\left[\mathbf{Z}_{\mathrm{SE}}\right]^{\frac{1}{2}} + \frac{1}{2}\left[\mathbf{Z}_{\mathrm{MM}}\right]^{\frac{1}{2}}\mathbf{K}_{\mathrm{LNA}}^{\mathrm{i}}\left[\mathbf{Z}_{\mathrm{SE}}\right]^{-\frac{1}{2}} \tag{4.4a}$$

$$\mathbf{K}_{\mathrm{ab}}^{\mathrm{LNA}} = \frac{1}{2}\left[\mathbf{Z}_{\mathrm{MM}}\right]^{-\frac{1}{2}}\mathbf{K}_{\mathrm{LNA}}^{\mathrm{v}}\left[\mathbf{Z}_{\mathrm{SE}}\right]^{\frac{1}{2}} - \frac{1}{2}\left[\mathbf{Z}_{\mathrm{MM}}\right]^{\frac{1}{2}}\mathbf{K}_{\mathrm{LNA}}^{\mathrm{i}}\left[\mathbf{Z}_{\mathrm{SE}}\right]^{-\frac{1}{2}} \tag{4.4b}$$

with $\mathbf{Z}_{\mathrm{SE}}$ and $\mathbf{Z}_{\mathrm{MM}}$ denoting the $[2N \times 2N]$ diagonal SE and multi-mode characteristic impedance matrices of the form

$$\mathbf{Z}_{\mathrm{SE}} = \begin{bmatrix} Z_0 & \cdots & 0 \\ \vdots & \ddots & \vdots \\ 0 & \cdots & Z_0 \end{bmatrix} \tag{4.5}$$

and

$$\mathbf{Z}_{\mathrm{MM}} = \begin{bmatrix} Z_1^{\mathrm{MM}} & 0 & \cdots & 0 & 0 \\ 0 & Z_1^{\mathrm{MM}} & \cdots & 0 & 0 \\ \vdots & \vdots & \ddots & \vdots & \vdots \\ 0 & 0 & \cdots & Z_{\mathrm{N}}^{\mathrm{MM}} & 0 \\ 0 & 0 & \cdots & 0 & Z_{\mathrm{N}}^{\mathrm{MM}} \end{bmatrix}. \tag{4.6}$$

Note that for the special case where the SE input and output ports are isolated, the equivalent multi-mode characteristic impedance matrix can be obtained from

$$\mathbf{Z}_{\mathrm{MM}} = \mathbf{K}_{\mathrm{LNA}}^{\mathrm{v}}\mathbf{Z}_{\mathrm{SE}}\left[\mathbf{K}_{\mathrm{LNA}}^{\mathrm{i}}\right]^{-1}. \tag{4.7}$$

Using (4.3) the response of the N isolated and identical SE LNAs for N orthogonal excitation modes described by the coefficient matrices $\{\mathbf{K}_{\mathrm{LNA}}^{\mathrm{v}}, \mathbf{K}_{\mathrm{LNA}}^{\mathrm{i}}\}$ can be expressed as an equivalent block diagonal S-matrix containing the $[2 \times 2]$ S-matrices $\{\mathbf{S}_{\mathrm{MM;1}}^{\mathrm{LNA}}, ..., \mathbf{S}_{\mathrm{MM;N}}^{\mathrm{LNA}}\}$ corresponding to each excitation mode, i.e.

$$\mathbf{S}_{\mathrm{LNA}}^{\mathrm{MM}} = \begin{bmatrix} \left[\mathbf{S}_{\mathrm{MM;1}}^{\mathrm{LNA}}\right] & \cdots & [\mathbf{0}] \\ \vdots & \ddots & \vdots \\ [\mathbf{0}] & \cdots & \left[\mathbf{S}_{\mathrm{MM;N}}^{\mathrm{LNA}}\right] \end{bmatrix}. \tag{4.8}$$

It is worth noting that this block diagonal form of the multi-mode S-matrix is only obtained for identical, isolated SE LNAs transformed to N orthogonal excitation modes using the specific port numbering system in Fig. 4.2. The response of the multi-mode receiver for each of the orthogonal TEM excitation modes can therefore be represented by a two-port S-matrix $\mathbf{S}_{\mathrm{MM;m}}^{\mathrm{LNA}}$. In the following section the equivalent two-port noise parameters for each of the multi-mode excitations of the receiver are derived.

Low-noise amplifier: Multi-mode Noise parameters

A noisy two-port network is generally modelled as a combination of a noiseless two-port network, representing the signal response, and two external noise sources applied to the input and output

ports. Figure 4.3 shows three of the common equivalent network representations for noisy two-port networks.

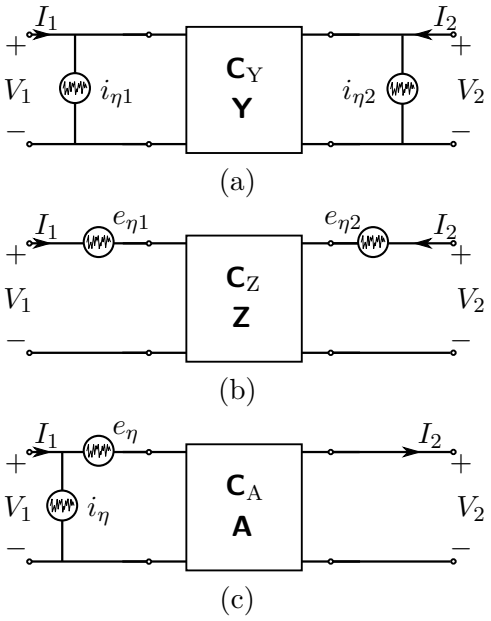

Figure 4.3: Equivalent noise representation of two-port networks (a) admittance representation (b) impedance representation (c) chain representation.

In Fig. 4.3, (a) is the admittance representation with the signal response represented by a noiseless admittance matrix $\mathbf{Y}$ and the noise modelled with two noise current sources applied to the input and output ports, (b) the impedance representation with an impedance matrix $\mathbf{Z}$ representing the signal response of the two-port and a noise voltage source applied to each port, and lastly (c) the chain representation where the signal response is modelled through an $ABCD$-matrix, denoted as $\mathbf{A}$, with a voltage and current noise source applied to the input port modelling the noise response. A physically significant representation of the two noise sources of each representation is given by their self- and cross-power spectral densities, which when arranged in matrix form constitutes the noise correlation matrix $\left(\mathbf{C}_{\mathrm{Y/Z/A}}\right)$ – henceforth referred to only as the correlation matrix [47, 48].

To derive an equivalent set of noise parameters that corresponds to each excitation of the multi-mode response, the SE and multi-mode network representation of the LNAs [c.f. Fig. 4.2] are modelled with external noise sources configured in the chain representation as illustrated in Fig. 4.4(a) with ν representing either the SE or multi-mode (MM) response.

A convenient trait of the chain correlation matrix is the direct relation it has with the noise parameters of the noisy two-port network [49]. Therefore, first consider the equivalent SE schematic representation of the multi-port receiver illustrated in Fig. 4.4(a). Each of the N

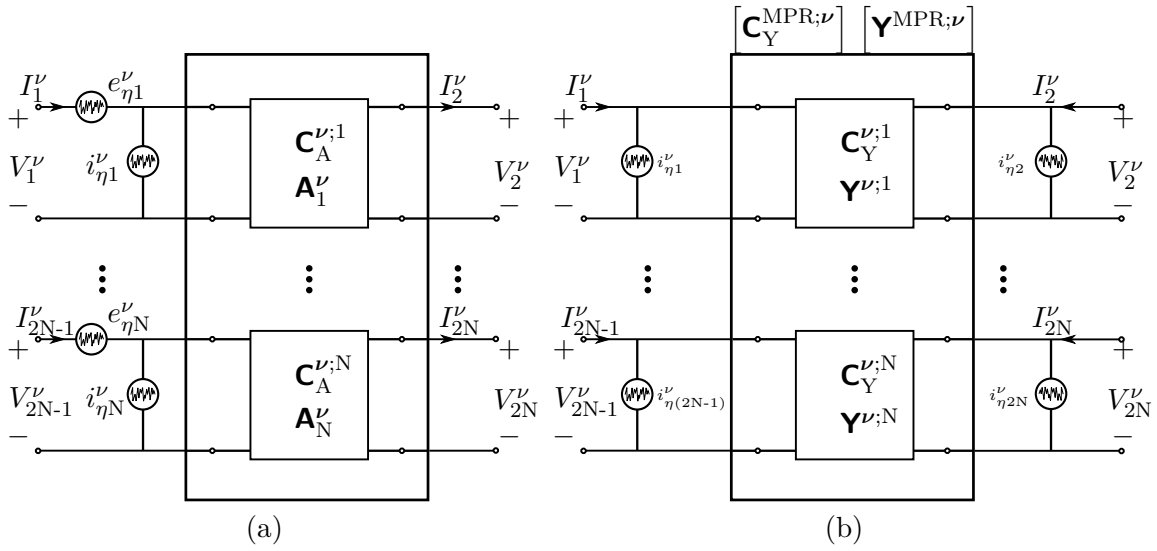

Figure 4.4: Equivalent noise representation of the multi-port LNA network (a) chain representation (b) admittance representation.

LNAs is represented as a noiseless $ABCD$-matrix of the form

$$\mathbf{A}_{\mathrm{m}}^{\mathrm{SE}} = \begin{bmatrix} A_{\mathrm{SE;m}} & B_{\mathrm{SE;m}} \\ C_{\mathrm{SE;m}} & D_{\mathrm{SE;m}} \end{bmatrix} \quad \forall\, \mathrm{m} = 1, ..., N \tag{4.9}$$

with the noise behaviour described by the chain correlation matrix [49], i.e.

$$\begin{aligned} \mathbf{C}_{\mathrm{A}}^{\mathrm{SE;m}} &= \frac{1}{2} \begin{bmatrix} \langle e_{\eta\mathrm{m}} e_{\eta\mathrm{m}}^* \rangle & \langle e_{\eta\mathrm{m}} i_{\eta\mathrm{m}}^* \rangle \\ \langle i_{\eta\mathrm{m}} e_{\eta\mathrm{m}}^* \rangle & \langle i_{\eta\mathrm{m}} i_{\eta\mathrm{m}}^* \rangle \end{bmatrix} \\ &= 2k_{\mathrm{B}}T_0 \begin{bmatrix} R_{\mathrm{n}}^{\mathrm{SE;m}} & \frac{F_{\mathrm{min}}^{\mathrm{SE;m}}-1}{2} - R_{\mathrm{n}}^{\mathrm{SE;m}} \left(Y_{\mathrm{opt}}^{\mathrm{SE;m}}\right)^* \\ \frac{F_{\mathrm{min}}^{\mathrm{SE;m}}-1}{2} - R_{\mathrm{n}}^{\mathrm{SE;m}} \left(Y_{\mathrm{opt}}^{\mathrm{SE;m}}\right) & R_{\mathrm{n}}^{\mathrm{SE;m}} |Y_{\mathrm{opt}}^{\mathrm{SE;m}}|^2 \end{bmatrix}, \quad \forall\, \mathrm{m} = 1, ..., N \end{aligned} \tag{4.10}$$

where $\{\langle e_{\eta\mathrm{m}} e_{\eta\mathrm{m}}^* \rangle, \langle i_{\eta\mathrm{m}} i_{\eta\mathrm{m}}^* \rangle\}$ and $\{\langle e_{\eta\mathrm{m}} i_{\eta\mathrm{m}}^* \rangle, \langle i_{\eta\mathrm{m}} e_{\eta\mathrm{m}}^* \rangle\}$ denote the auto- and cross-correlated spectral densities of the voltage and current noise source, k_{B} the Boltzmann constant, T_0 the standard temperature (290 K), and $\{F_{\mathrm{min}}^{\mathrm{SE;m}}, R_{\mathrm{n}}^{\mathrm{SE;m}}, Y_{\mathrm{opt}}^{\mathrm{SE;m}}\}$ the minimum noise factor, noise resistance, and optimum source admittance of each SE LNA respectively.

Given that the LNAs are identical, the elements of each chain correlation matrix in $\mathbf{C}_{\mathrm{A}}^{\mathrm{SE;m}}$ can be represented by

$$\mathbf{C}_{\mathrm{A}}^{\mathrm{SE;m}} = \begin{bmatrix} C_{\mathrm{A;11}} & C_{\mathrm{A;12}} \\ C_{\mathrm{A;21}} & C_{\mathrm{A;22}} \end{bmatrix} \quad \forall\, \mathrm{m} = 1, ..., N. \tag{4.11}$$

In order to obtain the equivalent multi-mode chain correlation matrices, the SE chain representation of the multi-port LNA network is first transformed into the equivalent SE admittance representation illustrated in Fig. 4.4(b), where (for ν = SE) each LNA is represented by a

noiseless admittance matrix

$$\mathbf{Y}^{\mathrm{SE;m}} = \begin{bmatrix} Y_{11}^{\mathrm{SE;m}} & Y_{12}^{\mathrm{SE;m}} \\ Y_{21}^{\mathrm{SE;m}} & Y_{22}^{\mathrm{SE;m}} \end{bmatrix} \tag{4.12}$$

with the corresponding admittance noise correlation matrix $\left(\mathbf{C}_{\mathrm{Y}}^{\mathrm{SE;m}}\right)$ representing the noise contributed by two current noise sources applied to the input and output ports. It is worth noting that for a passive network represented by an admittance matrix $\mathbf{Y}$, the corresponding admittance correlation matrix is given by [49]

$$\mathbf{C}_{\mathrm{Y}} = 2k_{\mathrm{B}}T_0\mathrm{Re}\{\mathbf{Y}\}. \tag{4.13}$$

For active devices of which the noise sources are not purely thermal in nature, the relation given in (4.13) does not apply for the admittance matrix of the active device. Instead each two-port chain correlation matrix defined in terms of the SE noise parameters in (4.10) can be transformed into the equivalent admittance correlation matrix depicted in Fig. 4.4(b) using the two-port transformation matrix $\mathbf{T}_{\mathrm{Y}}^{\mathrm{SE;m}}$, introduced in [49], i.e.

$$\mathbf{C}_{\mathrm{Y}}^{\mathrm{SE;m}} = \mathbf{T}_{\mathrm{Y}}^{\mathrm{SE;m}}\mathbf{C}_{\mathrm{A}}^{\mathrm{SE;m}}\left[\mathbf{T}_{\mathrm{Y}}^{\mathrm{SE;m}}\right]^{H}, \tag{4.14}$$

where ^{H} denotes the conjugate-transpose and the transformation matrix $\mathbf{T}_{\mathrm{Y}}^{\mathrm{SE;m}}$ is expressed in terms of the SE admittance parameters

$$\mathbf{T}_{\mathrm{Y}}^{\mathrm{SE;m}} = \begin{bmatrix} -Y_{11}^{\mathrm{SE;m}} & 1 \\ -Y_{21}^{\mathrm{SE;m}} & 0 \end{bmatrix}. \tag{4.15}$$

Since the SE LNAs are isolated and no noise correlation exists between the constituent SE LNAs, the noise response of the multi-port receiver network depicted in Fig. 4.4(b), and denoted by the superscript MPR, can be expressed as a $[2N \times 2N]$ block diagonal matrix consisting of the admittance correlation matrices of all SE LNAs. That is

$$\mathbf{C}_{\mathrm{Y}}^{\mathrm{MPR;SE}} = \begin{bmatrix} \left[\mathbf{C}_{\mathrm{Y}}^{\mathrm{SE;1}}\right] & \cdots & [\mathbf{0}] \\ \vdots & \ddots & \vdots \\ [\mathbf{0}] & \cdots & \left[\mathbf{C}_{\mathrm{Y}}^{\mathrm{SE;N}}\right] \end{bmatrix}, \tag{4.16}$$

where $[\mathbf{0}]$ denotes a $[2 \times 2]$ zero matrix. The SE representation can now be transformed into the equivalent multi-mode representation corresponding to the N orthogonal excitation modes defined using the coefficient matrices in (4.2a) and (4.2b). Starting with the definition of the multi-mode admittance matrix relating the multi-mode currents to the equivalent voltages

$$\mathbf{I}_{\mathrm{LNA}}^{\mathrm{MM}} = \mathbf{Y}^{\mathrm{MPR;MM}}\mathbf{V}_{\mathrm{LNA}}^{\mathrm{MM}} \tag{4.17}$$

the total multi-mode admittance matrix can be related to the equivalent SE admittance matrix

by substituting (4.2a) and (4.2b) into (4.17), i.e.

$$\mathbf{Y}^{\mathrm{MPR;MM}} = \mathbf{K}^{\mathrm{i}}_{\mathrm{LNA}} \mathbf{Y}^{\mathrm{MPR;SE}} \left[\mathbf{K}^{\mathrm{i}}_{\mathrm{LNA}}\right]^{H}, \tag{4.18}$$

where the SE admittance matrix of the multi-port receiver $\mathbf{Y}^{\mathrm{MPR;SE}}$ is a $[2N \times 2N]$ block-diagonal matrix containing the admittance matrices of each SE LNA $\mathbf{Y}^{\mathrm{SE;m}}$ for m$= 1, ..., N$. Using (4.13) and (4.18) it can be shown that, for real valued coefficients, the same transformation given in (4.18) applies to the admittance noise correlation matrix. Hence the equivalent multi-mode admittance noise correlation matrix $\mathbf{C}_{\mathrm{Y}}^{\mathrm{MPR;MM}}$ can be derived from the equivalent SE admittance correlation matrix $\mathbf{C}_{\mathrm{Y}}^{\mathrm{MPR;SE}}$ using the current coefficient matrix $\mathbf{K}^{\mathrm{i}}_{\mathrm{LNA}}$, i.e.

$$\mathbf{C}_{\mathrm{Y}}^{\mathrm{MPR;MM}} = \mathbf{K}^{\mathrm{i}}_{\mathrm{LNA}} \mathbf{C}_{\mathrm{Y}}^{\mathrm{MPR;SE}} \left[\mathbf{K}^{\mathrm{i}}_{\mathrm{LNA}}\right]^{T}. \tag{4.19}$$

Given the orthogonal nature of each of the TEM excitation modes, the rows of the current coefficient matrix are linearly independent, and hence the non-zero elements of $\mathbf{K}^{\mathrm{i}}_{\mathrm{LNA}}$ satisfy the condition

$$\sum_{j=1}^{N} k^{\mathrm{i}}_{\mathrm{pj}} k^{\mathrm{i}}_{\mathrm{qj}} = \begin{cases} \sum\limits_{j=1}^{N} |k^{\mathrm{i}}_{\mathrm{pj}}|^2, & p = q \\ 0, & p \neq q \end{cases} \quad \forall \ \mathrm{p, q} = 1, ..., N. \tag{4.20}$$

The admittance and corresponding correlation matrix resulting from (4.18) and (4.19) are therefore block diagonal matrices of the form

$$\mathbf{Y}^{\mathrm{MPR;MM}} = \begin{bmatrix} \sum\limits_{j=1}^{N} |k^{\mathrm{i}}_{1\mathrm{j}}|^2 \left[\mathbf{Y}^{\mathrm{SE;1}}\right] & \cdots & [\mathbf{0}] \\ \vdots & \ddots & \vdots \\ [\mathbf{0}] & \cdots & \sum\limits_{j=1}^{N} |k^{\mathrm{i}}_{\mathrm{Nj}}|^2 \left[\mathbf{Y}^{\mathrm{SE;N}}\right] \end{bmatrix} = \begin{bmatrix} \left[\mathbf{Y}^{\mathrm{MM;1}}\right] & \cdots & [\mathbf{0}] \\ \vdots & \ddots & \vdots \\ [\mathbf{0}] & \cdots & \left[\mathbf{Y}^{\mathrm{MM;N}}\right] \end{bmatrix}, \tag{4.21}$$

with $\mathbf{Y}^{\mathrm{MM;m}}$ denoting the admittance matrix of the multi-port receiver when excited through mode m$= 1, ..., N$, i.e.

$$\mathbf{Y}^{\mathrm{MM;m}} = \begin{bmatrix} Y_{11}^{\mathrm{MM;m}} & Y_{12}^{\mathrm{MM;m}} \\ Y_{21}^{\mathrm{MM;m}} & Y_{22}^{\mathrm{MM;m}} \end{bmatrix} \tag{4.22}$$

and

$$\mathbf{C}_{\mathrm{Y}}^{\mathrm{MPR;MM}} = \begin{bmatrix} \sum\limits_{j=1}^{N} |k^{\mathrm{i}}_{1\mathrm{j}}|^2 \left[\mathbf{C}_{\mathrm{Y}}^{\mathrm{SE;1}}\right] & \cdots & [\mathbf{0}] \\ \vdots & \ddots & \vdots \\ [\mathbf{0}] & \cdots & \sum\limits_{j=1}^{N} |k^{\mathrm{i}}_{\mathrm{Nj}}|^2 \left[\mathbf{C}_{\mathrm{Y}}^{\mathrm{SE;N}}\right] \end{bmatrix} = \begin{bmatrix} \left[\mathbf{C}_{\mathrm{Y}}^{\mathrm{MM;1}}\right] & \cdots & [\mathbf{0}] \\ \vdots & \ddots & \vdots \\ [\mathbf{0}] & \cdots & \left[\mathbf{C}_{\mathrm{Y}}^{\mathrm{MM;N}}\right] \end{bmatrix}. \tag{4.23}$$

Note again that the block diagonal form of the multi-mode admittance and admittance correlation matrices are only achieved when transforming identical, isolated SE LNAs of which the noise generated by the LNAs are uncorrelated from one another, into N orthogonal excitation modes through a current coefficient matrix defined as in (4.2b). The equivalent admittance cor-

relation matrix of each mode $\mathbf{C}_{\mathrm{Y}}^{\mathrm{MM;m}}$ can now be transformed into the chain correlation matrix $\mathbf{C}_{\mathrm{A}}^{\mathrm{MM;m}}$ corresponding to the $ABCD$-matrix representation of each mode [49]. That is

$$\mathbf{C}_{\mathrm{A}}^{\mathrm{MM;m}} = \mathbf{T}_{\mathrm{A}}^{\mathrm{MM;m}} \mathbf{C}_{\mathrm{Y}}^{\mathrm{MM;m}} \left[\mathbf{T}_{\mathrm{A}}^{\mathrm{MM;m}}\right]^{H} \quad \forall\, \mathrm{m} = 1, ..., N \tag{4.24}$$

which, given the relation between the multi-mode and SE admittance correlation matrices in (4.23), can be expressed as

$$\mathbf{C}_{\mathrm{A}}^{\mathrm{MM;m}} = \mathbf{T}_{\mathrm{A}}^{\mathrm{MM;m}} \left(\kappa_{\mathrm{m}} \mathbf{C}_{\mathrm{Y}}^{\mathrm{SE;m}}\right) \left[\mathbf{T}_{\mathrm{A}}^{\mathrm{MM;m}}\right]^{H} \quad \forall\, \mathrm{m} = 1, ..., N \tag{4.25}$$

with $\kappa_{\mathrm{m}} = \sum_{j=1}^{N} |k_{\mathrm{mj}}^{\mathrm{i}}|^2$ and

$$\mathbf{T}_{\mathrm{A}}^{\mathrm{MM;m}} = \begin{bmatrix} 0 & B^{\mathrm{MM;m}} \\ 1 & D^{\mathrm{MM;m}} \end{bmatrix}, \tag{4.26}$$

where the $ABCD$-parameters in the transformation matrix $\mathbf{T}_{\mathrm{A}}^{\mathrm{MM;m}}$ can be expressed in terms of the SE admittance parameters of the constituent SE LNAs [50], i.e.

$$\begin{aligned} B^{\mathrm{MM;m}} &= -\frac{1}{Y_{21}^{\mathrm{MM;m}}} = -\frac{1}{\kappa_{\mathrm{m}} Y_{21}^{\mathrm{SE;m}}} \\ D^{\mathrm{MM;m}} &= -\frac{Y_{11}^{\mathrm{MM;m}}}{Y_{21}^{\mathrm{MM;m}}} = -\frac{Y_{11}^{\mathrm{SE;m}}}{Y_{21}^{\mathrm{SE;m}}}. \end{aligned} \tag{4.27}$$

By substituting (4.14) into (4.25) with the transformation matrix $\mathbf{T}_{\mathrm{A}}^{\mathrm{MM;m}}$ expressed in terms of the SE admittance parameters as given in (4.27), the elements of the chain correlation matrix associated with the m-th mode can be expressed in terms of the elements of the SE chain correlation matrix defined in (4.11)

$$\mathbf{C}_{\mathrm{A}}^{\mathrm{MM;m}} = \begin{bmatrix} \frac{C_{\mathrm{A;11}}}{\kappa_{\mathrm{m}}} & C_{\mathrm{A;12}} \\ C_{\mathrm{A;21}} & \kappa_{\mathrm{m}} C_{\mathrm{A;22}} \end{bmatrix}. \tag{4.28}$$

Finally, comparing (4.28) to (4.10) the equivalent multi-mode noise parameters of each equivalent two-port can be expressed in terms of the noise parameters of the SE LNAs, resulting in

$$\begin{aligned} F_{\mathrm{min}}^{\mathrm{MM;m}} &= F_{\mathrm{min}}^{\mathrm{SE}} \\ R_{\mathrm{n}}^{\mathrm{MM;m}} &= \frac{R_{\mathrm{n}}^{\mathrm{SE}}}{\kappa_{\mathrm{m}}} \\ Y_{\mathrm{opt}}^{\mathrm{MM;m}} &= \kappa_{\mathrm{m}} Y_{\mathrm{opt}}^{\mathrm{SE}}. \end{aligned} \tag{4.29}$$

Equation set (4.29) shows the relation between the SE noise parameters of each of the N identical and isolated LNAs connected to a multiconductor transmission line and the equivalent noise parameters corresponding to each of the N orthogonal TEM modes supported by the multiconductor transmission line. The expressions show that the minimum noise factor of each orthogonal TEM mode equates to that of the constituent SE LNAs, whereas the equivalent noise resistance and optimum sources admittances corresponding to each excitation mode can be ob-

tained from the SE parameters using κ_{m} solved from the row elements of the current coefficient matrix $\mathbf{K}^{\mathrm{i}}_{\mathrm{LNA}}$.

4.1.2 Sensitivity (Signal-to-Noise Ratio)

As mentioned in Chapter 2, one of the key requirements for the AA receivers of the SKA is high sensitivity over a scan range up to 60° from zenith. Given the multi-mode noise model in Sec. 4.1.1, this section derives an expression for the sensitivity of the multi-mode receiver depicted in Fig. 4.1(b). The sensitivity is expressed in terms of the radiated multi-mode far-field patterns as well as the equivalent multi-mode LNA S-parameters and noise parameters for an arbitrary set of complex beamforming weights $\mathbf{w} = \left[w_1^{\mathrm{MM}} \ldots w_{\mathrm{N}}^{\mathrm{MM}}\right]^T$ applied to the orthogonal TEM excitation modes. Two distinct models for the receiver sensitivity are derived. The first model analyses the sensitivity using the radiated far-fields of a multi-mode antenna defined in the transmit situation and introduces an equivalent uncoupled system model through which the sensitivity can be solved [45]. In the second model the multi-mode receiver is considered in the receiving situation, modelling the sensitivity in terms of the signal and noise waves propagating through the receiver [51]. Although these two models are equivalent and produce proportional solutions for the sensitivity, modelling the sensitivity in the transmit situation provides valuable insight into the effects of the radiation performance of the antenna, the signal and noise performance of the LNAs as well as coupling between the various excitation modes, on the resulting sensitivity of the multi-mode receiver. The receiving sensitivity model on the other hand produces an expression for the sensitivity that allows for a closed-form solution through which the complex beamforming weights can be solved to maximise the sensitivity over the FoV coverage.

Transmit model

The derivation of the sensitivity of the active multi-mode receiver depicted in Fig. 4.1 is based on the equivalent system representation of SE active antenna arrays introduced in [45]. Following the exposition in [45] a single expression is derived to solve the sensitivity of the active multi-mode receiver using either the SE or equivalent multi-mode representation introduced in Sec. 4.1. As defined in (2.1) the sensitivity of a receiver is defined as the ratio of the effective area of the radiating element A_{eff} to the total system noise temperature T_{sys}. For the active multi-mode antenna the effective area can be solved in terms of the weighted gain of the antenna using the well-known reciprocity theorem [12]

$$A_{\mathrm{eff}}(\theta,\phi) = \frac{\lambda^2}{4\pi} G(\theta,\phi) \tag{4.30}$$

where λ denotes the operating wavelength and the gain is defined as

$$G(\theta,\phi) = 4\pi \frac{U_{\mathrm{rad}}(\theta,\phi)}{P_{\mathrm{in}}}. \tag{4.31}$$

In (4.31) $U_{\text{rad}}(\theta,\phi)$ is the total radiation intensity expressed in terms of the weighted radiated far-field patterns – henceforth referred to as Embedded Element Patterns (EEPs) – corresponding to each excitation mode

$$U_{\text{rad}}(\theta,\phi) = \frac{1}{2\eta}\left|\sum_{m=1}^{N} w_{\text{m}}^{\nu}\boldsymbol{f}_{\text{m}}^{\boldsymbol{\nu}}(\theta,\phi)\right|^2 \tag{4.32}$$

with w_{m}^{ν} denoting the complex beamforming weight, $\boldsymbol{f}_{\text{m}}^{\boldsymbol{\nu}}(\theta,\phi)$ the radiated electric far-field vector, ν representing either the SE or equivalent multi-mode representation, η the free-space impedance, and P_{in} the total input power to the multiconductor transmission line port. That is, for a given set of beamforming weights $\mathbf{w}^{\boldsymbol{\nu}} = [w_1^{\nu} \ldots w_{\text{N}}^{\nu}]^T$

$$P_{\text{in}} = (\mathbf{w}^{\boldsymbol{\nu}})^H\left[\boldsymbol{\mathcal{I}} - \mathbf{S}^{\boldsymbol{\nu};\text{ant}}\left(\mathbf{S}^{\boldsymbol{\nu};\text{ant}}\right)^H\right]\mathbf{w}^{\boldsymbol{\nu}} \tag{4.33}$$

where $\mathbf{S}^{\boldsymbol{\nu};\text{ant}}$ denotes the S-matrix of the multi-mode antenna for the corresponding network representation ν, and $\boldsymbol{\mathcal{I}}$ the $[N \times N]$ identity matrix. Note that the weights applied to the radiated EEPs in (4.32) assume the same reference plane as indicated in Fig. 4.1. The effective area of the active multi-mode antenna for an arbitrary set of complex beamforming weights is therefore given by

$$A_{\text{eff}}(\theta,\phi) = \frac{\lambda^2}{2\eta}\left[\frac{|\sum_{m=1}^{N} w_{\text{m}}^{\nu}\boldsymbol{f}_{\text{m}}^{\boldsymbol{\nu}}(\theta,\phi)|^2}{(\mathbf{w}^{\boldsymbol{\nu}})^H\left[\boldsymbol{\mathcal{I}} - \mathbf{S}^{\boldsymbol{\nu};\text{ant}}\left(\mathbf{S}^{\boldsymbol{\nu};\text{ant}}\right)^H\right]\mathbf{w}^{\boldsymbol{\nu}}}\right]. \tag{4.34}$$

It is well known that for a single active antenna, optimum noise performance is achieved when the passive input impedance of the antenna is noise matched to the SE LNA. For active phased array antennas it has been shown that improved noise performance can be obtained when the constituent SE LNAs are noise matched to the active impedance of the antenna array elements [52]. To derive an expression for the equivalent noise temperature of the active multi-mode antenna the active impedance of the multi-mode antenna element is defined in terms of the beamforming weights applied to each excitation. Toward this end, consider the equivalent network representation of the active multi-mode antenna in Fig. 4.5, showing the correlated noise waves $c_{\text{m}}^{\nu(\text{p})}$ emanating from the input and output ports ($\text{p} = 1, 2$) of each LNA ($\text{m} = 1, \ldots N$) for both the SE and multi-mode ($\nu = \text{SE, MM}$) representations.

Under the assumption that the reference impedance at each frequency is chosen such that the SE S-matrix of each LNA is of the form

$$\mathbf{S}_{\text{SE;m}}^{\text{LNA}} = \begin{bmatrix} 0 & S_{12}^{\text{SE;m}} \\ S_{21}^{\text{SE;m}} & 0 \end{bmatrix}, \tag{4.35}$$

the active reflection coefficients of the individual SE channels or modes are solved by expressing the respective noise waves at the output of the ideal power combiner as the superposition of

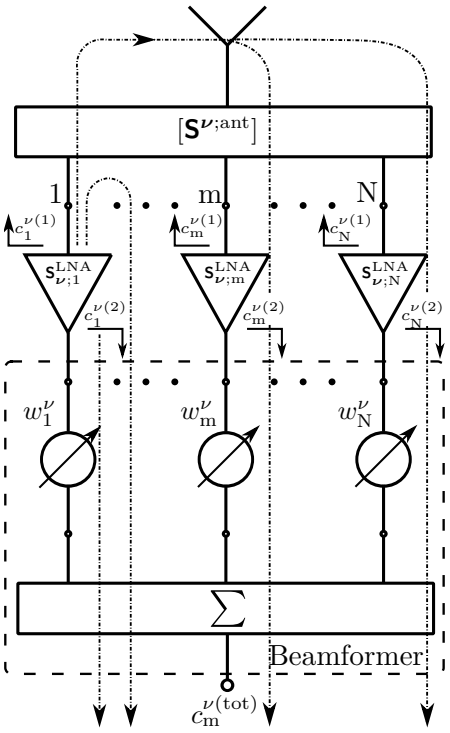

Figure 4.5: Propagation paths of the SE and multi-mode noise waves in the multi-mode active antenna.

three noise wave contributions [52]. That is, for channel or mode m = 1

$$\begin{aligned} c_1^{\nu(\mathrm{tot})} &= \text{Direct Part} + \text{Reflected Part} + \text{Coupled Part} \\ &= w_1^\nu c_1^{\nu(2)} + w_1^\nu c_1^{\nu(1)} S_{11}^{\nu;\mathrm{ant}} S_{21}^{\nu;1} + c_1^{\nu(1)} \sum_{m=2}^{N} w_\mathrm{m}^\nu S_{\mathrm{m}1}^{\nu;\mathrm{ant}} S_{21}^{\nu;\mathrm{m}} \\ &= w_1^\nu c_1^{\nu(2)} + c_1^{\nu(1)} \left[\sum_{m=1}^{N} w_\mathrm{m}^\nu S_{\mathrm{m}1}^{\nu;\mathrm{ant}} S_{21}^{\nu;\mathrm{m}} \right]. \end{aligned} \tag{4.36}$$

For identical LNAs with gains S_{21}^{LNA} it follows that $S_{21}^{\nu;\mathrm{m}} = S_{21}^{\mathrm{LNA}}$ for both the SE and multi-mode representations, therefore

$$\begin{aligned} c_1^{\nu(\mathrm{tot})} &= w_1^\nu \left(c_1^{\nu(2)} + c_1^{\nu(1)} S_{21}^{\mathrm{LNA}} \left[\sum_{m=1}^{N} \frac{w_\mathrm{m}^\nu}{w_1^\nu} S_{\mathrm{m}1}^{\nu;\mathrm{ant}} \right] \right) \\ &= w_1^\nu \left(c_1^{\nu(2)} + c_1^{\nu(1)} S_{21}^{\mathrm{LNA}} \Gamma_{\mathrm{act}}^{\nu;1} \right), \end{aligned} \tag{4.37}$$

where the active reflection coefficient $\Gamma_{\mathrm{act}}^{\nu;\mathrm{q}}$ of each channel or mode (q) is defined as

$$\Gamma_{\mathrm{act}}^{\nu;\mathrm{q}} = \sum_{m=1}^{N} \frac{w_\mathrm{m}^\nu}{w_\mathrm{q}^\nu} S_{\mathrm{qm}}^{\nu;\mathrm{ant}} \quad \forall \quad \mathrm{q} = 1, \ldots, N. \tag{4.38}$$

By applying the active reflection coefficient, the multi-mode active antenna can be represented as N uncoupled channels or modes as shown in Fig. 4.6 [45], with each SE channel or equivalent mode of the multi-mode antenna terminated in their respective active impedance as defined by (4.38).

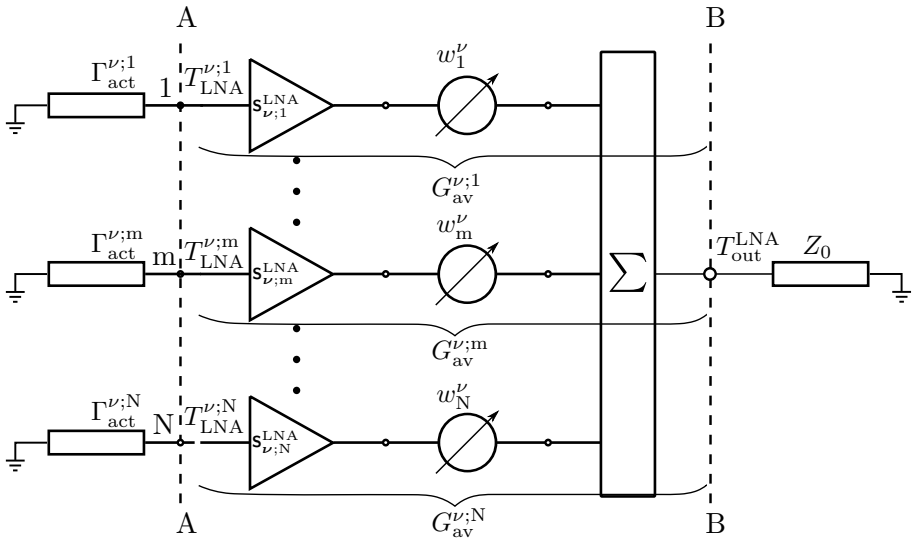

Figure 4.6: Equivalent uncoupled representation of the active multi-mode antenna.

Given that the effective area (4.34) is defined at the antenna port plane $(A-A)$, Fig. 4.6 must be used to derive an expression for the equivalent noise temperature contributed by the receiver referenced to the plane $(A-A)$. The total noise contribution at the output of the beamforming network due to the LNAs $\left(T_{\text{out}}^{\text{LNA}}\right)$ is given by the weighted sum of the uncorrelated noise contributions of each LNA

$$T_{\text{out}}^{\text{LNA}} = \sum_{m=1}^{N} G_{\text{av}}^{\nu;\text{m}} T_{\text{LNA}}^{\nu;\text{m}}, \tag{4.39}$$

where the noise temperature $T_{\text{LNA}}^{\nu;\text{m}}$ of channel or mode m$=1, ..., N$ is referred to the input plane $(A-A)$ and is weighted by the available gain defined from the plane $(A-A)$ to $(B-B)$, i.e.

$$G_{\text{av}}^{\nu;\text{m}} = \frac{1}{N}|S_{21}^{\text{LNA}}|^2 |w_{\text{m}}^\nu|^2 \left(1-|\Gamma_{\text{act}}^{\nu;\text{m}}|^2\right). \tag{4.40}$$

The input referred noise temperature of each channel or mode is obtained using the well-known formula for noisy two-ports

$$T_{\text{LNA}}^{\nu;\text{m}} = T_{\text{min}} + \frac{4R_{\text{n}}^{\nu;\text{m}} T_0}{Z_0^{\nu;\text{m}}} \left[\frac{|\Gamma_{\text{act}}^{\nu;\text{m}} - \Gamma_{\text{opt}}|^2}{|1+\Gamma_{\text{opt}}|^2 \left(1-|\Gamma_{\text{act}}^{\nu;\text{m}}|^2\right)}\right], \tag{4.41}$$

where $R_{\text{n}}^{\nu;\text{m}}$, T_{min}, Γ_{opt} are the noise parameters of each LNA m$=1, ..., N$ for either the SE or multi-mode representation ($\nu =$ SE, MM), and $Z_0^{\nu;\text{m}}$ is the real-valued reference impedance of each channel or mode. Dividing (4.39) with the equivalent available gain of the LNAs yields the equivalent input referred noise of the receiver, i.e.

$$T_{\text{eq}} = \frac{T_{\text{out}}^{\text{LNA}}}{G_{\text{av}}^{\text{eq}}} \tag{4.42}$$

where

$$G_{\text{av}}^{\text{eq}} = \frac{1}{N}\left[\sum_{m=1}^{N} |w_{\text{m}}^\nu|^2 |S_{21}^{\text{LNA}}|^2 \left(1-|\Gamma_{\text{act}}^{\nu;\text{m}}|^2\right)\right], \tag{4.43}$$

and hence, for identical SE LNAs, (4.42) reduces to

$$T_{\text{eq}} = \frac{\sum_{m=1}^{N} T_{\text{LNA}}^{\nu;\text{m}} |w_{\text{m}}^{\nu}|^2 \left(1 - |\Gamma_{\text{act}}^{\nu;\text{m}}|^2\right)}{\sum_{m=1}^{N} |w_{\text{m}}^{\nu}|^2 \left(1 - |\Gamma_{\text{act}}^{\nu;\text{m}}|^2\right)}. \tag{4.44}$$

As expressed in (2.1) sensitivity is defined as the ratio of the effective area (4.34) to the total system noise temperature T_{sys}. In general T_{sys} consists of four predominant contributions: (i) the sky noise, (ii) spill-over noise, (iii) noise due to dissipation loss of the antenna, and (iv) the noise due to the LNAs [45]. As indicated in Fig. 2.1, sky noise is the predominate factor in the system noise temperature at lower frequencies. Low noise contribution from the receiver is therefore less critical at the lower end of the SKA frequency band. Since sky noise contribution in the mid-frequency band of the SKA is much lower, spill-over noise could result in an increase in the system noise temperature when scanning toward the horizon. Given the scope of this chapter, only the receiver noise contribution is taken into account, such that $T_{\text{sys}} = T_{\text{eq}}$, where the input referred noise contribution of the receiver is calculated through (4.44). The receiving sensitivity of the multi-mode active antenna, in both SE and multi-mode representations ($\nu = \text{SE, MM}$), is therefore expressed as

$$\frac{A_{\text{eff}}(\theta,\phi)}{T_{\text{sys}}} = \frac{\lambda^2}{2\eta T_{\text{eq}}} \left[\frac{\left| \sum_{m=1}^{N} w_{\text{m}}^{\nu} \boldsymbol{f}_{\text{m}}^{\nu}(\theta,\phi) \right|^2}{(\mathbf{w}^{\boldsymbol{\nu}})^H \left[\boldsymbol{\mathcal{I}} - \mathbf{S}^{\nu;\text{ant}} \left(\mathbf{S}^{\nu;\text{ant}}\right)^H \right] \mathbf{w}^{\boldsymbol{\nu}}} \right]. \tag{4.45}$$

The expressions in (4.45) defines the sensitivity with the signal and noise response of the active multi-mode antenna referred to the input of the antenna. An equivalent description of the sensitivity, proportional to (4.45), is obtained by considering the Signal-to-Noise Ratio (SNR) at the output port of the active multi-mode receiver.

Receiving model

The following derivation of the SNR of an active multi-mode receiver is based on the exposition detailed in [51, 53, 54]. In [51] the SNR is defined in terms of the signal and noise voltage correlation matrices at the beamformer output. Here, the same procedure is applied to express the SNR in terms of the signal and noise waves propagating through the receiver. Toward this end, consider Fig. 4.7 representing both the SE and multi-mode response ($\nu = \text{SE, MM}$) of the multi-mode receiver, indicating the incident and reflected waves at the antenna port $\mathbf{a}_{\text{S}}^{\boldsymbol{\nu}} = \left[a_{\text{S;1}}^{\nu} \ldots a_{\text{S;N}}^{\nu}\right]^T$, $\mathbf{b}_{\text{S}}^{\boldsymbol{\nu}} = \left[b_{\text{S;1}}^{\nu} \ldots b_{\text{S;N}}^{\nu}\right]^T$, the input of the beamformer $\mathbf{a}_{\text{L}}^{\boldsymbol{\nu}} = \left[a_{\text{L;1}}^{\nu} \ldots a_{\text{L;N}}^{\nu}\right]^T$, $\mathbf{b}_{\text{L}}^{\boldsymbol{\nu}} = \left[b_{\text{L;1}}^{\nu} \ldots b_{\text{L;N}}^{\nu}\right]^T$, as well as the input referred noise waves produced by the LNAs $\mathbf{a}_{\boldsymbol{\eta}}^{\boldsymbol{\nu}} = \left[a_{\eta;1}^{\nu} \ldots a_{\eta;\text{N}}^{\nu}\right]^T$, $\mathbf{b}_{\boldsymbol{\eta}}^{\boldsymbol{\nu}} = \left[b_{\eta;1}^{\nu} \ldots b_{\eta;\text{N}}^{\nu}\right]^T$.

Assuming a noiseless antenna and no external interfering signals, the incident waves at the

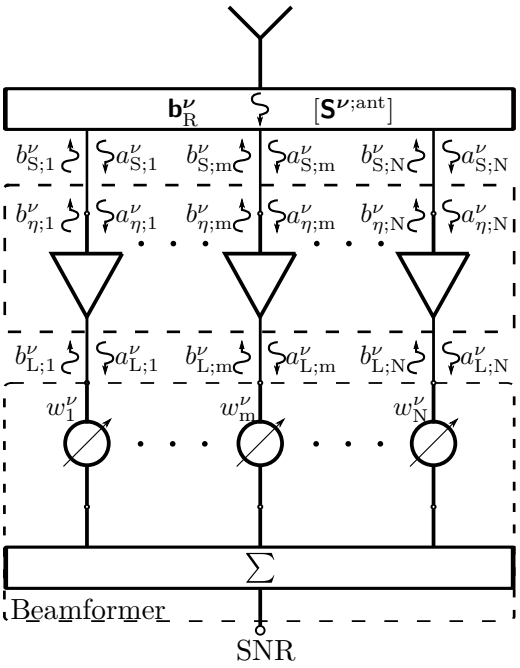

Figure 4.7: Equivalent representation of the active multi-mode antenna showing the incident and reflected signal and noise waves propagating through the receiver.

antenna ports can be expressed as

$$\mathbf{a}^{\nu}_{\mathrm{S}} = \mathbf{b}^{\nu}_{\mathrm{R}} + \mathbf{S}^{\nu;\mathrm{ant}}\mathbf{b}^{\nu}_{\mathrm{S}}, \tag{4.46}$$

where $\mathbf{S}^{\nu;\mathrm{ant}}$ denotes the $[N \times N]$ S-matrix of the antenna corresponding to the SE or multi-mode representation ν, and $\mathbf{b}^{\nu}_{\mathrm{R}}$ the waves induced in each conductor or mode by an incident electromagnetic wave front. Taking the noise contributed by the LNAs into account, the expression in (4.46) expands to [51]

$$\mathbf{a}^{\nu}_{\mathrm{S}} = \mathbf{b}^{\nu}_{\mathrm{R}} + \mathbf{S}^{\nu;\mathrm{ant}}\mathbf{b}^{\nu}_{\mathrm{S}} + \mathbf{S}^{\nu;\mathrm{ant}}\mathbf{b}^{\nu}_{\boldsymbol{\eta}} - \mathbf{a}^{\nu}_{\boldsymbol{\eta}}. \tag{4.47}$$

Given that the reference impedance is selected such that $S^{\mathrm{LNA}}_{11} = 0$, and therefore $\mathbf{b}^{\nu}_{\mathrm{S}} = \mathbf{0}$, (4.47) reduces to

$$\mathbf{a}^{\nu}_{\mathrm{S}} = \mathbf{b}^{\nu}_{\mathrm{R}} + \mathbf{S}^{\nu;\mathrm{ant}}\mathbf{b}^{\nu}_{\boldsymbol{\eta}} - \mathbf{a}^{\nu}_{\boldsymbol{\eta}}. \tag{4.48}$$

For unilateral LNAs matched to the input ports of the beamformer it results that $\mathbf{b}^{\nu}_{\mathrm{L}} = \mathbf{0}$ and the incident wave at the beamformer port m= 1, ..., N equates to

$$a^{\nu}_{\mathrm{L};\mathrm{m}} = S^{\mathrm{LNA}}_{21} a^{\nu}_{\mathrm{S};\mathrm{m}}, \tag{4.49}$$

where S^{LNA}_{21} denotes the gain of the LNAs. For notational ease, unity gain is assumed $\left(S^{\mathrm{LNA}}_{21} = 1\right)$, hence from (4.48)

$$\mathbf{a}^{\nu}_{\mathrm{L}} = \mathbf{b}^{\nu}_{\mathrm{R}} + \mathbf{S}^{\nu;\mathrm{ant}}\mathbf{b}^{\nu}_{\boldsymbol{\eta}} - \mathbf{a}^{\nu}_{\boldsymbol{\eta}}. \tag{4.50}$$

Using (4.50) the wave correlation matrix at the input of the beamformer can be defined as [54]

$$\begin{aligned}\mathbf{R}_{\mathrm{a}} &= \mathbf{a}_{\mathrm{L}}^{\boldsymbol{\nu}} \left(\mathbf{a}_{\mathrm{L}}^{\boldsymbol{\nu}}\right)^{H} \\ &= \mathbf{R}_{\mathrm{sig}} + \mathbf{R}_{\boldsymbol{\eta}},\end{aligned} \tag{4.51}$$

with $\mathbf{R}_{\mathrm{sig}}$ denoting the signal wave correlation matrix

$$\mathbf{R}_{\mathrm{sig}} = \mathbf{b}_{\mathrm{R}}^{\boldsymbol{\nu}} \left(\mathbf{b}_{\mathrm{R}}^{\boldsymbol{\nu}}\right)^{H}, \tag{4.52}$$

and $\mathbf{R}_{\boldsymbol{\eta}}$ the noise wave correlation matrix equating to

$$\begin{aligned}\mathbf{R}_{\boldsymbol{\eta}} &= \left[\mathbf{S}^{\boldsymbol{\nu};\mathrm{ant}}\mathbf{b}_{\boldsymbol{\eta}}^{\boldsymbol{\nu}} - \mathbf{a}_{\boldsymbol{\eta}}^{\boldsymbol{\nu}}\right]\left[\mathbf{S}^{\boldsymbol{\nu};\mathrm{ant}}\mathbf{b}_{\boldsymbol{\eta}}^{\boldsymbol{\nu}} - \mathbf{a}_{\boldsymbol{\eta}}^{\boldsymbol{\nu}}\right]^{H} \\ &= \mathbf{S}^{\boldsymbol{\nu};\mathrm{ant}}\mathbf{b}_{\boldsymbol{\eta}}^{\boldsymbol{\nu}}\left(\mathbf{b}_{\boldsymbol{\eta}}^{\boldsymbol{\nu}}\right)^{H}\left(\mathbf{S}^{\boldsymbol{\nu};\mathrm{ant}}\right)^{H} - \mathbf{S}^{\boldsymbol{\nu};\mathrm{ant}}\mathbf{b}_{\boldsymbol{\eta}}^{\boldsymbol{\nu}}\left(\mathbf{a}_{\boldsymbol{\eta}}^{\boldsymbol{\nu}}\right)^{H} - \mathbf{a}_{\boldsymbol{\eta}}^{\boldsymbol{\nu}}\left(\mathbf{b}_{\boldsymbol{\eta}}^{\boldsymbol{\nu}}\right)^{H}\left(\mathbf{S}^{\boldsymbol{\nu};\mathrm{ant}}\right)^{H} + \mathbf{a}_{\boldsymbol{\eta}}^{\boldsymbol{\nu}}\left(\mathbf{a}_{\boldsymbol{\eta}}^{\boldsymbol{\nu}}\right)^{H}.\end{aligned} \tag{4.53}$$

Defining equivalent noise temperatures for the incident and reflected noise power, as well as the correlation between the incident and reflected noise waves, (4.53) can be written as

$$\mathbf{R}_{\boldsymbol{\eta}} = k_{\mathrm{B}}\Delta f\left[\mathbf{T}_{\boldsymbol{\alpha}} + \mathbf{S}^{\boldsymbol{\nu};\mathrm{ant}}\mathbf{T}_{\boldsymbol{\beta}}\left(\mathbf{S}^{\boldsymbol{\nu};\mathrm{ant}}\right)^{H} - \mathbf{S}^{\boldsymbol{\nu};\mathrm{ant}}\mathbf{T}_{\boldsymbol{\gamma}} - \left(\mathbf{T}_{\boldsymbol{\gamma}}\right)^{H}\left(\mathbf{S}^{\boldsymbol{\nu};\mathrm{ant}}\right)^{H}\right]. \tag{4.54}$$

Since the noise contributed by the LNAs are uncorrelated $\mathbf{T}_{\boldsymbol{\alpha}}$, $\mathbf{T}_{\boldsymbol{\beta}}$, and $\mathbf{T}_{\boldsymbol{\gamma}}$ are diagonal matrices constructed from the auto- and cross correlated noise powers of the respective noise waves of each LNA, i.e.

$$\mathbf{T}_{\boldsymbol{\alpha}} = \frac{1}{k_{\mathrm{B}}\Delta f}\left[\mathbf{a}_{\boldsymbol{\eta}}^{\boldsymbol{\nu}}\left(\mathbf{a}_{\boldsymbol{\eta}}^{\boldsymbol{\nu}}\right)^{H}\right] \tag{4.55a}$$

$$\mathbf{T}_{\boldsymbol{\beta}} = \frac{1}{k_{\mathrm{B}}\Delta f}\left[\mathbf{b}_{\boldsymbol{\eta}}^{\boldsymbol{\nu}}\left(\mathbf{b}_{\boldsymbol{\eta}}^{\boldsymbol{\nu}}\right)^{H}\right] \tag{4.55b}$$

$$\mathbf{T}_{\boldsymbol{\gamma}} = \frac{1}{k_{\mathrm{B}}\Delta f}\left[\mathbf{b}_{\boldsymbol{\eta}}^{\boldsymbol{\nu}}\left(\mathbf{a}_{\boldsymbol{\eta}}^{\boldsymbol{\nu}}\right)^{H}\right] \tag{4.55c}$$

where Δf denotes the noise bandwidth and the diagonal elements of the equivalent noise temperatures in (4.55) are solved from the noise parameters of the SE or multi-mode representations using [55]

$$\begin{aligned}T_{\alpha;\mathrm{mm}} &= \frac{T_0}{|R_0^{\nu;\mathrm{m}}|}\left[R_{\mathrm{n}}^{\nu;\mathrm{m}}\left(1 + |Z_0^{\nu;\mathrm{m}}|^2|Y_{\mathrm{opt}}^{\nu;\mathrm{m}}|^2\right) + R_0^{\nu;\mathrm{m}}\left(F_{\min} - 1\right) - 2R_{\mathrm{n}}^{\nu;\mathrm{m}}\left(R_0^{\nu;\mathrm{m}}G_{\mathrm{opt}}^{\nu;\mathrm{m}} - X_0^{\nu;\mathrm{m}}B_{\mathrm{opt}}^{\nu;\mathrm{m}}\right)\right] \\ T_{\beta;\mathrm{mm}} &= \frac{T_0}{|R_0^{\nu;\mathrm{m}}|}\left[R_{\mathrm{n}}^{\nu;\mathrm{m}}\left(1 + |Z_0^{\nu;\mathrm{m}}|^2|Y_{\mathrm{opt}}^{\nu;\mathrm{m}}|^2\right) - R_0^{\nu;\mathrm{m}}\left(F_{\min} - 1\right) + 2R_{\mathrm{n}}^{\nu;\mathrm{m}}\left(R_0^{\nu;\mathrm{m}}G_{\mathrm{opt}}^{\nu;\mathrm{m}} + X_0^{\nu;\mathrm{m}}B_{\mathrm{opt}}^{\nu;\mathrm{m}}\right)\right] \\ T_{\gamma;\mathrm{mm}} &= \frac{T_0}{|R_0^{\nu;\mathrm{m}}|}\left[R_{\mathrm{n}}^{\nu;\mathrm{m}}\left(1 - |Y_{\mathrm{opt}}^{\nu;\mathrm{m}}|^2\left((R_0^{\nu;\mathrm{m}})^2 - (X_0^{\nu;\mathrm{m}})^2\right)\right) + 2R_{\mathrm{n}}^{\nu;\mathrm{m}}X_0^{\nu;\mathrm{m}}B_{\mathrm{opt}}^{\nu;\mathrm{m}}\right] \\ &\quad + j2T_0R_{\mathrm{n}}^{\nu;\mathrm{m}}\left(B_{\mathrm{opt}}^{\nu;\mathrm{m}} + X_0^{\nu;\mathrm{m}}|Y_{\mathrm{opt}}^{\nu;\mathrm{m}}|^2\right),\end{aligned} \tag{4.56}$$

with T_0 denoting the standard temperature, $F_{\min}$ the minimum noise factor, $Y_{\mathrm{opt}}^{\nu;\mathrm{m}} = G_{\mathrm{opt}}^{\nu;\mathrm{m}} + jB_{\mathrm{opt}}^{\nu;\mathrm{m}}$ the optimum source admittance, and $Z_0^{\nu;\mathrm{m}} = R_0^{\nu;\mathrm{m}} + jX_0^{\nu;\mathrm{m}}$ the complex characteristic

reference impedance. Using the signal and noise correlation matrices defined in (4.52) and (4.54), the SNR at the output port of the beamformer can be defined as the ratio of the weighted signal and noise powers, i.e. [51]

$$\mathrm{SNR} = \frac{(\mathbf{w}^{\boldsymbol{\nu}})^H \mathbf{R}_{\mathrm{sig}} \mathbf{w}^{\boldsymbol{\nu}}}{(\mathbf{w}^{\boldsymbol{\nu}})^H \mathbf{R}_{\boldsymbol{\eta}} \mathbf{w}^{\boldsymbol{\nu}}}. \tag{4.57}$$

Finally, for an incident electromagnetic wave front with signal flux density $S_{\mathrm{f}}\,(\mathrm{W/m^2})$ the sensitivity can be expressed in terms of the SNR [56, 57], i.e.

$$\frac{A_{\mathrm{eff}}\,(\theta,\phi)}{T_{\mathrm{sys}}} = \frac{k_{\mathrm{B}}\Delta f}{S_{\mathrm{f}}}\,[\mathrm{SNR}]\,, \tag{4.58}$$

where k_{B} denotes Boltzmann's constant and Δf the noise bandwidth. In Sec. 4.2.2 this expression for the SNR (4.57) is used to solve the beamforming weights that result in maximum sensitivity over the FoV coverage.

4.1.3 Polarimeter model

As for the derivation of sensitivity, the multi-mode noise and antenna models can be used to derive a polarimeter model in terms of the multi-mode excitations. This section introduces the equivalent receiver model through which the polarimetric performance of an active multi-mode antenna can be assessed. The analysis is based on the polarimeter model for single-mode array antennas as detailed in [46, 58]. Analogous to the equivalent multi-mode representation in Fig. 4.1(b) the multi-mode polarimeter model shown in Fig. 4.8 depicts the multi-mode antenna as an N-element phased array where each element represents one of the N orthogonal excitation modes through which the multi-mode antenna is excited. To define the polarimetric performance of the multi-mode polarimeter, the polarimetric response is modelled using the Jones matrix formulation [59].

Jones matrix formulation

As indicated in Fig. 4.8 the antenna is assumed to be illuminated by an arbitrarily polarised plane wave electric field

$$\boldsymbol{E}_{\mathrm{inc}}\,(\boldsymbol{r}) = E_{\mathrm{u}}\,(\boldsymbol{r})\,\hat{\boldsymbol{u}} + E_{\mathrm{v}}\,(\boldsymbol{r})\,\hat{\boldsymbol{v}}, \tag{4.59}$$

where E_{u} and E_{v} are the two orthogonal field components of the incident plane-wave corresponding to the coordinate system defined by the unit vectors $\hat{\boldsymbol{u}}$ and $\hat{\boldsymbol{v}}$. For a dual-polarised polarimeter, the Jones matrix constitutes a transfer function relating the two orthogonal components of an incident electric field to the voltages induced at the two output ports of the polarimeter $\mathbf{v}^{\mathrm{MM}} = [v_1\, v_2]^T$, i.e.

$$\begin{bmatrix} v_1 \\ v_2 \end{bmatrix} = \begin{bmatrix} J_{11} & J_{12} \\ J_{21} & J_{22} \end{bmatrix} \begin{bmatrix} E_{\mathrm{u}} \\ E_{\mathrm{v}} \end{bmatrix} = \mathbf{J}\boldsymbol{E}_{\mathrm{inc}}, \tag{4.60}$$

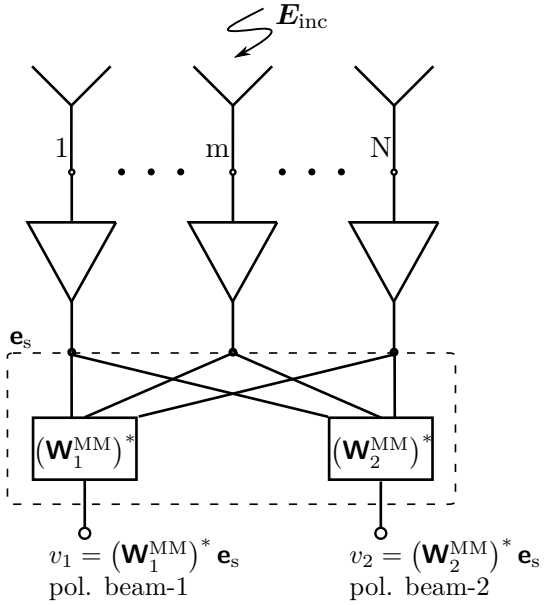

Figure 4.8: Polarimeter model of an active multi-mode antenna showing the output signals of the two polarimeter beams (pol. beam-1 and pol. beam-2).

where the output voltages of the polarimeter $\mathbf{v}^{\text{MM}}$ are obtained by combining the voltages at the beamformer input $\mathbf{e}_{\text{s}}$ using the two $[N \times 1]$ beamformer weight sets $\mathbf{w}_1^{\text{MM}}$ and $\mathbf{w}_2^{\text{MM}}$. The elements of the Jones matrix are derived by considering the voltage response of the polarimeter, $\mathbf{e}_{\text{u}}$ and $\mathbf{e}_{\text{v}}$, corresponding to a $\hat{\boldsymbol{u}}$- and $\hat{\boldsymbol{v}}$- polarised incident electric field respectively. For an arbitrarily polarised incident field the signal response of the polarimeter ($\mathbf{e}_{\text{s}}$) can be expressed in terms of $\mathbf{e}_{\text{u}}$ and $\mathbf{e}_{\text{v}}$ [58]. That is

$$\mathbf{e}_{\text{s}} = E_{\text{u}}\mathbf{e}_{\text{u}} + E_{\text{v}}\mathbf{e}_{\text{v}}, \tag{4.61}$$

for which the two beam output voltages equate to

$$\begin{bmatrix} v_1 \\ v_2 \end{bmatrix} = \begin{bmatrix} \mathbf{w}_1^{\text{MM}\,H}\mathbf{e}_{\text{s}} \\ \mathbf{w}_2^{\text{MM}\,H}\mathbf{e}_{\text{s}} \end{bmatrix}. \tag{4.62}$$

Substituting (4.61) into (4.62) the beam output voltages can be related to the components of the incident electric fields through

$$\begin{aligned} \begin{bmatrix} v_1 \\ v_2 \end{bmatrix} &= \begin{bmatrix} \mathbf{w}_1^{\text{MM}\,H}\left(E_{\text{u}}\mathbf{e}_{\text{u}} + E_{\text{v}}\mathbf{e}_{\text{v}}\right) \\ \mathbf{w}_2^{\text{MM}\,H}\left(E_{\text{u}}\mathbf{e}_{\text{u}} + E_{\text{v}}\mathbf{e}_{\text{v}}\right) \end{bmatrix} \\ &= \begin{bmatrix} \mathbf{w}_1^{\text{MM}\,H}\mathbf{e}_{\text{u}} & \mathbf{w}_1^{\text{MM}\,H}\mathbf{e}_{\text{v}} \\ \mathbf{w}_2^{\text{MM}\,H}\mathbf{e}_{\text{u}} & \mathbf{w}_2^{\text{MM}\,H}\mathbf{e}_{\text{v}} \end{bmatrix} \begin{bmatrix} E_{\text{u}} \\ E_{\text{v}} \end{bmatrix}, \end{aligned} \tag{4.63}$$

and hence, it follows that the Jones matrix of the multi-mode polarimeter equates to

$$\mathbf{J} = \begin{bmatrix} \mathbf{w}_1^{\text{MM}\,H}\mathbf{e}_{\text{u}} & \mathbf{w}_1^{\text{MM}\,H}\mathbf{e}_{\text{v}} \\ \mathbf{w}_2^{\text{MM}\,H}\mathbf{e}_{\text{u}} & \mathbf{w}_2^{\text{MM}\,H}\mathbf{e}_{\text{v}} \end{bmatrix}. \tag{4.64}$$

Intrinsic cross-polarisation ratio

Conventionally the polarisation performance of an antenna can be analysed through two standard IEEE definitions, i.e. Cross-Polarisation Discrimination (XPD) and Cross-Polarisation Isolation (XPI) [60], defined in terms of the elements of the Jones matrix as

$$\begin{aligned} \mathrm{XPD_u} &= \frac{|J_{1\mathrm{u}}|^2}{|J_{2\mathrm{u}}|^2} \qquad \mathrm{XPD_v} = \frac{|J_{1\mathrm{v}}|^2}{|J_{2\mathrm{v}}|^2} \\ \mathrm{XPI_1} &= \frac{|J_{1\mathrm{u}}|^2}{|J_{1\mathrm{v}}|^2} \qquad \mathrm{XPI_2} = \frac{|J_{2\mathrm{u}}|^2}{|J_{2\mathrm{v}}|^2}. \end{aligned} \tag{4.65}$$

These Cross-Polarisation Ratios (XPRs) have been defined to assess the performance of dual-polarised antennas used in communication links and therefore assume prior knowledge of the alignment of the co- and cross-polar components with respect to a know transmitter. This dependence on the reference coordinate system may result in substantial changes in the XPR values when adjustments are made to the reference coordinate system [61]. In radio astronomy applications no unique selection for a reference coordinate system exists, even more so for large antenna arrays where multiple beams can be electronically steered over the FoV coverage of the array. The polarimetric performance of the active multi-mode antenna is therefore characterised using a polarimetric figure-of-merit that is independent of the chosen coordinate system: the Intrinsic Cross-Polarisation Ratio (IXR) [61].

In defining the IXR the reference coordinate systems of both the polarimeter and the incident electric field are rotated such that a diagonal Jones matrix results. This diagonalisation is achieved by appling the singular value decomposition theorem to the Jones matrix in (4.64), from which it follows that $\mathbf{J}$ can be expressed as the matrix product of a diagonal matrix containing the largest and smallest singular values of $\mathbf{J}$ ($\sigma_{\max}$, $\sigma_{\min}$) and two unitary matrices $\mathbf{Q}$ and $\mathbf{U}$, i.e.

$$\mathbf{J} = \mathbf{Q} \begin{bmatrix} \sigma_{\max} & 0 \\ 0 & \sigma_{\min} \end{bmatrix} \mathbf{U}^H. \tag{4.66}$$

Applying a 45° rotation to the diagonal matrix of singular values using the transformation matrix

$$\mathbf{R}_{45} = \frac{1}{\sqrt{2}} \begin{bmatrix} 1 & 1 \\ 1 & -1 \end{bmatrix}, \tag{4.67}$$

the following relation results

$$\mathbf{J} = \mathbf{Q}\mathbf{R}_{45}\mathbf{J'}{\mathbf{R}_{45}}^H\mathbf{U}^H, \tag{4.68}$$

where $\mathbf{J'}$ is of the form

$$\mathbf{J'} = \mathrm{c} \begin{bmatrix} 1 & \mathrm{d} \\ \mathrm{d} & 1 \end{bmatrix} \tag{4.69}$$

and the constants (c, d) are defined in terms of the singular values of $\mathbf{J}$, i.e.

$$\mathrm{c} = \frac{\sigma_{\max} + \sigma_{\min}}{2}, \qquad \mathrm{d} = \frac{\sigma_{\max} - \sigma_{\min}}{\sigma_{\max} + \sigma_{\min}}. \tag{4.70}$$

For the polarimeter alignment resulting in (4.69) the XPRs equate to

$$\mathrm{XPD_u} = \mathrm{XPI_1} = \mathrm{IXR}, \tag{4.71}$$

with

$$\mathrm{IXR} = \frac{1}{\mathrm{d}^2}. \tag{4.72}$$

Hence, the IXR is defined solely by the invariant singular values of the Jones matrix of the multi-mode polarimeter ($\mathbf{J}$), making the IXR a polarimetric figure-of-merit that is independent of the respective orientation of the reference coordinate systems. In Sec. 4.2.3 the polarimetric beamforming weight sets $\mathbf{w}_1^{\mathrm{MM}}$ and $\mathbf{w}_2^{\mathrm{MM}}$ are derived to ensure optimal polarisation performance whilst retaining minimum receiver noise contribution.

4.2 Beamforming Algorithms

Given the similarity between the receiver model of an active multi-mode antenna and the equivalent model for conventional single-mode phased antenna arrays, the same beamforming strategies normally applied to solve the optimum weights for single-mode phased array antennas can be applied to solve the weights for each of the orthogonal TEM excitation modes of the multi-mode antenna. These beamforming strategies are covered extensively in recent literature detailing the performance of antenna arrays for radio astronomy applications [46, 62, 58, 63]. In Sec. 4.2.1 to Sec. 4.2.3, three beamforming strategies implemented to solve the complex beamforming weights that result in maximum gain, SNR, and optimal polarimetric performance are summarised. During each exposition, the multi-mode operation of the multi-mode antenna is considered and for notational simplicity the MM notation is omitted from all parameters.

4.2.1 Maximum gain

To obtain the complex beamforming weights that result in maximum gain over the FoV coverage, consider the equivalent multi-mode network representation of the active multi-mode receiver depicted in Fig. 4.1(b). It follows from (4.31) to (4.33) that the gain of the multi-mode antenna at each scan angle can be expressed as

$$G(\theta,\phi) = \frac{2\pi}{\eta}\left[\frac{\left|\sum_{m=1}^{N} w_{\mathrm{m}}\boldsymbol{f}_{\mathrm{m}}(\theta,\phi)\right|^2}{(\mathbf{w})^H\left[\boldsymbol{\mathcal{I}} - \mathbf{S}^{\mathrm{ant}}\left(\mathbf{S}^{\mathrm{ant}}\right)^H\right]\mathbf{w}}\right], \tag{4.73}$$

where $\mathbf{w}$ is an $[N \times 1]$ vector containing the beamforming weights corresponding to each orthogonal excitation mode of the multi-mode antenna, $\mathbf{S}^{\mathrm{ant}}$ is the equivalent multi-mode S-matrix of the antenna, and $\boldsymbol{f}_{\mathrm{m}}(\theta,\phi)$ denotes the electric field vector radiated by the EEP of each mode

$m = 1, \ldots \mathrm{N}$ defined in the far-field in a spherical coordinate system, i.e.

$$\boldsymbol{f}_{\mathrm{m}}(\theta,\phi) = f_{\mathrm{m}}^{\theta}(\theta,\phi)\,\hat{\boldsymbol{\theta}} + f_{\mathrm{m}}^{\phi}(\theta,\phi)\,\hat{\boldsymbol{\phi}}. \tag{4.74}$$

For notational ease the components of the EEPs at each scan angle are structured in an $[N \times 2]$ matrix of the form

$$\boldsymbol{F} = \begin{bmatrix} f_1^{\theta}(\theta,\phi) & f_1^{\phi}(\theta,\phi) \\ \vdots & \vdots \\ f_{\mathrm{m}}^{\theta}(\theta,\phi) & f_{\mathrm{m}}^{\phi}(\theta,\phi) \\ \vdots & \vdots \\ f_{\mathrm{N}}^{\theta}(\theta,\phi) & f_{\mathrm{N}}^{\phi}(\theta,\phi) \end{bmatrix}. \tag{4.75}$$

Using (4.75) the total radiation intensity (4.32) can be simplified to

$$\begin{aligned} U_{\mathrm{rad}} &= \frac{1}{2\eta}\left[\left(\mathbf{w}^T\boldsymbol{F}\right)\left(\mathbf{w}^T\boldsymbol{F}\right)^H\right] \\ &= \frac{1}{2\eta}\left[\mathbf{w}^T\boldsymbol{F}\boldsymbol{F}^H\mathbf{w}^*\right], \end{aligned} \tag{4.76}$$

and hence the expression for the gain (4.73) can be written as

$$G(\theta,\phi) = \frac{2\pi}{\eta}\left[\frac{\mathbf{w}^T\boldsymbol{F}\boldsymbol{F}^H\mathbf{w}^*}{\mathbf{w}^T\mathbf{B}\mathbf{w}^*}\right], \tag{4.77}$$

with $\mathbf{B} = \left[\boldsymbol{\mathcal{I}} - \mathbf{S}^{\mathrm{ant}}\left(\mathbf{S}^{\mathrm{ant}}\right)^H\right]$.

The weight values that result in maximum gain at each scan angle can therefore be solved by equating the partial derivative of (4.77) with respect to $\mathbf{w}^T$, to zero. That is,

$$\frac{\partial G(\theta,\phi)}{\partial \mathbf{w}^T} = \frac{\mathbf{w}^T\mathbf{B}\mathbf{w}^*\boldsymbol{F}\boldsymbol{F}^H\mathbf{w}^* - \mathbf{w}^T\boldsymbol{F}\boldsymbol{F}^H\mathbf{w}^*\mathbf{B}\mathbf{w}^*}{\left[\mathbf{w}^T\mathbf{B}\mathbf{w}^*\right]^2} = 0$$

$$\begin{aligned} \therefore \quad \mathbf{w}^T\mathbf{B}\mathbf{w}^*\boldsymbol{F}\boldsymbol{F}^H\mathbf{w}^* &= \mathbf{w}^T\boldsymbol{F}\boldsymbol{F}^H\mathbf{w}^*\mathbf{B}\mathbf{w}^* \\ \boldsymbol{F}\boldsymbol{F}^H\mathbf{w}^* &= \left[\frac{\mathbf{w}^T\boldsymbol{F}\boldsymbol{F}^H\mathbf{w}^*}{\mathbf{w}^T\mathbf{B}\mathbf{w}^*}\right]\mathbf{B}\mathbf{w}^* \\ \boldsymbol{F}\boldsymbol{F}^H\mathbf{w}^* &= \frac{\eta}{2\pi}\left[G(\theta,\phi)\,\mathbf{B}\mathbf{w}^*\right] \end{aligned} \tag{4.78}$$

Since $\left[\boldsymbol{F}\boldsymbol{F}^H\right]$ and $\mathbf{B}$ are both $[N \times N]$ matrices, the final expression in (4.78) can be identified as a generalised eigenvalue problem of the form

$$\mathbf{A}\mathbf{v} = \lambda\mathbf{D}\mathbf{v}, \tag{4.79}$$

where $\mathbf{A}$ and $\mathbf{D}$ are square $[N \times N]$ matrices, λ denotes the scalar eigenvalue and $\mathbf{v}$ the corresponding $[N \times 1]$ non-zero eigenvector satisfying the expression in (4.79). The complex beamforming weights resulting in maximum gain at each scan angle can therefore be solved as the conjugate of the eigenvector corresponding to the largest eigenvalue of (4.78).

4.2.2 Maximum signal-to-noise ratio

The complex beamforming weights for each of the multi-mode excitations that result in maximum SNR (or sensitivity) over the FoV coverage can be obtained through (4.57). Given the linearity between the radiated far-fields and the excitation applied to the port of the antenna, it follows from reciprocity that the signals induced at the antenna ports ($\mathbf{b}_{\mathrm{R}}$) by an incident electromagnetic wave front are proportional to the radiated fields at each angle of incidence. Ignoring the proportionality constants in obtaining the beamforming weight values, the signal correlation matrix $\mathbf{R}_{\mathrm{sig}}$ in (4.57) can therefore be expressed in terms of the EEPs of each excitation mode, i.e.

$$\mathbf{R}_{\mathrm{sig}} = \boldsymbol{F}\boldsymbol{F}^{H}, \tag{4.80}$$

with $\boldsymbol{F}$ an $[N \times 2]$ matrix containing the field components of each EEP as defined in (4.75) for each angle of incidence. At the output of the beamformer, the SNR can then be written as

$$\mathrm{SNR} = \frac{\mathbf{w}^{T}\boldsymbol{F}\boldsymbol{F}^{H}\mathbf{w}^{*}}{\mathbf{w}^{T}\mathbf{R}_{\boldsymbol{\eta}}\mathbf{w}^{*}}, \tag{4.81}$$

with $\mathbf{R}_{\boldsymbol{\eta}}$ the noise correlation matrix defined in (4.54).

Equating the partial derivative of (4.81) with respect to $\mathbf{w}^{T}$, to zero it can be shown that

$$\boldsymbol{F}\boldsymbol{F}^{H}\mathbf{w}^{*} = (\mathrm{SNR})\,\mathbf{R}_{\boldsymbol{\eta}}\mathbf{w}^{*}. \tag{4.82}$$

The expression in (4.82) can once again be identified as a generalised eigenvalue problem from which it follows that the complex beamforming weight values that result in maximum SNR at each angle of incidence is solved as the eigenvector corresponding to the largest eigenvalue of the expression in (4.82). Applying these weight values to (4.45) at each angle, the maximum sensitivity of the active multi-mode antenna can be solved over the FoV coverage.

4.2.3 Optimal-polarisation minimum-noise

In Sec. 4.2.2 the beamforming weights maximising the sensitivity in terms of the total field intensity are solved. Following from Sec. 4.1.3, two sets of beamforming weights – each corresponding to one of the orthogonal incident field components – are required to assess, and eventually calibrate, the polarimetric response of the multi-mode antenna. In this section beamforming weights are solved to ensure optimal polarimetric performance while retaining minimum noise contribution from the receiver. An extensive treatment of the beamforming strategy introduced here can be found in [46].

To ensure minimum noise contribution from the receiver, the beamforming weight sets $\{\mathbf{w}_1, \mathbf{w}_2\}$ are first solved to maximise the SNR of the multi-mode polarimeter for a $\hat{\boldsymbol{u}}$- and $\hat{\boldsymbol{v}}$-polarised incident field, respectively. For a completely polarised incident field, it can be shown that the

weights resulting in maximum SNR equate to [63]

$$\mathbf{w}_{\text{MaxSNR}} = [\mathbf{R}_{\boldsymbol{\eta}}]^{-1}\,\mathbf{e}, \tag{4.83}$$

where $\mathbf{R}_{\boldsymbol{\eta}}$ denotes the noise correlation matrix (4.54) of the receiver, and $\mathbf{e}$ the signal induced at the antenna port by the polarised incident field. Concatenating the two beamforming weight sets into the matrix $\mathbf{W}_{\text{SNR}} = [\mathbf{w}_1\,\mathbf{w}_2]$, the expression in (4.83) can be applied to solve the polarimetric beam pair weights to maximise the SNR, i.e.

$$\mathbf{W}_{\text{SNR}} = [\mathbf{R}_{\boldsymbol{\eta}}]^{-1}\,\mathbf{E}, \tag{4.84}$$

with $\mathbf{E} = [\mathbf{e}_{\text{u}}\,\mathbf{e}_{\text{v}}]$.

To achieve optimal polarisation performance the polarimetric beam pair weights should ideally result in a Jones matrix that is equal to the identity matrix. In [46] it is shown that polarimetric correction can be applied to the maximum SNR weights $\mathbf{W}_{\text{SNR}}$ resulting in an identity Jones matrix over the entire FoV coverage, with the sensitivity bounded by the same values achieved before polarimetric correction. This solution for the Optimal-Polarisation Minimum-Noise (OPMN) beamforming weight set is obtained through

$$\mathbf{W}_{\text{OPMN}} = [\mathbf{R}_{\boldsymbol{\eta}}]^{-1}\,\mathbf{E}\left(\mathbf{E}^{H}\,[\mathbf{R}_{\boldsymbol{\eta}}]^{-1}\,\mathbf{E}\right)^{-1}. \tag{4.85}$$

From the expression for the Jones matrix of the polarimeter in (4.64), it follows that the Jones matrix for the maximum SNR beam pair weights can be written as

$$\mathbf{J}_{\text{SNR}} = [\mathbf{W}_{\text{SNR}}]^{H}\,\mathbf{E}. \tag{4.86}$$

Applying (4.84) and (4.86) to (4.85) the expression for the OPMN beamforming weights reduces to

$$\mathbf{W}_{\text{OPMN}} = \mathbf{W}_{\text{SNR}}\left[\mathbf{J}_{\text{SNR}}{}^{H}\right]^{-1}. \tag{4.87}$$

Finally, solving the Jones matrix for the OPMN weights defined in (4.87) it can readily be shown that an identity matrix results, i.e.

$$\begin{aligned}\mathbf{J}_{\text{OPMN}} &= [\mathbf{W}_{\text{OPMN}}]^{H}\,\mathbf{E}\\ &= [\mathbf{J}_{\text{SNR}}]^{-1}\,[\mathbf{W}_{\text{SNR}}]^{H}\,\mathbf{E}\\ &= [\mathbf{J}_{\text{SNR}}]^{-1}\,\mathbf{J}_{\text{SNR}} = \boldsymbol{\mathcal{I}}.\end{aligned} \tag{4.88}$$

In Sec. 4.4 the polarimetric beam pair SNR realised for the conical quad-mode antenna design by the maximum SNR weight set $\mathbf{W}_{\text{SNR}}$ and the polarimetrically calibrated equivalent weights $\mathbf{W}_{\text{OPMN}}$ are compared, showing that polarimetric calibration can result in a reduction in the SNR at scan angles with poor polarisation performance before correction.

The multi-mode characteristics of the antenna elements presented in this work allow the designer to combine different radiation patterns by appropriate weighting and summing of the various

modes. Using the derived multi-mode noise, sensitivity and polarimeter models of Sec. 4.1, the following two sections show how standard array beamforming techniques can be applied to the proposed multi-mode antenna element. It is shown that improved sensitivity, gain over FoV, and polarimetric performance can be obtained in this way. Sections 4.3 and 4.4 therefore constitutes the final evaluation of the multi-mode antennas presented in the preceding sections of this work.

4.3 Active Dual-Mode Antenna

This section presents the performance of an active dual-mode antenna and applies the beamforming algorithms introduced in Sec. 4.2 to illustrate the improved FoV coverage achieved by utilising both differential- and common-mode excitations. The active dual-mode antenna is modelled using the dual-mode antenna design presented in Sec. 3.1.3 – shown again in Fig. 4.9 for ease of reading – placed over an infinite ground plane with two SE LNAs connected to each of the SE ports and their outputs connected to a beamformer as depicted in Fig. 4.1(a).

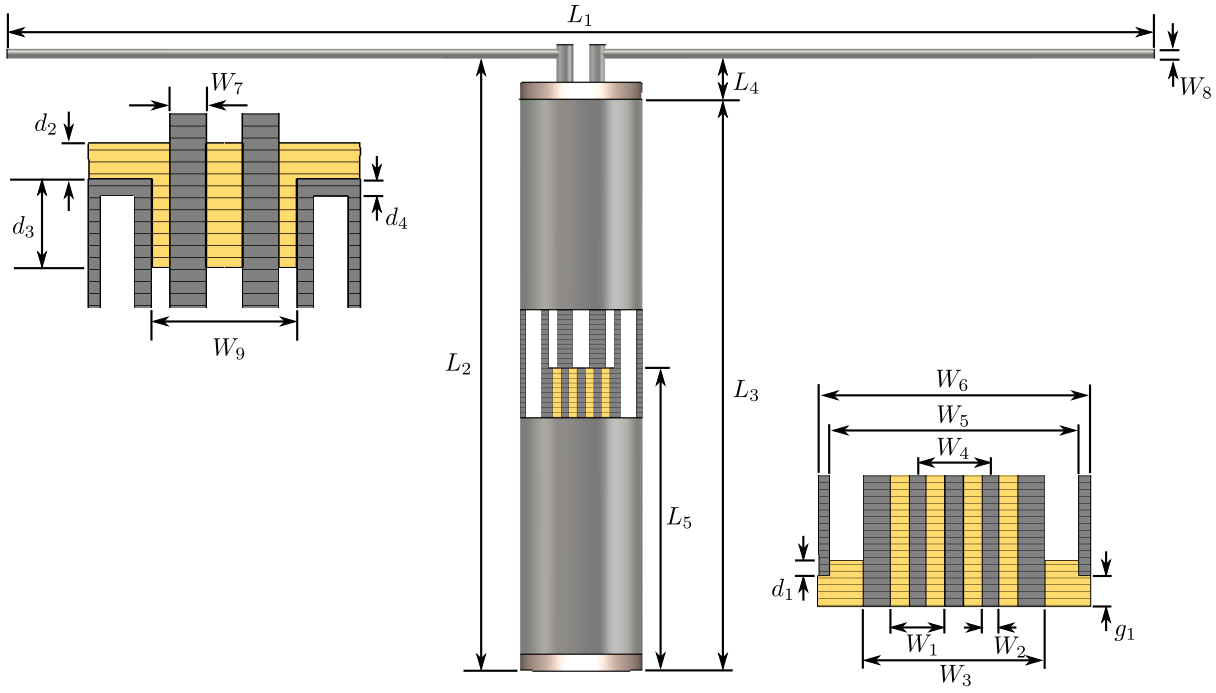

Figure 4.9: Cylindrical dual-mode antenna design with cut planes at the bottom, middle (semi-rigid coaxial to air-core twinaxial transition) and top of the antenna feed.

Throughout the analysis the mixed differential- and common-mode response of the dual-mode antenna, simulated in CST Microwave Studio at 1 GHz with an infinite ground plane, will be considered. The simulated far-field patterns of the antenna are denoted as $\boldsymbol{f}_{1/2}^{\mathrm{MM}}$ – with 1/2 representing the differential/common-mode response – and the corresponding mixed-mode S-matrix (3.14) denoted as $\mathbf{S}^{\mathrm{MM;ant}}$. Furthermore, the SE LNAs are considered unilateral, identical and isolated and with signal and noise response as summarised by the S- and noise parameters

in Table 4.1. As indicated in the table, the SE LNAs are assumed to be noise matched to the passive differential-mode input reflection coefficient $\left(S_{11}^{\mathrm{MM;ant}}\right)$ of the dual-mode antenna.

Table 4.1: Single-ended LNA noise parameters and S-parameters.

Noise parameters	S-parameters
$T_{\mathrm{min}}^{\mathrm{SE}} = 37$ K	$S_{11} = S_{22} = 0$
$R_{\mathrm{n}}^{\mathrm{SE}} = 3\,\Omega$	$S_{12} = 0$
$\Gamma_{\mathrm{opt}}^{\mathrm{SE}} = S_{11}^{\mathrm{MM;ant}}$	$S_{21} = 1$

Using the voltage and current coefficient matrices defined in (3.39) and (3.40), the signal and noise response of the LNAs can be transformed into the equivalent mixed differential- and common-mode response through (4.3) and equation set (4.29). Hence, the active dual-mode antenna can be represented by the equivalent multi-mode representation illustrated in Fig. 4.1(b), with $N = 2$.

4.3.1 Maximum gain

By expressing the gain of the active dual-mode antenna as in (4.77), the eigenvalue problem is solved to obtain the differential- and common-mode weights $\{w_1^{\mathrm{MM}}, w_2^{\mathrm{MM}}\}$ that result in maximum gain at each scan angle. The graph in Fig. 4.10 compares the weighted multi-mode (MM) gain to the gain achieved by a purely differential excitation in the two principal planes at 1 GHz, with the calculated weights shown in Fig. 4.11.

Figure 4.10 clearly illustrates the improved FoV coverage achieved by the dual-mode antenna when compared with the purely differential excitation. Through the added use of common-mode excitation a variation in gain of less than 3 dB is achieved in the E-plane over the scan range from $-90°$ to $90°$, with the gain seen to vary with approximately 4 dB over the same scan range in the H-plane. Note that the sharp junction observed at $65°$ in the H-plane can be ascribed to the fact that the differential- and common-mode excitations radiate orthogonal linearly polarised field components in the H-plane and therefore cannot be summed. In comparison, the gain of the purely differential antenna is seen to fall below zero at scan angles larger $50°$ from zenith in the E-plane, and at approximately $70°$ from zenith in the H-plane. Since low noise contribution is essential over the entire FoV coverage, the maximum sensitivity of the active dual-mode antenna is presented in the following section.

4.3.2 Maximum sensitivity

As shown in Sec. 4.1.2, the beamforming weights resulting in maximum sensitivity over the FoV coverage are obtained by solving the eigenvalue problem derived from the expression for the SNR of the active dual-mode antenna. These weights are therefore obtained by expressing the SNR in terms of the simulated differential- and common-mode far-fields as in (4.81) with

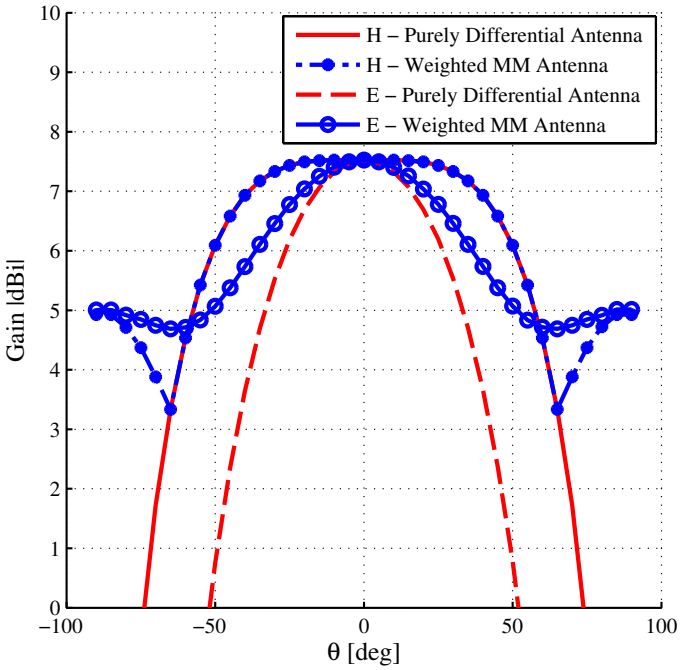

Figure 4.10: Weighted multi-mode gain of the dual-mode antenna compared to the gain achieved by a purely differential excitation in both the E- and H-planes.

the noise correlation matrix defined in terms of the equivalent differential- and common-mode noise parameters, solved through (4.29). Solving the differential- and common-mode weights for maximum SNR at each scan angle, the corresponding gain of the dual-mode active antenna can once again be obtained through (4.77). The graphs in Fig. 4.11 compare the normalised differential- and common-mode weights solved for maximum gain and SNR in both principal planes.

As noted in Fig. 4.11(a) the weights realised by the maximum SNR beamformer in the E-plane are slightly different to the weights solved for the maximum gain beamformer. This difference is ascribed to the fact that the maximum SNR weights take noise mismatch into account and therefore result in a lower noise contribution in the E-plane as compared to the maximum gain beamformer weights. To gain a better understanding of these weight values solved by the two beamforming algorithms, consider the graphs in Fig. 4.12 showing the gain of the differential- and common-common mode EEPs as well as the gain realised through the maximum gain and SNR beamformers, in the two principal planes.

Despite the differences between the weight values solved by the maximum gain and SNR beamformers, both are seen to result in the same weighted gain in the E- and H-planes. Considering only the E-plane gains in Fig. 4.12(a), it is noted that the weighted gain is larger than both the differential- and common-mode EEPs for the scan range between $\pm 75°$ and $\pm 10°$. This is due to the fact that the differential- and common-mode excitations radiate co-polarised fields in the E-plane. In the H-plane however, the fields radiated by the differential- and common-mode excitations – i.e. the dipole and monopole elements – are orthogonal to one another, therefore the

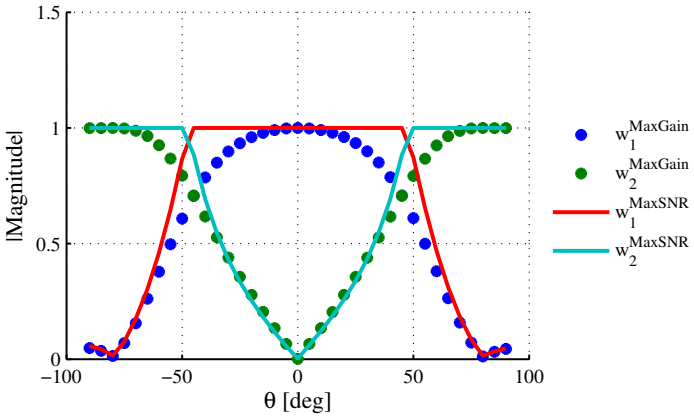

(a)

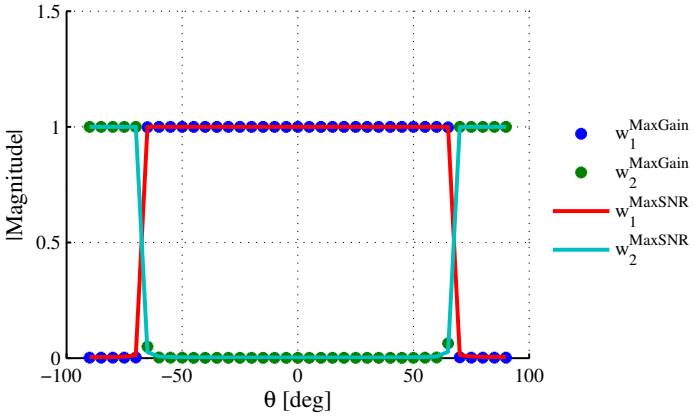

(b)

Figure 4.11: Normalised beamforming weight values for maximum gain and SNR in the (a) *E*-plane and (b) *H*-plane.

respective weight values are seen to be a maximum at the scan angles where each EEP is dominant [c.f. Fig. 4.11(b)] and the corresponding maximum gain equals the gain of the respective differential- or common-mode excitation over the same scan range as indicated in Fig. 4.12(b).

To illustrate the improved sensitivity over the FoV coverage by allowing for combinations of differential- and common-mode excitations, the noise contribution and sensitivity of the active dual-mode antenna are compared to the corresponding values realised by a purely differential excitation. Given the linear relation between the effective area (4.30) and the gain of the antenna, the active dual-mode antenna achieves the same improvement in effective area over the FoV coverage as illustrated for the gain in Fig. 4.10. Since this increase in effective area is maximized by applying complex-valued beamforming weights to each of the two excitation modes, the equivalent noise contribution of the active dual-mode antenna should be computed using the active reflection coefficient as discussed in Sec. 4.1.2, rather than the passive reflection coefficient considered for a purely differential excitation. Using (4.44), defined in terms of the differential- and common-mode active reflection coefficients, the noise contributed to the receiver noise temperature due to the weighted differential- and common-mode excitations is shown for

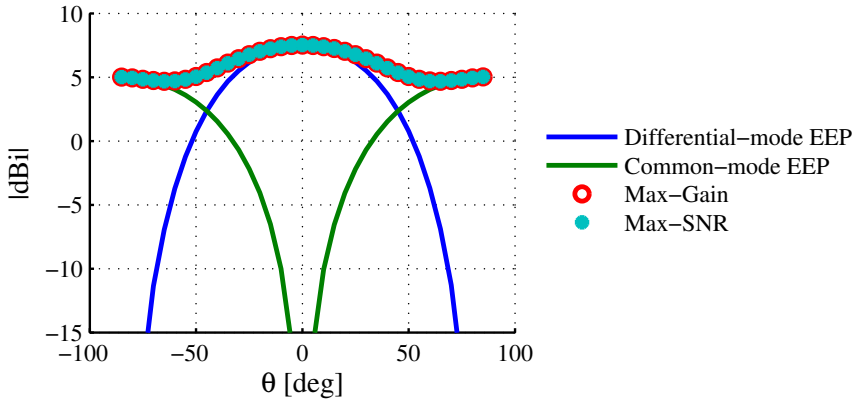

(a)

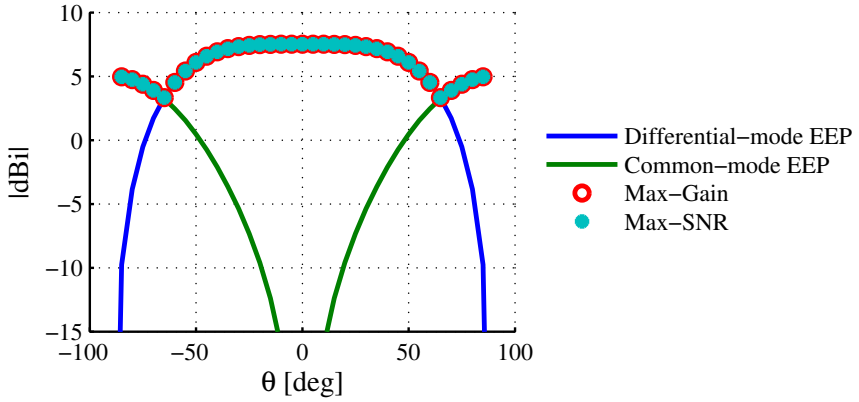

(b)

Figure 4.12: Gain of active dual-mode antenna: EEPs, maximum gain beamformer, and maximum SNR beamformer in the (a) E-plane and (b) H-plane.

both the E- and the H-planes in Fig. 4.13.

Figure 4.13 indicates that the equivalent noise contributed by the purely differential receiver remains constant at the minimum noise temperature of the SE LNA listed in Table 4.1. This is to be expected given that the optimum source reflection coefficient of the LNA equals the passive differential reflection coefficient of the dual-mode antenna. For the mixed differential- and common-mode noise contribution – denoted as (MM) – first consider the E-plane noise contribution in Fig. 4.13. The weighted gain of the active dual-mode antenna in Fig. 4.12(a) is seen to be almost equal to a purely differential-mode excitation for scan angles of $0° \leq \theta_{\text{scan}} \leq 20°$ from zenith. As indicated in Fig. 4.11(a) the differential-mode weights are found to be significantly more dominant than the common-mode weights at these scan angles, resulting in an active differential reflection coefficient close to the passive reflection coefficient of the antenna. Together with low common-mode weight values, this results in the dual-mode receiver being noise matched in the E-plane at $0° \leq \theta_{\text{scan}} \leq 20°$ from zenith. For $20° \leq \theta_{\text{scan}} \leq 50°$ from zenith, the weighted gain is seen to be greater than that of the purely differential receiver. This increase in gain is due to the addition of common-mode propagation realised through an

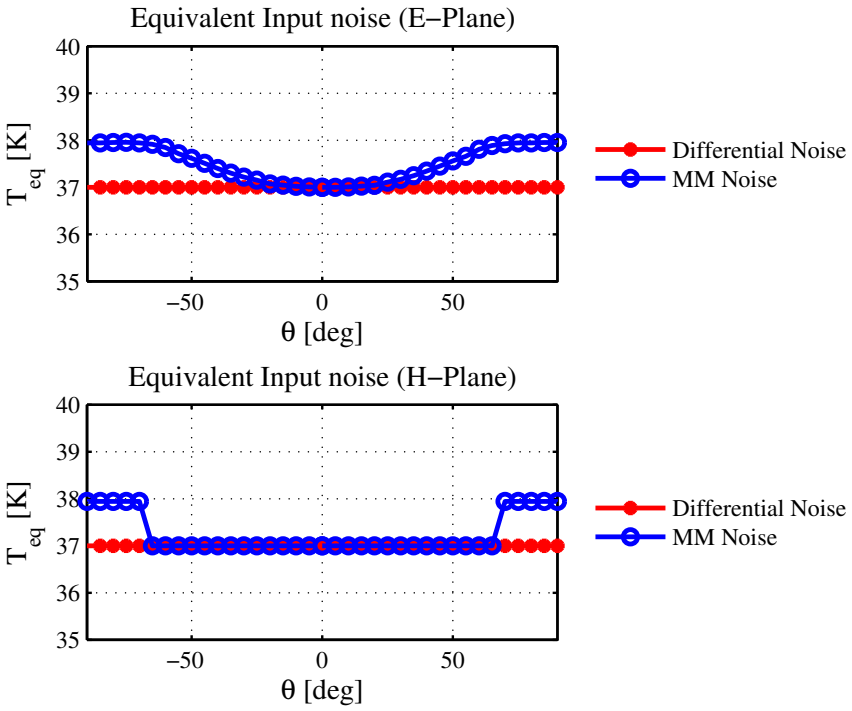

Figure 4.13: Purely differential and mixed differential- and common-mode (MM) equivalent input noise temperature in both the E- and H-planes.

increase in the complex common-mode weight values. Since the LNAs are noise matched to the passive differential impedance of the antenna, the common-mode noise mismatch results in a larger common-mode noise contribution. Considering Fig. 4.13 at $20° \leq \theta_{\text{scan}} \leq 50°$ from zenith, this common-mode noise is seen to increase the equivalent input noise of the dual-mode receiver proportionally to the common-mode weight values applied at these scan angles. As indicated in Fig. 4.11(a) the common-mode weights are substantially larger than the differential-mode weights at scan angles between $50° \leq \theta_{\text{scan}} \leq 90°$ from zenith, resulting in common-mode noise dominating the equivalent input noise of the dual-mode receiver. This behaviour is noted in the increase of the equivalent noise temperature of the dual-mode receiver in Fig. 4.13.

Next, consider the H-plane beamforming weight magnitudes and equivalent receiver noise contribution shown in Figs. 4.11(b) and 4.13, respectively. At scan angles $0° \leq \theta_{\text{scan}} \leq 60°$ from zenith Fig. 4.11(b) shows that the common-mode weights are nearly negligible compared to the differential-mode weights, hence the equivalent noise contribution of the weighted dual-mode receiver equals that of the purely differential receiver as shown in Fig 4.13. For scan angles $60° \leq \theta_{\text{scan}} \leq 90°$ from zenith, the common-mode weights are seen to dominate in the H-plane. Analogous to the E-plane, this increase in common-mode weights at these larger scan angles are seen to result in common-mode noise dominating the equivalent noise contribution of the dual-mode receiver as shown in Fig. 4.13.

Finally consider the sensitivity of the active dual-mode antenna. As indicated in (4.45), the receiving sensitivity is approximated by only accounting for the noise contributed by the LNAs. The normalised sensitivity, in both the E- and H-planes, of the dual-mode receiver is com-

pared to the sensitivity of a conventional purely differential receiver in Figs. 4.14(a) and (b), respectively.

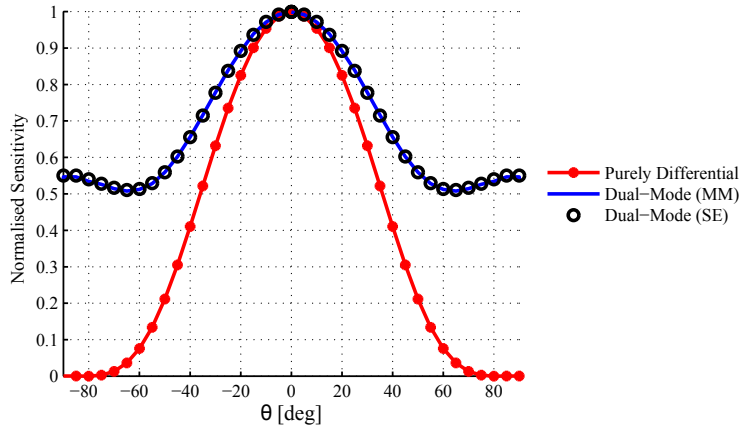

(a)

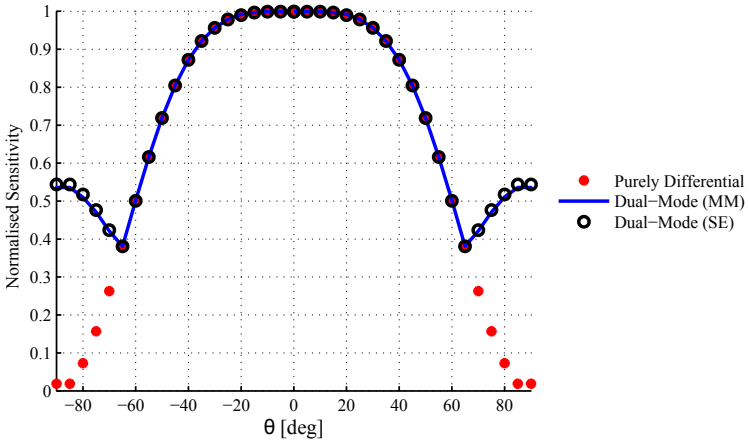

(b)

Figure 4.14: Purely differential and dual-mode sensitivity (a) E-plane and (b) H-plane.

Figure 4.14 indicates that, regardless of the increase in the equivalent noise temperature attributed to the common-mode present in the dual-mode receiver, the utilisation of common-mode excitation can result in an increase in the sensitivity over nearly all scan angles in the E-plane and for angles larger than 60° from zenith in the H-plane, when compared with the purely differential excitation. Comparing the variation in sensitivity in Fig. 4.14 to the gain variation depicted in Fig. 4.10 it is seen that the variation in sensitivity corresponds to the gain variation in both planes, with the sensitivity varying by less than 50% in the E-plane and 60% in the H-plane. Considering the sensitivity of the purely differential excitation a 90% reduction in sensitivity is seen at 60° E-plane scan, reducing to zero at 90°. Similar to the H-plane gain, the sensitivity of the purely differential excitation and the dual-mode antenna remain equal up to 60° in the H-plane, with the sensitivity of the purely differential excitation once again reducing to zero at 90°. Despite of the fact that the sensitivity shown in Fig. 4.14 does not take sky and spill-over noise into consideration, the graphs still illustrate that the utilisation of common-

mode propagation does not result in a reduction of the sensitivity. To verify the multi-mode signal and noise models introduced in this chapter, Fig. 4.14 shows the sensitivity obtained when analysing the antenna and receiver using the SE S-matrix $\mathbf{S}^{\mathrm{SE;ant}}$ and EEPs $\boldsymbol{f}_1^{\mathrm{SE}}$ and $\boldsymbol{f}_2^{\mathrm{SE}}$ with the corresponding SE complex beamforming weights $\{w_1^{\mathrm{SE}}, w_2^{\mathrm{SE}}\}$ solved for maximum SNR at each scan angle. It is clear from the graphs, that the SE and multi-mode representations are indeed equivalent.

Since the dual-mode antenna consists of only a single linearly polarised dipole element, the polarimetric performance of the active dual-mode antenna is not considered. Instead, the OPMN beamforming weights are solved for the dual-polarised conical quad-mode antenna in Sec. 4.4.

4.4 Active Conical Quad-Mode Antenna

The performance of the active quad-mode antenna of Sec. 3.4.1, repeated in Fig. 4.15 for ease of reading, with respect to gain, sensitivity and polarimetric performance is presented in this section.

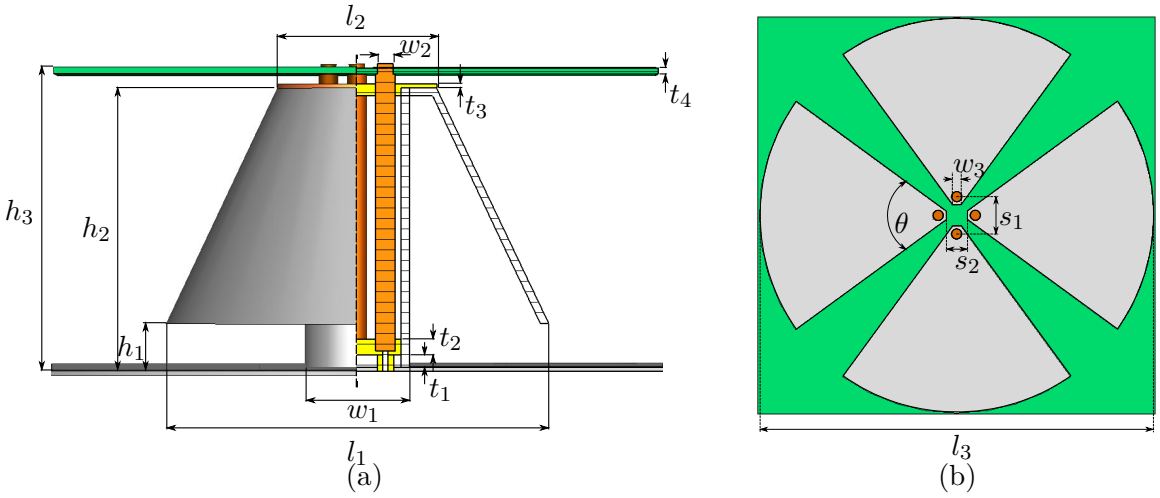

Figure 4.15: Conical quad-mode antenna (a) side view (b) top view.

The active quad-mode antenna is modelled using the simulated multi-mode response of the conical quad-mode antenna placed over an infinite ground plane, as presented in Sec. 3.4.1. Hence, the equivalent multi-mode receiver depicted in Fig. 4.1(b) is considered where $N = 4$ and the radiated far-field patterns $\boldsymbol{f}_1^{\mathrm{MM}}, ..., \boldsymbol{f}_4^{\mathrm{MM}}$ represent the four radiation patterns illustrated in Fig. 3.30 and the corresponding S-matrix of the quad-mode antenna $\mathbf{S}^{\mathrm{MM;ant}}$ is solved for the four orthogonal excitation modes shown in Fig. 3.15(a)–(d). Similar to the analysis of the active dual-mode antenna presented in Sec. 4.3, each of the four SE inner conductors of the quadraxial feed is connected to a SE LNA defined by the S- parameters and noise parameters listed in Table 4.1 – where $S_{11}^{\mathrm{MM;ant}}$ denotes the input reflection coefficient of excitation mode MM_1 depicted in Fig. 3.15(a). Applying the theory presented in Sec. 4.1 the equivalent multi-mode signal and

noise response of the four SE LNAs corresponding to the four orthogonal excitation modes can be obtained through (4.3) and (4.29) with the coefficients of matrices $\mathbf{K}^{\mathrm{v}}_{\mathrm{LNA}}$ and $\mathbf{K}^{\mathrm{i}}_{\mathrm{LNA}}$ defined as in (3.54) and (3.55), respectively. Using the equivalent multi-mode representation of the active quad-mode antenna, the complex beamforming weights corresponding to each of the four excitation modes can be solved to ensure maximum gain, sensitivity or polarimetric performance through the beamforming algorithms discussed in Sec. 4.2. In section 4.4.1, the performance obtained through the maximum gain and SNR beamformers is compared and in Sec. 4.4.2 the equivalent quad-mode polarimeter model is used to assess the polarimetric performance, where the effect polarimetric correction has on the sensitivity of the quad-mode polarimeter is presented [6].

4.4.1 Maximum gain and sensitivity

Using the equivalent multi-mode representation of the active quad-mode antenna the gain (4.77) and SNR (4.81) can be expressed in terms of the weighted EEPs, the multi-mode S-matrix of the antenna, and noise correlation matrix of the LNAs – solved using the equivalent multi-mode noise parameters through (4.54). Considering the response of the conical quad-mode antenna as simulated in CST Microwave Studio at 900 MHz, the performance of the active quad-mode antenna with respect to gain and sensitivity is maximised over the FoV coverage by solving the corresponding beamforming weights through the maximum gain and SNR beamforming algorithms discussed in Sec. 4.2.1 and Sec. 4.2.2. The normalised magnitudes of the weights solved for each excitation mode through the maximum gain (Max-Gain BF) and maximum SNR (Max-SNR BF) beamforming algorithms are shown over the hemispherical FoV coverage in Fig. 4.16.

The first observation that can be made of the beamforming weight magnitudes shown in Fig. 4.16 is that the weights allocated at each scan angle corresponds to the far-fields radiated by each excitation mode – where the distribution of weights solved for excitations MM_1 and MM_2 are seen to resemble the dipole-over-ground far-field patterns depicted in Figs. 3.30(a) and (b), the weights of excitation MM_3 that of the monopole far-field pattern in Fig. 3.30(c), and similarly the weight values solved for excitation MM_4 resembles the radiated far-field pattern shown in Fig. 3.30(d). By applying these weights to the four excitation modes at each scan angle the active quad-mode antenna achieves near-hemispherical FoV coverage. Furthermore, comparing the normalised weight magnitudes for maximum gain with the weight magnitudes for maximum SNR, it is evident from the lower Max-SNR beamformer weight values of mode MM_4 that noise match is the dominating factor at each scan angle when beamforming for maximum SNR. The fact that the LNAs are noise matched to the passive input impedance of mode MM_1, together with the similar input reflection coefficients of modes MM_1–MM_3 [c.f. Fig. 3.29], results in lower noise contribution for excitation modes MM_1–MM_3 than the mismatched mode MM_4. The weight magnitudes of modes MM_1–MM_3 are therefore seen to be much larger for the Max-SNR beamformer than for the Max-Gain beamformer, where the lower weight values of excitation MM_4 obtained through the Max-SNR beamformer is attributed to the mismatch observed for

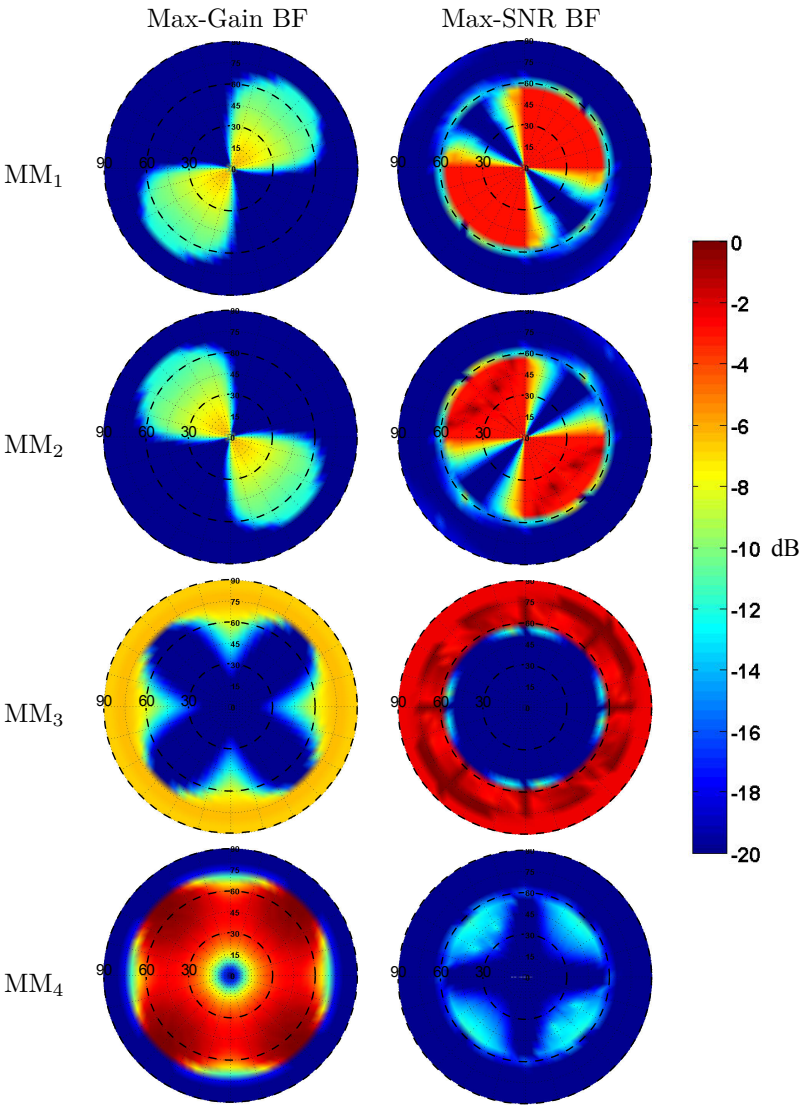

Figure 4.16: Normalised weight values solved for each mode at all scan angles over the hemispherical FoV at 900 MHz.

the mode [c.f. Fig. 3.29]. This mismatch of MM_4 is seen to result in much larger weight values when beamforming for maximum gain.

Using the weights illustrated in Fig. 4.16 the gain and sensitivity, solved through (4.77) and (4.45), over the hemispherical FoV coverage when beamforming for maximum gain and SNR are shown in Fig. 4.17. The effect of the dominant MM_4 mode realised by the Max-Gain beamformer is clearly visible in both the gain and sensitivity over the FoV, where a higher gain is achieved at scan angles corresponding to the radiated far-field of MM_4 and a decrease in sensitivity is observed at these scan angles due to the noise mismatch of the MM_4 mode. The gain realised by the Max-Gain beamformer is seen to peak around 9.5 dB at 40° from zenith in the diagonal planes and decreases to a minimum of 5 dB at 90° from zenith. Figure 4.17 shows that the Max-SNR beamformer results in a near axisymmetric gain pattern, with a maximum gain of approximately 8.5 dB at zenith and a minimum of 5 dB toward the horizon. Since the Max-SNR beamforming weights ensure minimum noise contribution from the active quad-mode antenna,

a much smaller variation in sensitivity is observed over the hemispherical FoV for the Max-SNR beamfoming weights. Following, the performance of the active quad-mode antenna at the lower and upper frequencies (800 MHz and 1.1 GHz), where the input match of modes MM_1–MM_3 are below -10 dB, is considered.

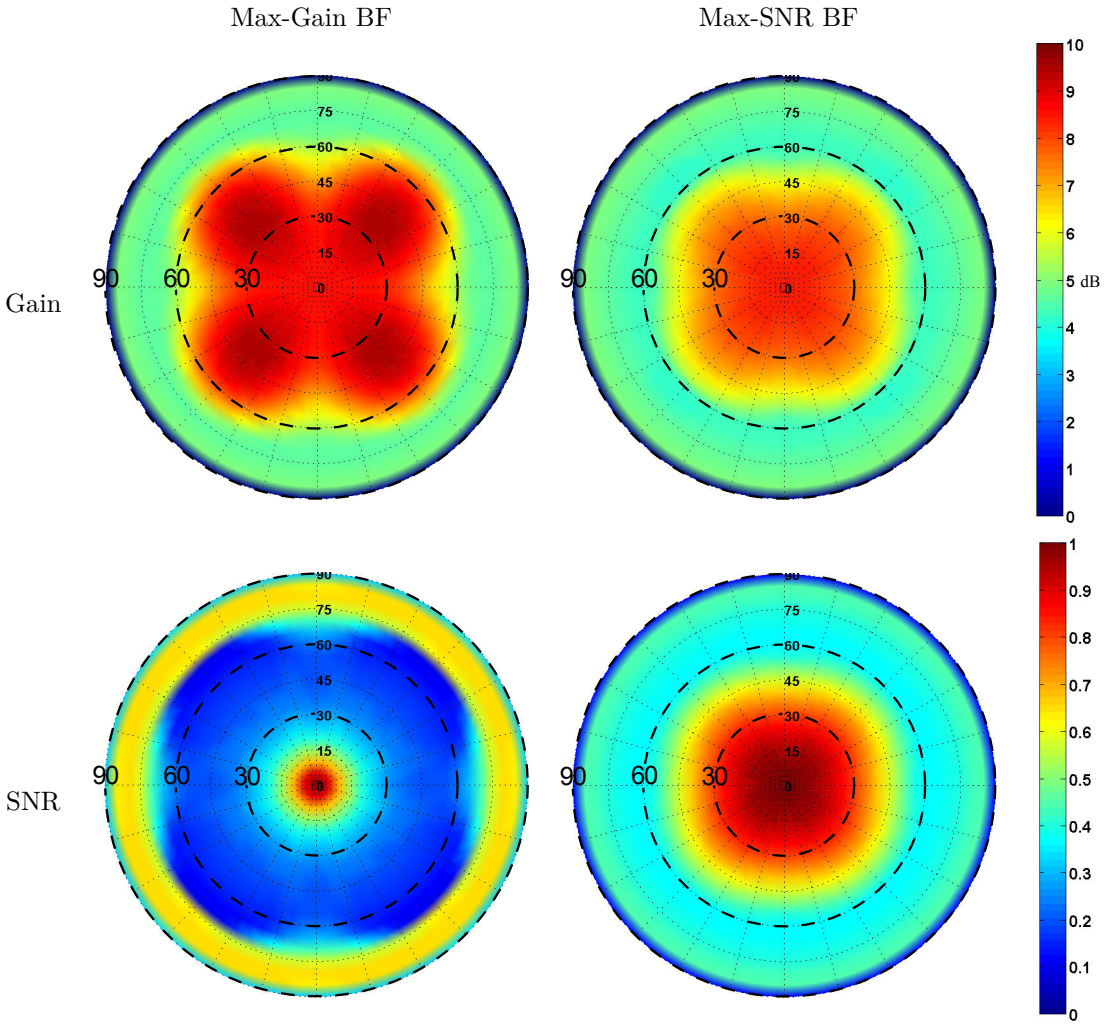

Figure 4.17: Gain and normalised sensitivity (SNR) over the hemispherical FoV at 900 MHz.

Gain and sensitivity at the operating frequency band edges

Similar to the preceding discussion, the performance of the active quad-mode antenna for the Max-Gain and Max-SNR beamformers is assessed, comparing the gain and sensitivity over the FoV coverage resulting from the beamforming weights computed through each beamforming algorithm. First consider Fig. 4.18 showing the normalised weight magnitudes of each excitation mode over the hemispherical FoV coverage at 800 MHz and 1.1 GHz, obtained from the Max-Gain and Max-SNR beamformers. Once again the weights allocated at each scan angle are seen to correspond to the radiated far-field patterns illustrated in Fig. 3.30, with the Max-Gain beamformer assigning the largest weight values to the mismatched mode MM_4. Comparing the

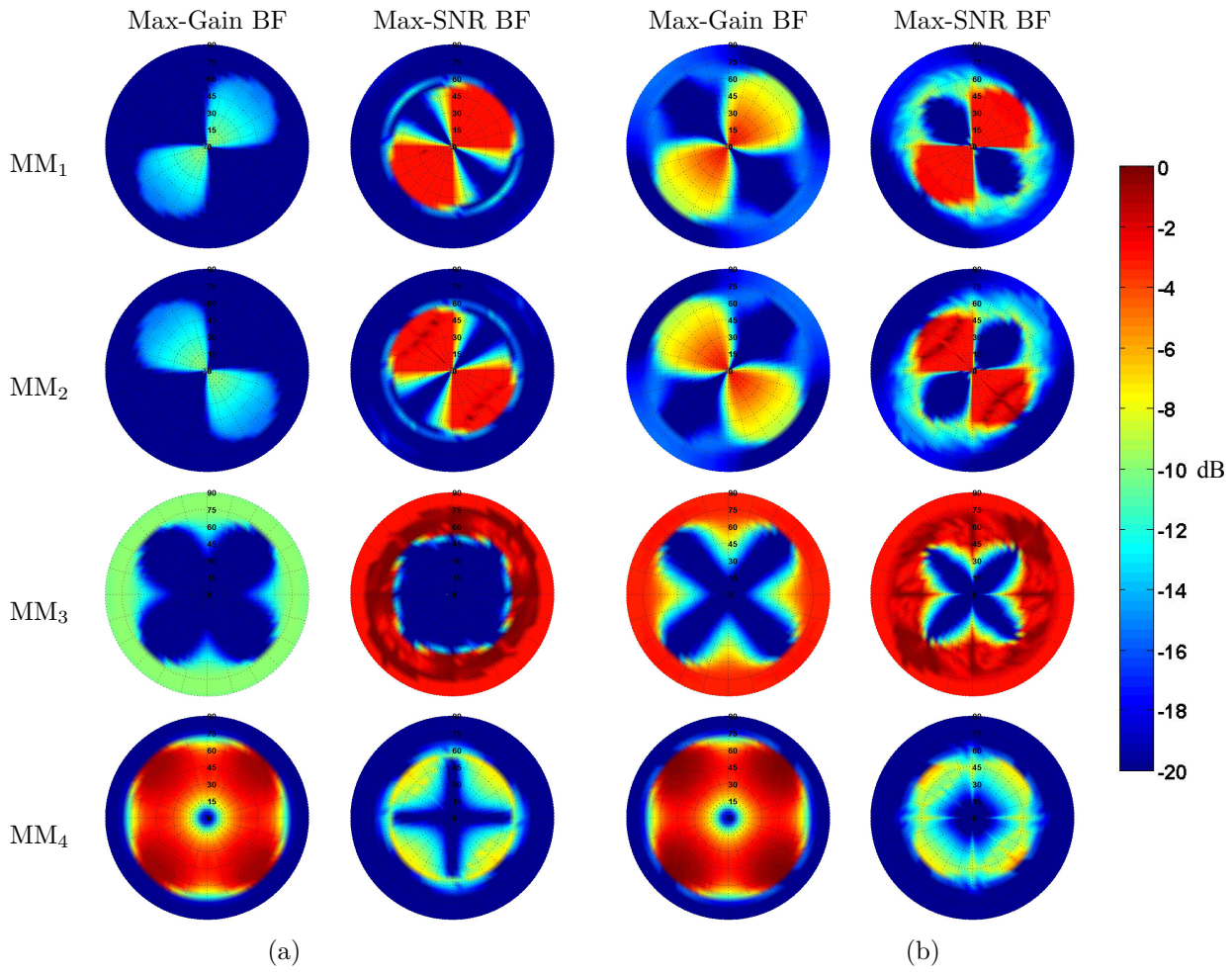

Figure 4.18: Normalised weight values solved for each mode at all scan angles over the hemispherical FoV at (a) 800 MHz and (b) 1.1 GHz.

relative weight magnitudes of modes MM_1–MM_3 solved by the Max-Gain beamformer at 800 MHz and 1.1 GHz, an increase in the relative weight magnitudes of modes MM_1–MM_3 is seen at 1.1 GHz. Considering the realised gain of the four excitation modes at 1.1 GHz, depicted in Fig. 3.31(d), it is seen that this increase in the relative weight values of modes MM_1–MM_3 corresponds to the smaller difference between the realised gain of the four excitation modes.

The maximum gain and sensitivity at 800 MHz and 1.1 GHz resulting from the weight values obtained through the Max-Gain beamformer are shown in Fig. 4.19. It is seen that the maximum gain resulting from the weight values at the two frequencies are virtually identical, whereas a larger difference is noted between the corresponding sensitivities (SNR). The improved sensitivity observed at 1.1 GHz is ascribed to the increase in the weight magnitudes of modes MM_1–MM_3 resulting in a lower equivalent noise temperature as defined in (4.44).

Next, consider the normalised weight magnitudes solved through the Max-SNR beamformer (Max-SNR BF) at 800 MHz and 1.1 GHz shown in Figs. 4.18(a) and (b). Recalling that the LNAs are noise matched to the passive input impedance of mode MM_1, the similar input match observed for modes MM_1–MM_3 [c.f. Fig. 3.29] results in lower noise contribution from these

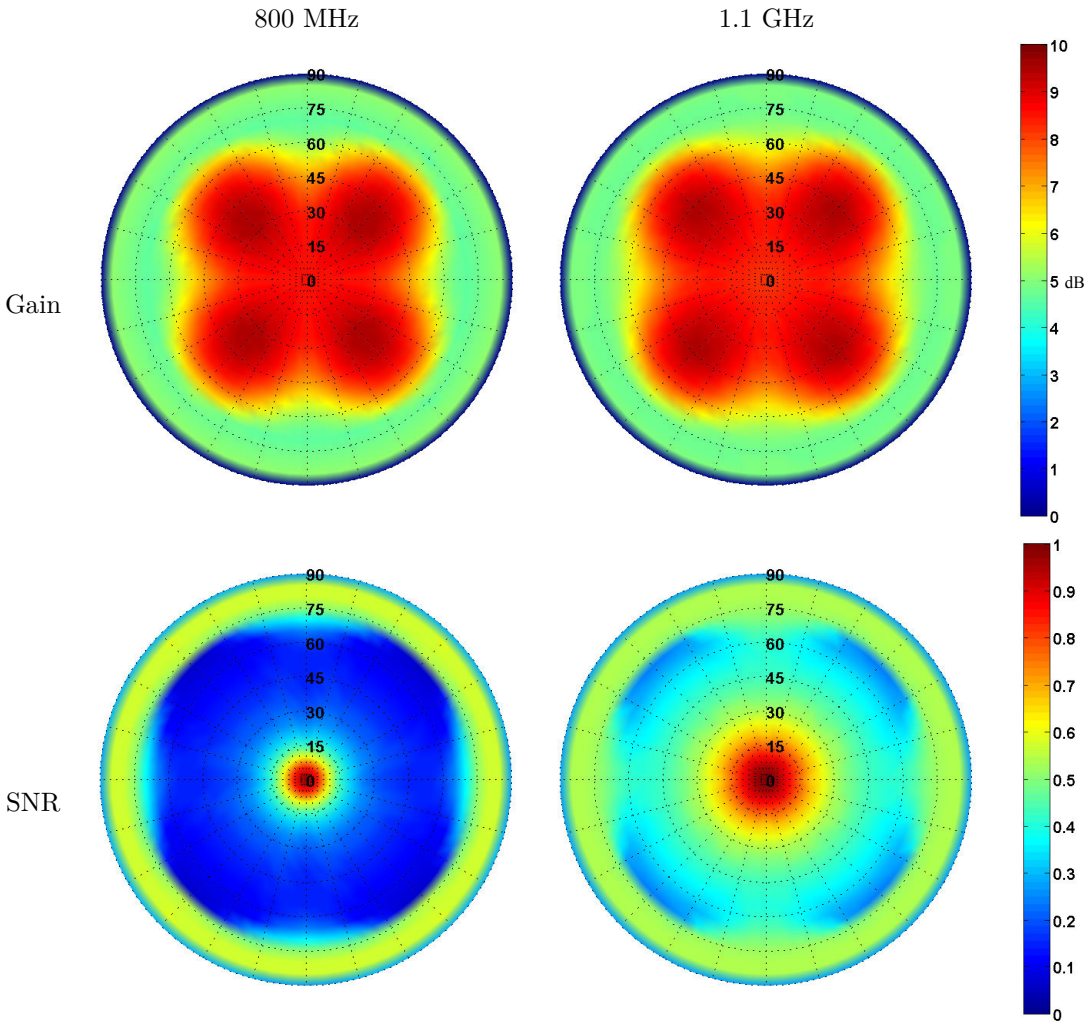

Figure 4.19: Max-Gain beamformer: gain and normalised sensitivity (SNR) over the hemispherical FoV at 800 MHz and 1.1 GHz.

modes, compared to the mismatched MM_4 mode. This is once again reflected in the larger weight magnitudes of modes MM_1–MM_3 solved when maximising the SNR at both frequencies. As shown in Fig. 4.20 the Max-SNR beamforming weights solved at 800 MHz and 1.1 GHz again result in a more axisymmetric gain variation over the hemispherical FoV coverage, with a maximum gain variation of approximately 4.5 dB observed at 800 MHz which is seen to reduce to below 4 dB at 1.1 GHz. This lower variation in the maximum gain over the FoV coverage at 1.1 GHz, together with near equal active reflection coefficients of the dominant excitation modes (MM_1–MM_3) is seen to result in less than 50% variation in sensitivity over the entire FoV coverage.

In this section the gain and sensitivity of the active quad-mode antenna are assessed using complex beamforming weights solved from the total field intensity radiated by the four orthogonal excitation modes of the antenna. The following section considers the polarimetric performance of the active quad-mode antenna by solving two sets of beamforming weights corresponding to two orthogonal incident field components, as discussed in Sec. 4.1.3.

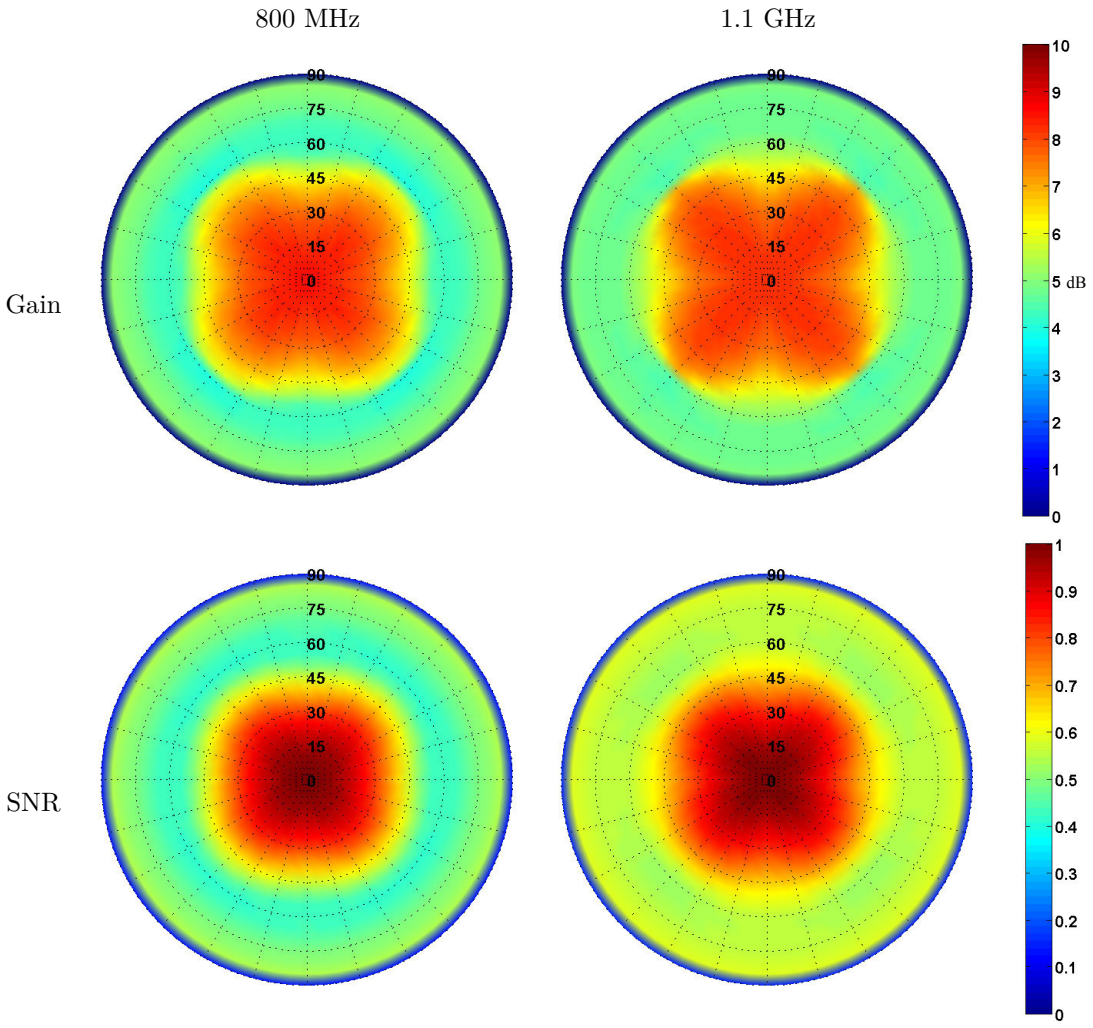

Figure 4.20: Max-SNR beamformer: gain and normalised sensitivity (SNR) over the hemispherical FoV at 800 MHz and 1.1 GHz.

4.4.2 Quad-mode polarimeter

Using the equivalent polarimeter model introduced in Sec. 4.1.3 the beamforming algorithms discussed in Sec. 4.2.3 are applied in this section to assess the polarimetric performance as well as the effect polarimetric correction has on the sensitivity of the active quad-mode antenna. As depicted in Fig. 4.8, the multi-mode response of the active quad-mode antenna can be modelled as a four element polarimetric array, where each array element represents one of the orthogonal excitation modes. For the analysis to follow an unpolarised incident electric field, defined according to (4.59), is assumed. It then follows from reciprocity that the signals induced at the antenna port by each component of the incident electric field are proportional to the field components radiated by each excitation mode. Hence, in calculating the complex beamforming weight values, the signal response of the polarimeter, $\mathbf{e}_{\mathrm{u}}$ and $\mathbf{e}_{\mathrm{v}}$, corresponding to a $\hat{\boldsymbol{u}}$- and $\hat{\boldsymbol{v}}$-polarised incident electric field are considered equal to the corresponding field components, $\boldsymbol{F}^{\mathrm{u}} = [f_1^{\mathrm{u}}(\theta,\phi) \ \ldots \ f_4^{\mathrm{u}}(\theta,\phi)]^T$ and $\boldsymbol{F}^{\mathrm{v}} = [f_1^{\mathrm{v}}(\theta,\phi) \ \ldots \ f_4^{\mathrm{v}}(\theta,\phi)]^T$, radiated by the four orthogonal excitation modes.

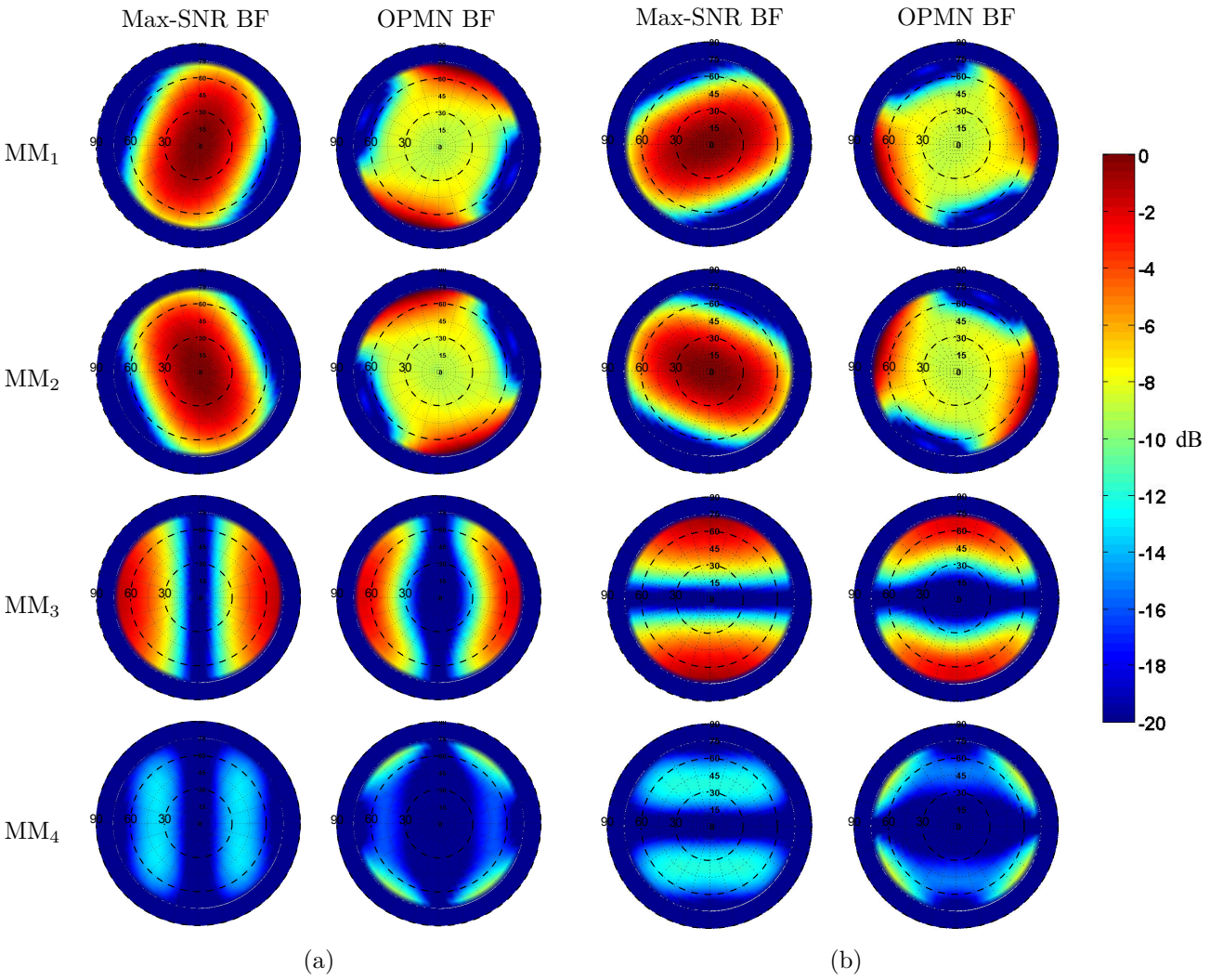

Figure 4.21: Normalised weight values of the Max-SNR and OPMN beamformers for (a) pol. beam-1 and (b) pol. beam-2 solved at 900 MHz for each mode over the hemispherical FoV.

Similar to the analysis discussed in Sec. 4.4.1, the sensitivity of each polarimeter beam can be maximised over the FoV coverage using the noise correlation matrix (4.54), defined in terms of the equivalent multi-mode noise parameters of the LNAs. That is, by applying the maximum SNR (Max-SNR) beamforming algorithm the weight sets $\mathbf{W}_{\text{SNR}} = [\mathbf{w}_1\ \mathbf{w}_2]$ can be solved at each scan angle through the expression in (4.84), with $\mathbf{E} = [\boldsymbol{F}^{\text{u}}\ \boldsymbol{F}^{\text{v}}]$. Since the Max-SNR beamformer does not calibrate the polarimetric response of the quad-mode polarimeter, the OPMN beamforming algorithm (4.87) is applied to the weight sets $\mathbf{W}_{\text{SNR}}$ to achieve optimal polarimetric performance while retaining minimum noise contribution from the receiver. Figure 4.21 compares the normalised weight magnitudes for the polarimetric beam pair, solved at 900 MHz over the hemispherical FoV using the Max-SNR and OPMN beamforming algorithms. To obtain a clearer understanding of the differences observed between the weight magnitudes solved for each mode by the two beamformers, first consider the polarimetric performance of the Max-SNR beamforming weight sets.

The polarimetric performance is assessed using the Intrinsic Cross-polarisation Ratio (IXR)

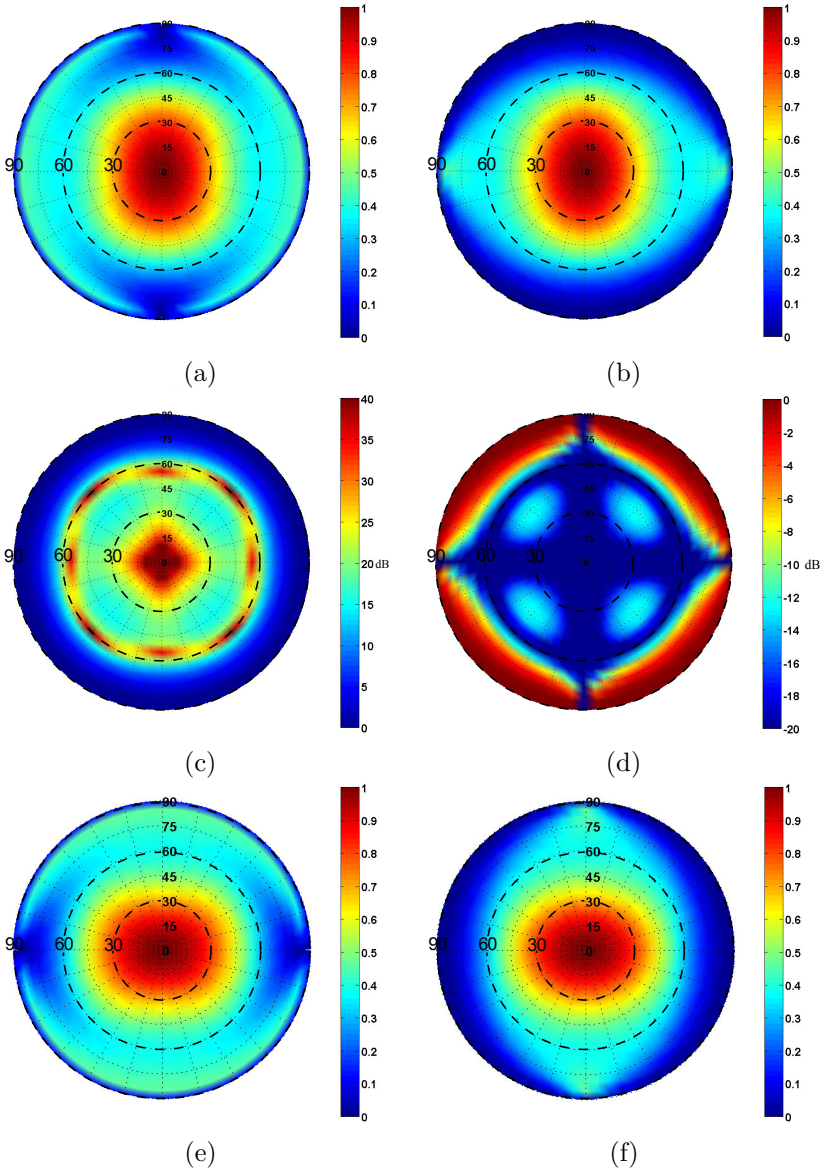

Figure 4.22: (a) SNR of pol. beam-1 (max-SNR BF), and (b) SNR of pol. beam-1 (OPMN BF), (c) IXR (max-SNR BF), (d) relative difference in SNR due to polarimetric correction realised by the OPMN BF, (e) SNR of pol. beam-2 (max-SNR BF), and (f) SNR of pol. beam-2 (OPMN BF) at 900 MHz.

introduced in Sec. 4.1.3. The IXR achieved over the hemispherical FoV coverage through the Max-SNR beamforming weights is shown in Fig. 4.22(c). As shown in Fig. 4.22(c), the Max-SNR beamformer realises IXR values greater than 15 dB for scan angles up to 65° from zenith, where the lower IXR values for larger scan angles can be attributed to the lower gain of modes MM_1 and MM_2 at these scan angles. Considering the normalised weight values of pol. beam-1 [c.f. Fig. 4.21(a)] obtained through the Max-SNR and OPMN beamformers, it is seen that the OPMN beamformer compensates for the lower gain at larger scan angles by increasing the relative weight values at these angles. This result is also noted when comparing the weight values of pol. beam-2 [c.f. Fig. 4.21(b)], solved by the two beamforming algorithms. As expected, the resulting IXR for the OPMN beamforming weights is numerically infinite over the entire FoV, and is therefore not shown.

Next, consider the sensitivity of the two quad-mode polarimeter beams realised through the Max-SNR and OPMN beamformers, compared in Figs. 4.22(a) and (b) and Figs. 4.22(e) and (f). In [46] the OPMN beamformer is described as *sensitivity equivalent* to the Max-SNR beamformer, implying that the sensitivity over the FoV coverage remains bounded by the same values before and after polarimetric correction. Considering the sensitivity of pol. beam-1 [c.f. Figs. 4.22(a) and (b)], it is interesting to note that the OPMN beamformer retains the same sensitivity only in the $\phi = 0°$ plane and for scan angles up to 65° from zenith. The same result is observed when comparing the sensitivity of pol. beam-2 in Figs. 4.22(e) and (f), where the same values for sensitivity is obtained from the Max-SNR and OPMN beamformers only in the $\phi = 90°$ plane and again only up to scan angles of 65°.

This phenomenon can be ascribed to the fact that the relative weight values of mode MM_3 obtained through both beamformers remain mostly unchanged in the $\phi = 0°$ and $\phi = 90°$ planes for the respective polarimeter beams [c.f. Fig. 4.21]. Furthermore, given the poor polarimetric performance of the Max-SNR beamformer at scan angles larger than 65° [c.f. Fig. 4.22(c)], the weight values resulting from the polarimetric correction of the OPMN beamformer, result in a decrease in the sensitivity at these scan angles. This decrease in sensitivity corresponding to poor polarimetric performance is clearly illustrated in Fig. 4.22(d) showing the normalised relative difference in sensitivity obtained through the Max-SNR and OPMN beamformers. A comparison between the relative difference in sensitivity [c.f. Fig. 4.22(d)] and the IXR achieved by the Max-SNR beamformer [c.f. Fig. 4.22(c)] illustrates that the OPMN beamformer degrades the sensitivity at scan angles of lower IXR, showing a relative difference in sensitivity of approximately 10 percent results when polarimetrically correcting IXR values below 13 dB.

Quad-mode polarimeter performance at operating frequency band edges

Following the same procedure performed at 900 MHz, the performance of the quad-mode polarimeter at 800 MHz and 1.1 GHz is assessed. Given the similarity of the weight values and sensitivities solved for the two polarimeter beams by the Max-SNR and OPMN beamformers shown in Figs. 4.21 and 4.22, only the performance of pol. beam-1 is considered in the following analysis. From the normalised weight magnitudes solved through both beamformers at 800 MHz and 1.1 GHz, illustrated in Figs. 4.23(a) and (b), it is once again seen that the OPMN beamformer results in an increase in the weight magnitudes at larger scan angles. Considering the IXR solved at both frequencies using the Max-SNR beamforming weights [c.f. Figs. 4.24(c) and (g)] it is seen that this increase in the OPMN beamformer weight values correspond to scan angles with low IXR values prior to polarimetric correction. Regarding the IXR values shown in Figs. 4.24(c) and (g), it is shown that the Max-SNR beamforming weights result in IXR values above 15 dB up to 60° from zenith, falling just below this value at 60° in the principal planes at 1.1 GHz. Finally, comparing the sensitivity of pol. beam-1 before and after polarimetric correction at 800 MHz and 1.1 GHz, as shown in Figs. 4.24(a) and (b) and Figs. 4.24(e) and (f) respectively, a similar reduction in sensitivity is noted at scan angles corresponding to low IXR values obtained through the Max-SNR beamforming weights. As illustrated in Figs. 4.24(d)

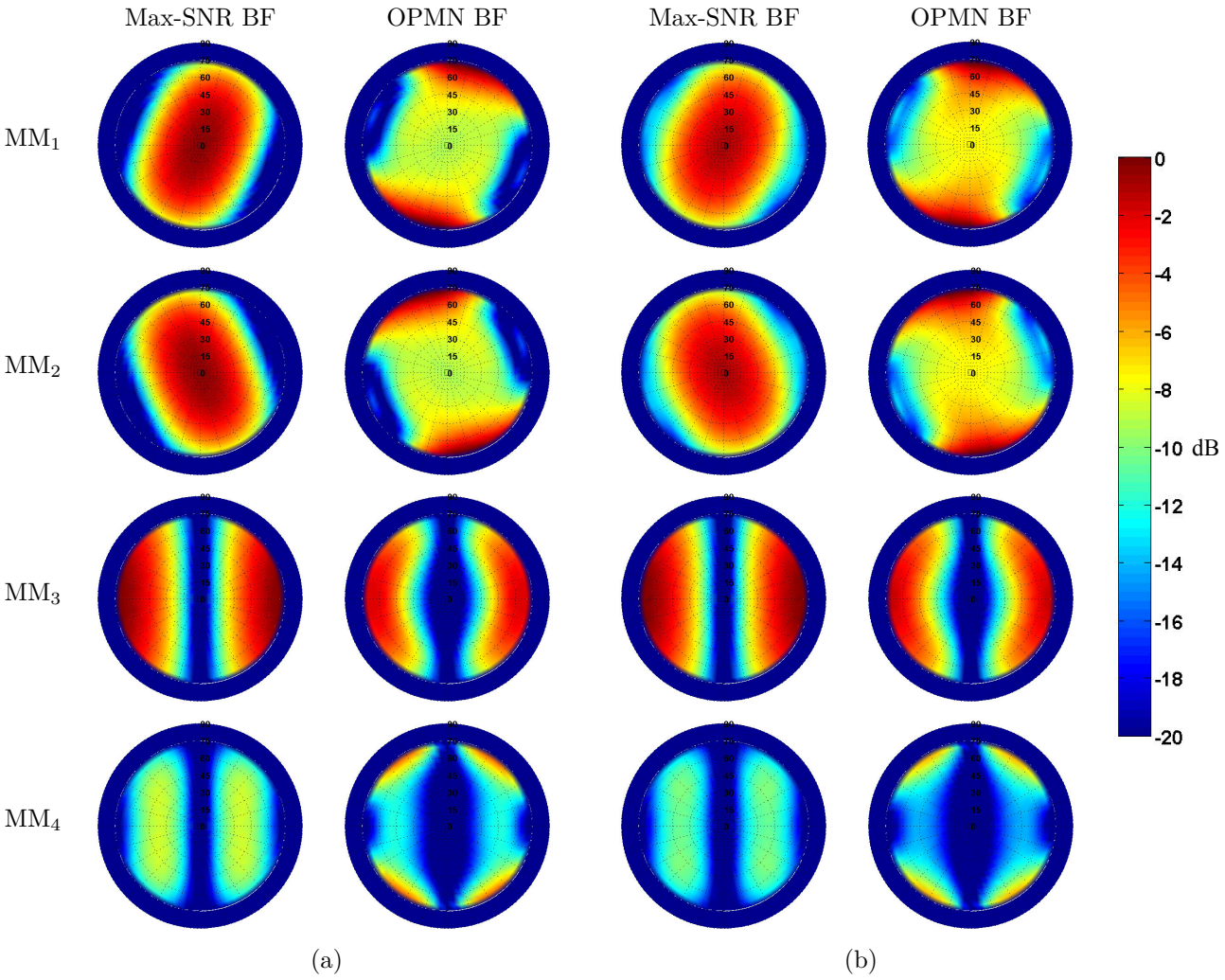

Figure 4.23: Normalised weight values of pol. beam-1 solved for each mode at (a) 800 MHz and (b) 1.1 GHz over the hemispherical FoV through the Max-SNR and OPMN beamformers.

and (h), showing the normalised difference in sensitivity obtained through the Max-SNR and OPMN beamformers, at least 10 percent difference in sensitivity results when polarimetrically correcting IXR values below 13 dB.

Polarimetric performance compared with dual-polarised dipole antenna

Before concluding this chapter, it is interesting to point out the improved polarimetric performance achieved through the utilisation of the available orthogonal excitation modes of the quad-mode antenna. To illustrate this improvement, the IXR of the quad-mode antenna is compared with the IXR of a conventional dual-polarised dipole antenna. In this analysis the dual-polarised dipole antenna is realised by removing the conical monopole element from the quad-mode antenna design introduced in Sec. 3.4.1 thereby resulting in only two perpendicular bow-tie elements, excited through a quadraxial transmission line. Given the purely differential nature of the bow-tie dipole elements, only excitation modes MM_1 and MM_2, depicted in Figs. 3.15(a) and (b) are considered when computing the IXR of the dual-polarised dipole

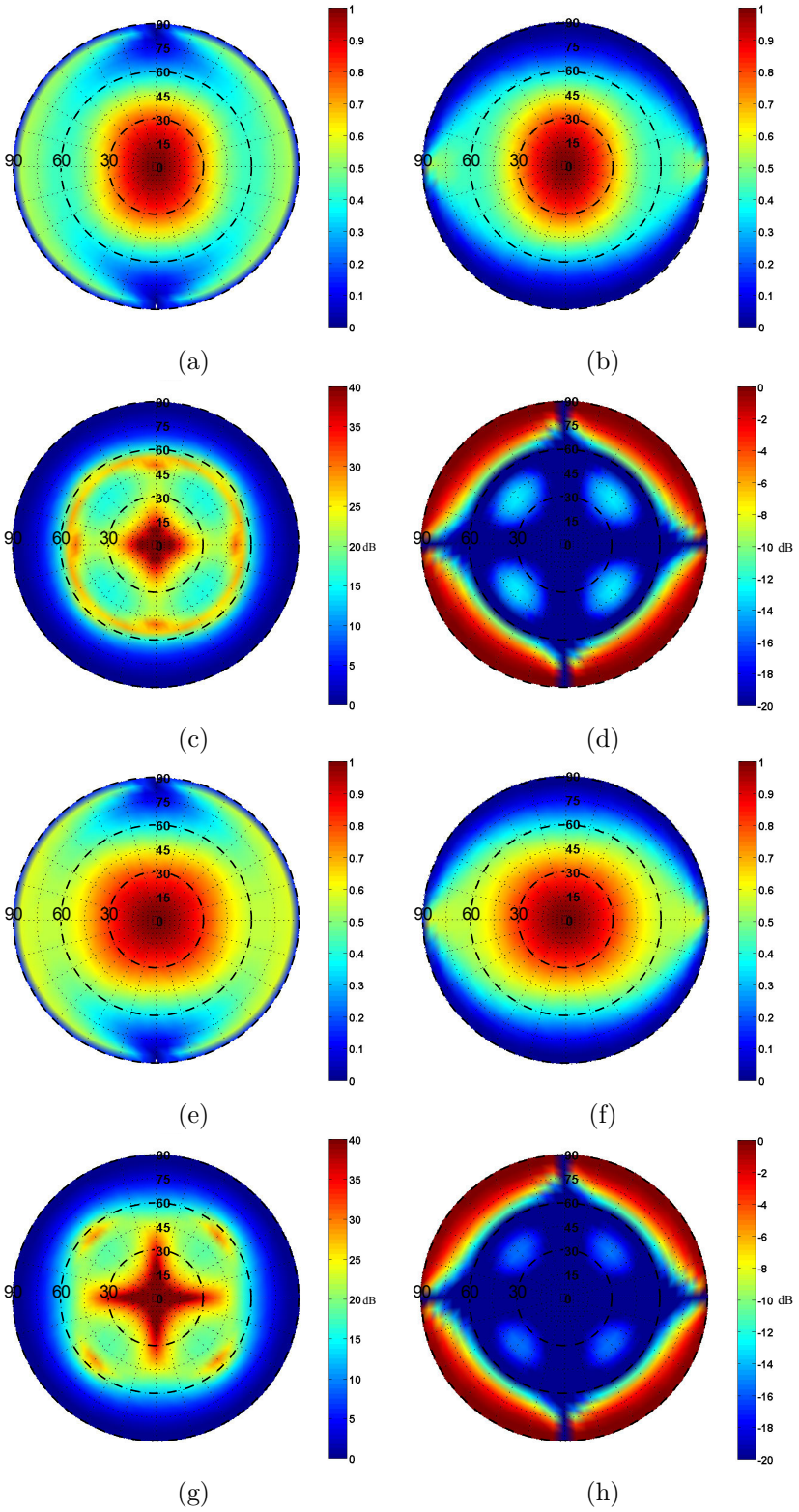

Figure 4.24: 800 MHz: (a) SNR of pol. beam-1 (max-SNR BF), and (b) SNR of pol. beam-1 (OPMN BF), (c) IXR (max-SNR BF), and (d) relative difference in SNR due to polarimetric correction realised by the OPMN BF, 1.1GHz: (e) SNR of pol. beam-1 (max-SNR BF), and (f) SNR of pol. beam-1 (OPMN BF), (g) IXR (max-SNR BF), and (h) relative difference in SNR due to polarimetric correction realised by the OPMN BF.

antenna. Hence, the voltage and current coefficient matrices reduce to

$$\mathbf{K}^{\mathrm{v}} = \begin{bmatrix} \frac{1}{2} & \frac{1}{2} & -\frac{1}{2} & -\frac{1}{2} \\ \frac{1}{2} & -\frac{1}{2} & -\frac{1}{2} & \frac{1}{2} \end{bmatrix} \tag{4.89}$$

and

$$\mathbf{K}^{\mathrm{i}} = \begin{bmatrix} \frac{1}{2} & \frac{1}{2} & -\frac{1}{2} & -\frac{1}{2} \\ \frac{1}{2} & -\frac{1}{2} & -\frac{1}{2} & \frac{1}{2} \end{bmatrix}. \tag{4.90}$$

In solving the IXR, the same receiver model applied to the analysis of the active quad-mode antenna is used for the dual-polarised active dipole antenna, i.e. each of the inner conductors of the quadraxial feed is connected to an identical SE LNA defined according to the parameters summarised in Table 4.1. Since only two of the four orthogonal excitation modes supported by the quadraxial feed are considered, the noise correlation matrix corresponding to the two excitation modes results in a $[2 \times 2]$ matrix defined using (4.54), with the equivalent noise temperatures expressed in terms of the equivalent noise parameters of the two excitation modes as obtained through (4.29). Using the equivalent noise correlation matrix the weight set of each polarimetric beam can be solved using (4.84), where the signals induced at the antenna port $\{\mathbf{e}_{\mathrm{u}}, \mathbf{e}_{\mathrm{v}}\}$ by a $\hat{\boldsymbol{u}}$- and $\hat{\boldsymbol{v}}$-polarised incident wave are equated to the corresponding field components radiated by the two excitation modes $\{\boldsymbol{F}^{\mathrm{u}} = [f_1^{\mathrm{u}}\ f_2^{\mathrm{u}}]^T,\ \boldsymbol{F}^{\mathrm{v}} = [f_1^{\mathrm{v}}\ f_2^{\mathrm{v}}]^T\}$.

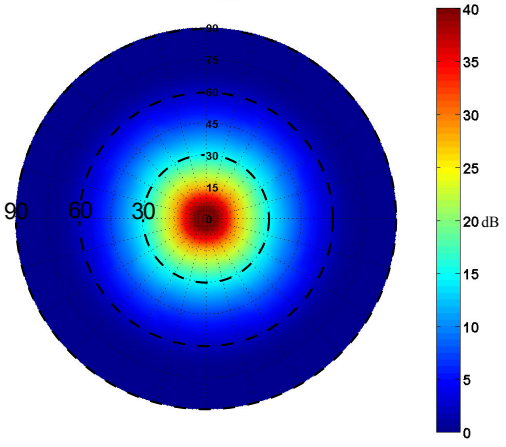

Figure 4.25: IXR of dual-polarised bow-tie dipole antennas excited through modes MM_1 and MM_2.

Considering the IXR of the active dual-polarised dipole antenna solved using these beamforming weights at 900 MHz, shown in Fig. 4.25, it is seen that IXR values above 15 dB is only achieved up to scan angles of 30° from zenith. Comparing the IXR of the active dual-polarised dipole antenna with that achieved by the active quad-mode antenna shown in Fig. 4.22(c), it is clear that the use of all available excitation modes supported by the quad-mode antenna design results in a significant improvement in polarimetric performance – where the IXR values are seen to remain above 15 dB up to 60° from zenith.

4.5 Conclusion

This chapter presents an equivalent network representation through which the performance of an active multi-mode antenna can be assessed. The equivalent multi-mode representation models the active multi-mode antenna as an array of single-mode antennas, where each single-mode antenna represents one of the orthogonal excitation modes supported by the multi-mode antenna. In order to characterise both the signal and noise response of the multi-mode receiver, transformations are presented to solve the equivalent multi-mode signal and noise response of the SE LNAs connected to the inner conductors of the multiconductor transmission line. Using the equivalent multi-mode network representation, expressions are derived through which the sensitivity and polarimetric performance of the active multi-mode antenna can be characterised in terms of arbitrary complex beamforming weights applied to each excitation mode.

Through the use of three beamforming algorithms, methods to solve complex beamforming weight values resulting in maximum gain, sensitivity and polarimetric performance at each scan angle is introduced. The presented theory is used to assess the performance of two active multi-mode antennas: the dual-mode and the conical quad-mode antenna. Applying the maximum SNR beamforming algorithm, the maximum sensitivity over the hemispherical FoV of the dual-mode antenna is compared with the sensitivity of a single linearly polarised dipole antenna of similar dimensions. The presented results show that effective utilisation of both excitation modes supported by a balanced transmission line allows for near-hemispherical FoV coverage, with the dual-mode antenna showing a variation in sensitivity of only 50 % over the entire FoV coverage in the E-plane. In comparison, the sensitivity of the purely differential dipole antenna is seen to fall below this value at scan angles greater than 35° from zenith.

Applying the multi-mode network representation to assess the performance of the active quad-mode antenna, the improved gain and sensitivity performance over the FoV, achieved through the judicious use of all available excitation modes, is once again demonstrated. Furthermore, comparing the IXR of the quad-mode antenna with a purely differential dual-polarised bow-tie dipole antenna of similar dimensions, illustrates the significant improvement in polarimetric performance over the FoV coverage achieved by the quad-mode antenna. Finally by modelling the active quad-mode antenna as a quad-mode polarimeter, the optimal-polarisation minimum-noise beamforming algorithm is applied to solve the complex beamforming weights that result in a calibrated polarimetric response while retaining minimum noise contribution from the receiver. Comparing the sensitivity of each polarimetric beam before and after polarimetric correction, it is demonstrated that a 10 % difference in sensitivity results when polarimetrically correcting at scan angles where the IXR is below 13 dB before polarimetric correction. Since the IXR of the quad-mode antenna is above 15 dB up to scan angles of 60° from zenith, the sensitivity over the FoV coverage of the quad-mode polarimeter beams remains virtually unchanged over 70 % of the hemispherical FoV coverage after polarimetric correction.

Chapter 5

Conclusion

In contrast to the purely differential antenna elements implemented in the state-of-the-art phased array radio telescopes, this dissertation presents multi-mode antenna elements excited with multiconductor transmission lines supporting multiple orthogonal Transverse Electromagnetic (TEM) modes. By means of three multi-mode antenna designs it is illustrated that each orthogonal TEM mode excites a unique radiation pattern that, collectively, allow for near-hemispherical Field-of-View (FoV) coverage. The presented multi-mode antenna designs include a dual-mode antenna comprising a single linearly polarised dipole and co-located monopole allowing for excitation through both differential- and common-mode signals supported by the twinaxial transmission line feed, as well as two quad-mode antennas comprising dual-polarised dipoles and a co-located monopole supporting four orthogonal TEM excitation modes through a quadraxial transmission line feed.

In order to characterise the multi-mode response of these antenna designs, generalised expressions are derived to solve the multi-mode S-parameters and radiated far-field patterns from the S-parameters and far-fields obtained from Single-Ended (SE) excitations. These transformations are validated through both the simulated and measured response of a cylindrical dual-mode antenna and a conical quad-mode antenna design.

To demonstrate the extended FoV coverage achieved by the multi-mode antenna designs, an equivalent network representation of an active multi-mode antenna is presented. Expression are derived by which the multi-mode signal and noise response of the SE Low-Noise Amplifiers (LNAs) connected to each SE conductor of the multi-mode antenna feed can be solved from the two-port S-parameters and noise parameters of the SE LNAs. It is illustrated that the equivalent representation allows for the use of conventional beamforming algorithms to assign complex weight values to each orthogonal excitation mode in order to maximise the gain, sensitivity or polarimetric performance over the FoV coverage. The improved response with respect to sensitivity, achieved through the utilisation of additional modes present within a multiconductor feed, is demonstrated through the analysis of both an active dual-mode and active quad-mode antenna. Through the added use of common-mode excitation, the active dual-mode antenna

is shown to achieve a variation in sensitivity below 50% in the entire hemispherical E-plane, whereas for a single purely differential dipole of similar dimensions the sensitivity is shown to fall below 50% at scan angles greater than 35° from zenith.

Similarly, by solving complex beamforming weight values through the Max-SNR beamformer for the four orthogonal excitation modes supported by the active conical quad-mode antenna, it is shown that the variation in sensitivity across the operating frequency bandwidth is between 60% and 50% over the entire hemispherical FoV coverage. Furthermore, by comparing the polarimetric response of the conical quad-mode antenna to that of a dual-polarised bow-tie antenna of similar dimensions, the improved polarimetric performance achieved through the additional use of the available excitation modes present in the quadraxial feed is illustrated. Using the Intrinsic Cross-polarisation Ratio (IXR) as a polarimetric figure-of-merit, it is shown that the conical quad-mode antenna achieves IXR values above 15 dB up to scan angles of 60° from zenith – an increase of nearly a factor four with respect to FoV coverage as compared with the purely differential dual-polarised bow-tie dipole antennas. Lastly, through the use of the Optimal-Polarisation Minimum-Noise (OPMN) beamforming algorithm, it is demonstrated that the active conical quad-mode antenna allows for a calibrated polarimetric response, with the sensitivity remaining virtually unchanged for scan angles up to 60° from zenith.

Expansion to the work presented in this dissertation could include: improving the input match of excitation mode MM_4 of the quad-mode antenna design, analysing the multi-mode response of an active multi-mode antenna comprising non-identical SE LNAs that are coupled to one another, as well as an analysis of the sensitivity of a quad-mode antenna design taking sky and spill-over noise into consideration. Furthermore, since the multi-mode antenna designs presented in this work does not yet meet the required bandwidth for the aperture arrays of the Square Kilometre Array telescope as isolated elements, future studies can be performed to investigate bandwidth improvement through mutual coupling in an array environment. This study could include a cost assessment of an anticipated SKA-size array of quad-mode antennas. Nonetheless, the work presented in this dissertation illustrates that improved performance with respect to gain, sensitivity, and polarimetric performance can be attained over an enhanced FoV coverage through the judicious use of the multiple radiation patterns which are characteristic of multi-mode antennas excited by multi-mode transmission lines.

Bibliography

[1] R. T. Schilizzi *et al.* (2007, Dec.) Preliminary specifications for the square kilometre array. 100_Memo_Schilizzi.pdf. [Online]. Available: http://www.skatelescope.org/PDF/memos/

[2] D. Prinsloo, P. Meyer, R. Maaskant, and M. Ivashina, "Design of an active dual-mode antenna with near hemispherical field of view coverage," in *Int. Conf. on Electromagnetics in Advanced Applicat. (ICEAA)*, Sep. 2013, pp. 1064–1067.

[3] D. Prinsloo, R. Maaskant, M. Ivashina, and P. Meyer, "Mixed-mode sensitivity analysis of a combined differential and common mode active receiving antenna providing near-hemispherical field-of-view coverage," *IEEE Trans. Antennas Propag.*, vol. 62, no. 8, pp. 3951–3961, Aug. 2014.

[4] D. Prinsloo, P. Meyer, R. Maaskant, and M. Ivashina, "Multi-mode composite antenna," South African Provisional patent application 2014/00 363, Jan. 17, 2014.

[5] D. Prinsloo, P. Meyer, M. Ivashina, and R. Maaskant, "A quad-mode antenna for accurate polarimetric measurements over an ultra-wide field-of-view," in *8th European Conf. on Antennas and Propag. (EuCAP)*, April 2014, pp. 3794–3797.

[6] D. Prinsloo, M. Ivashina, R. Maaskant, and P. Meyer, "Beamforming strategies for active multi-mode antennas: Maximum gain, signal-to-noise ratio, and polarization discrimination," in *Int. Conf. on Electromagnetics in Advanced Applicat. (ICEAA)*, Sep. 2014, pp. 507–510.

[7] P. Meyer and D. Prinsloo, "Generalized mixed-mode scattering parameters and antenna far-field conversions," *IEEE Trans. Antennas Propag.*, submitted for publication.

[8] P. Dewdney, P. Hall, R. Schilizzi, and T. Lazio, "The square kilometre array," *Proc. IEEE*, vol. 97, no. 8, pp. 1482–1496, Aug 2009.

[9] P. Dewdney, R. Millenaar, R. McCool, J. Lazio, and T. Cornwell. (2013, March) SKA1 system baseline design. [Online]. Available: www.skatelescope.org

[10] A. van Ardenne *et al.*, "Extending the field of view with phased array techniques: Results of european SKA research," *Proc. IEEE*, vol. 97, no. 8, pp. 1531–1542, Aug 2009.

[11] A. Faulkner *et al.* (2010, Apr.) The aperture array for the SKA: the SKADS white paper. [Online]. Available: http://www.skatelescope.org/publications

[12] C. A. Balanis, *Antenna Theory: Analysis and Design.* John Wiley and Sons, Inc., 2005.

[13] A. Faulkner, "Implementing a high performance AA-mid in SKA2," *Proc. Science*, Apr. 2012.

[14] R. Braun and W. van Cappellen. (2011, Jun.) Aperture arrays for the SKA: Dense or sparse ? SKA Memo 87. [Online]. Available: http://www.skatelescope.org/publications/

[15] S. Wijnholds and W. van Cappellen, "In situ antenna performance evaluation of the LOFAR phased array radio telescope," *IEEE. Trans. Antennas Propag.*, vol. 59, no. 6, pp. 1981 – 1989, Jun. 2011.

[16] M. van Haarlem *et al.*, "LOFAR: The low-frequency array," *Astronomy and Astrophysics*, vol. 556, Aug. 2013.

[17] The LOFAR website. [Online]. Available: http://www.lofar.org/

[18] R. Nijboer, M. Pandey-Pommier, and A. de Bruin. (2009, Jul.) LOFAR imaging capabilities and system sensitivity. 59513_113_Memo_Nijboer.pdf. [Online]. Available: http://www.skatelescope.org/publications/

[19] M. de Vos, A. Gunst, and R. Nijboer, "The LOFAR telescope: System architecture and signal processing," *Proc. IEEE*, vol. 97, no. 8, pp. 1431–1437, Aug 2009.

[20] S. Ellingson *et al.*, "The LWA1 radio telescope," *IEEE Trans. Antennas Propag.*, vol. 61, no. 5, pp. 2540 – 2549, May 2013.

[21] ——, "The long wavelewave array," *Proc. IEEE*, vol. 97, no. 8, pp. 1421 – 1430, Aug. 2009.

[22] B. C. Hicks *et al.*, "A wide-band, active antenna system for long wavelength radio astronomy," *Publications of the Astronomical Society of the Pacific*, vol. 124, no. 920, pp. pp. 1090–1104, 2012. [Online]. Available: http://www.jstor.org/stable/10.1086/668121

[23] S. Tingay *et al.*, "The Murchison widefield array: The square kilometre array precursor at low radio frequencies," *Publications of the Astronomical Society of Australia*, vol. 30, Jan. 2013. [Online]. Available: http://journals.cambridge.org/abstract_S1323358012000070

[24] Murchison Widefield Array. [Online]. Available: http://www.mwatelescope.org/

[25] C. Lonsdale *et al.*, "The murchison widefield array: Design overview," *Proc. IEEE*, vol. 97, no. 8, pp. 1497 –1506, Aug. 2009.

[26] P. Hall *et al.*, "First results from AAVS 0.5: A prototype array for next-generation radio astronomy," in *Int. Conf. on Electromagnetics in Advanced Applicat (ICEAA)*, Sep. 2013, pp. 340 – 343.

[27] A. Faulkner and J. G. Bij de Vaate, "SKA low frequency aperture array design," in *IEEE Int. Symp. on Phased Array Systems & Technology*, Oct. 2013, pp. 768–775.

[28] E. de Lera Acedo, H. Reader, and N. Razavi-Ghods, "Measurements and characterization of differentially-fed antennas for radio astronomy; the case of SKALA," in *Int. Conf. on Electromagnetics in Advanced Applicat. (ICEAA)*, Sept 2013, pp. 968–971.

[29] E. de Lera Acedo, "SKALA: A log-periodic antenna for the SKA," in *Int. Conf. on Electromagnetics in Advanced Applicat. (ICEAA)*, Sep. 2012, pp. 353 – 356.

[30] B. Munk, *Finite Antenna Arrays and FSS*. John Wiley and Sons, Inc., 2003.

[31] G. Kant, P. Patel, S. Wijnholds, M. Ruiter, and E. van der Wal, "EMBRACE: A multi-beam 20,000-element radio astronomical phased array antenna demonstrator," *IEEE Trans. Antennas Propag.*, vol. 59, no. 6, pp. 1990 –2003, Jun. 2011.

[32] P. Benthem and G. Kant, "EMBRACE: Resuls from an aperture array for radio astronomy," in *European Conf. on Antennas and Propag.*, Mar. 2011, pp. 629–633.

[33] M. Arts, R. Maaskant, and G. Kant, "Analysis of the EMBRACE aperture array antenna by the characterisatic basis function method," in *Int. Conf. on Electromagnetics in Advanced Applicat.*, Sept. 2011, pp. 959–962.

[34] M. Arts and B. Fiorelli, "Polarization studies of vivaldi aperture arrays for the square kilometre array," in *Int. Conf. on Electromagnetics in Advanced Applicat. (ICEAA)*, Sep. 2013, pp. 356–359.

[35] B. Fiorelli *et al.*, "Polarization analysis and evaluation for radio astronomy aperture array antennas," in *European Conf. on Antennas and Propag. (EuCAP)*, Apr. 2013, pp. 461–465.

[36] L. Garcia-Munoz *et al.*, "Broadband active differential array for the mid-frequency SKA band," *IEEE. Antennas Propagat. Mag.*, vol. 56, no. 2, pp. 27–38, Apr. 2014.

[37] ——, "Fida3: A novel active array design for the mid-frequency range of the square kilometre array," in *European Conf. on Antennas and Propag. (EuCAP)*, Apr. 2010, pp. 1–4.

[38] Y. Zhang and A. Brown, "Octagband ring antenna for a compact dual-polarized aperture array," *IEEE Trans. Antennas Propag.*, vol. 59, no. 10, pp. 3927–3932, Oct. 2011.

[39] A. Brown and Y. Zhang, "Novel broadband antenna arrays," in *Loughborough Antennas Propag. Conf.*, Nov. 2012.

[40] A. Höök, J. Johansson, and M. Gustafson, "Array antenna with enhanced scanning," U.S. Patent 7,855,690 B2, 2010.

[41] S. Cohn, "Shielded coupled-strip transmission line," *IRE Trans. Microw. Theory Tech.*, vol. 3, no. 5, pp. 29–38, October 1955.

[42] D. Bockelman and W. Eisenstadt, "Combined differential and common-mode scattering parameters: theory and simulation," *IEEE Trans. Microw. Theory Tech.*, vol. 43, no. 7, pp. 1530–1539, Jul 1995.

[43] Y. Zhou and Y. Chen, "Exploration of the properties of the mixed-mode s-parameters," in *Int. Conf. on Microw. and Millimeter Wave Tech. (ICMMT) 2008.*, April 2008, pp. 25–28.

[44] K. Kurokawa, "Power waves and the scattering matrix," *IEEE Trans. Microw. Theory Tech.*, vol. 13, no. 2, pp. 194–202, Mar. 1965.

[45] M. Ivashina, R. Maaskant, and B. Woestenburg, "Equivalent system representation to model the beam sensitivity of receiving antenna arrays," *IEEE Antennas Wireless Propag. Lett.*, vol. 7, pp. 733–737, 2008.

[46] K. F. Warnick, M. V. Ivashina, S. J. Wijnholds, and R. Maaskant, "Polarimetry with phased array antennas: theoretical framework and definitions," *IEEE Trans. Antennas Propag.*, vol. 60, no. 1, pp. 184–196, Jan. 2012.

[47] H. Rothe and W. Dahlke, "Theory of noisy fourpoles," *Proc. IRE*, vol. 44, no. 6, pp. 811–818, June 1956.

[48] H. Haus *et al.*, "Representation of noise in linear twoports," *Proc. IRE*, vol. 48, no. 1, pp. 69–74, Jan 1960.

[49] H. Hillbrand and P. Russer, "An efficient method for computer aided noise analysis of linear amplifier networks," *IEEE Trans. Circuits Syst.*, vol. 23, no. 4, pp. 235–238, Apr 1976.

[50] D. M. Pozar, *Microwave Engineering*, 3rd ed. John Wiley and Sons, Inc., 2005.

[51] K. F. Warnick and M. A. Jensen, "Effects of mutual coupling on interference mitigation with a focal plane array," *IEEE Trans. Antennas Propag.*, vol. 53, no. 8, pp. 2490–2498, Aug. 2005.

[52] R. Maaskant and E. E. M. Woestenburg, "Applying the active antenna impedance to achieve noise match in receiving array antennas," in *Proc. IEEE Int. Antennas Propag. Symp.*, Honolulu, Hawaii, Apr. 2007, pp. 5889–5892.

[53] K. F. Warnick and M. Jensen, "Optimal noise matching condition for mutually-coupled antenna arrays," in *IEEE Antennas Propag. Soc. Int. Symp.*, June 2007, pp. 2953–2956.

[54] K. F. Warnick *et al.*, "Unified definitions of efficiencies and system noise temperature for receiving antenna arrays," *IEEE Trans. Antennas Propag.*, vol. 58, no. 6, pp. 2121–2125, June 2010.

[55] J. Engberg and T. Larsen, *Noise Theory of Linear and Nonlinear Circuits*. New York: Wiley, 1995.

[56] B. D. Jeffs *et al.*, "Signal processing for phased array feeds in radio astronomical telescopes," *IEEE J. Sel. Topics Signal Process.*, vol. 2, no. 5, pp. 635–646, Oct. 2008.

[57] K. F. Warnick and B. D. Jeffs, "Efficiencies and system temperature for a beamforming array," *IEEE Antennas and Wireless Propag. Lett.*, vol. 7, no. 1, pp. 565–568, 2008.

[58] S. Wijnholds, M. Ivashina, R. Maaskant, and K. F. Warnick, "Polarimetry with phased array antennas: Sensitivity and polarimetric performance using unpolarized sources for calibration," *IEEE Trans. Antennas Propag.*, vol. 60, no. 10, pp. 4688–4698, Oct 2012.

[59] J. P. Hamaker, J. D. Bregman, and R. J. Sault, "Understanding radio polarimetry – I. mathematical foundations," *Astron. Astrophys. Suppl. Ser.*, vol. 117, pp. 137–147, May 1996.

[60] *IEEE Standard Definitions of Terms for Radio Wave Propagation*, IEEE Std. 211-1997, Rev. May 1998.

[61] T. Carozzi and G. Woan, "A fundamental figure of merit for radio polarimeters," *IEEE Trans. Antennas Propag.*, vol. 59, no. 6, pp. 2058–2065, June 2011.

[62] M. Ivashina *et al.*, "An optimal beamforming strategy for wide-field surveys with phased-array-fed reflector antennas," *IEEE Trans. Antennas Propag.*, vol. 59, no. 6, pp. 1864–1875, June 2011.

[63] K. D. Cheng and F. I. Tseng, "Maximisation of directive gain for circular and elliptical arrays," *Proc. IEE*, vol. 114, no. 5, pp. 589–594, May 1967.